MODELING OF THERMODYNAMIC PROPERTIES AND PHASE EQUILIBRIA OF MULTICOMPONENT SYSTEMS RELATED TO THE OIL AND GAS INDUSTRY USING THE PC-SAFT EQUATION OF STATE

A Thesis

by

SALLY HISHAM MOHAMED EL MERAGAWI

Submitted to the Office of Graduate and Professional Studies of
Texas A&M University
in partial fulfillment of the requirements of the degree of

MASTER OF SCIENCE

Chair of Committee,	Ioannis G. Economou
Committee Members,	Kenneth Hall
	Vassilios Kelessidis
Head of Department,	M. Nazmul Karim

August 2015

Major Subject: Chemical Engineering

ABSTRACT

Equations of state (EoS) have proved to be a reliable tool in chemical engineering thermodynamics for modeling the physical properties of complex systems. Various types of EoS have been developed based on different theories. For various reasons, some have become more popular for use in industry and academia. Of the popular EoS, two were chosen for investigation in this thesis. The first one was the Perturbed Chain- Statistical Associating Fluid Theory (PC-SAFT), an equation derived based on statistical mechanics and the second was the Peng-Robinson (PR) EoS, a cubic EoS commonly used in industry.

In this work, the prediction capabilities of these two EoS were compared for several properties. The analysis began with an evaluation of their use in the prediction of the saturation properties of pure components and derivative properties from ambient conditions to the supercritical range. The particular derivative properties studied include the isochoric and isobaric heat capacities, the speed of sound, and the isothermal compressibility. In general, it was concluded that PC-SAFT outperforms PR in all cases. Next, the same primary and derivative properties of several binary and a select ternary mixture were studied. To improve agreement with experimental data, a binary interaction parameter was introduced and fitted to binary mixture vapor – liquid equilibria (VLE) data. This procedure drastically improved the accuracy of the models compared to the case where no binary interaction parameter used for the case of VLE predictions. However, for the case of the derivative properties, the use of the binary interaction parameter to ensure a more accurate representation of the interactions between molecules had only a marginal effect on the prediction of these properties.

Finally, phase equilibria of hydrates were studied. As EoS for fluids are not designed to predict the properties of solid phases, the van der Waals-Platteeuw model was incorporated to allow for the prediction of three-phase equilibrium conditions of various hydrate formers. Specifically, this work focused on the equilibrium of a water-rich liquid phase, a hydrate phase and a vapor phase rich in a hydrate former. In all cases, calculations of the solid hydrate phase properties are based on the Kihara potential. This potential requires three parameters to be defined; initial values for which were found through a review of the literature. The accuracy of the predictions of the three-phase equilibrium is highly dependent on the reliability of these parameters. Thus, one of the parameters, the so-called ε parameter, was fitted to hydrate equilibrium data and resulted in a significant improvement in the accuracy of predictions of both PC-SAFT and PR EoS. The new set of parameters was then used to predict the three-phase equilibrium of several binary, ternary and quaternary mixtures of hydrate forming agents. Several conclusions are drawn from this work, including the observation that the accuracy of the models is reduced when the number of components increases.

ACKNOWLEDGEMENTS

I would like to express my gratitude and thanks to my advisor Professor Ioannis Economou. I would like to thank you for your advice and encouragement in my research which has allowed me to learn much in the field of the thermodynamics. I greatly appreciate your mentoring and advice in both my research and for my future career. I would also like to thank Professor Kenneth Hall and Professor Vassilios Kelessidis for serving in my committee. I am also grateful to the members of my research team for teaching me and helping me through the various obstacles that I have faced during my work on this thesis. I would like to thank Nikolaos Diamantonis for his work on the FORTRAN codes and algorithms used in this work. In addition, I would like to express my gratitude to the chemical engineering faculty and staff at Texas A&M University at Qatar for all the guidance that they have provided me with over the years.

NOMENCLATURE

Latin Letters

a	Kihara potential hard core radius [Å]
a	Helmholtz free energy
C_p	Isobaric Heat Capacity [J/mol.K]
C_v	Isochoric Heat Capacity [J/mol.K]
f_i^n	Fugacity of component i in phase n
k	Boltzmann constant
K	K-factor
k_{ij}	Binary interaction parameter
m	Number of segments in a molecule
MM	Molar Mass [g/mol]
P	Pressure [MPa]
P_c	Critical Pressure [MPa]
R	Universal Gas Constant [J/mol.K]
T	Temperature [K]
T_c	Critical temperature [K]
v	Molar volume [cm^3/mol]
x	Liquid mole fraction
X	Arbitrary property designation
y	Vapor mole fraction
z	Inlet mole fraction

Greek Letters

β	Empty hydrate lattice
ε	Potential well depth
φ	Fugacity coefficient
σ	Potential collision diameter
ω	Acentric factor
μ	Chemical potential

Subscripts

w	Water
i, j	Component identifications
g	Hydrate guest

Superscripts

assoc	Association
disp	Dispersion
hc	Hard core
hs	Hard sphere
ideal	Ideal
res	Residual
sat	Saturation

List of Abbreviations

#DP	Number of data points
AAD	Average absolute deviation
CCS	Carbon Capture and Sequestration
D	Diverges
EoS	Equation of State
HVL	Hydrate vapor liquid equilibrium
N/A	Not available
P&P	Parrish and Prausnitz Kihara Parameters
PC-SAFT	Perturbed Chain- Statistical Associating Fluid Theory
PR	Peng- Robinson
Q1	Liquid water, hydrate, vapor, ice equilibrium point
Q2	Liquid water, hydrate, vapor, liquid guest equilibrium point
r. P&P	Regressed Parrish and Prausnitz Kihara Parameters
r. S&K	Regressed Sloan and Koh Kihara Parameters
S&K	Sloan and Koh Kihara Parameters
VLE	Vapor liquid equilibrium

TABLE OF CONTENTS

Page

LIST OF FIGURES

Page

LIST OF TABLES

Page

1. INTRODUCTION

The change of Earth's climate has been a global concern since the 1950s. In the years since then, evidence of global warming such as changes in the surface temperature, sea level, and glacier volume have been attributed to the release of greenhouse gases (GHGs).[1] The GHGs trap infrared radiation in the atmosphere leading to increasing levels of thermal energy that have unfavorable side effects on the climate. The GHGs in the atmosphere responsible for climate change are carbon dioxide (CO_2), methane (CH_4), nitrous oxide (N_2O), ozone (O_3), water (H_2O) and chlorofluorocarbons (CFCs). Of these the most abundent and harmful are CO_2 and CH_4. Fluctuations in the global concentrations of these gases are the results of both anthropogenic and natural processes.[2]

The Intergovernmental Panel on Climate Change (IPCC) has shown that industry is responsible for 60% of global CO_2 emissions and 75% of anthropogenic CO_2 emissions, a large portion of which is the result of the burning of fossil fuels. The IPCC has estimated that approximately 24,000 metric tons of CO_2 is released into the atmosphere as a result of fossil fuel combustion per annum.[3] Reducing the concentration of CO_2 in the atmosphere is of vital interest to various factions including policy makers, industry, research groups, societies and individuals. In order to achieve this aim, different mitigation methods have been suggested that include improving the efficiency of converting fossil fuels to energy and switching to renewable energy, nuclear power or low carbon fuels such as natural gas instead of coal or oil to control CO_2 levels in the atmosphere.[3] Of those commercially available, the most favored method is the storage of the excess CO_2 in geological reservoirs. Carbon Capture and Storage (CCS) is the most popular large-scale process for mitigating concentrations of CO_2 used in

industry.[2] CCS is a process that is carried out in three disparate stages: capture, transportation and sequestration. Currently, the cost of implementation of CCS technology in a natural gas production plant is 38-91 US$ per ton of CO_2 sequestered which increases the cost of electricity by up to 85%.[3] In order to optimize this process and reduce cost, the ability to accurately know the thermodynamic properties of these systems over large ranges of conditions is essential.

On the other hand, while CO_2 is the most abundant GHG, CH_4 is more harmful on a per mass basis. The Global Warming Potential (GWP) is a measure of the ability of a GHG to trap thermal radiation in the atmosphere relative to CO_2. CH_4 has a GWP of 21. CH_4 can be found in large quantities in natural reserves of hydrates in the arctic permafrost and on the oceanic seabed.[4] Slight changes in the conditions of these hydrates might cause them to dissociate, releasing the stored CH_4 into the atmosphere. These releases can sustain arctic warming causing further melting of the hydrate phase. The overall result is an exacerbated effect on climate change. In addition, gas hydrates are also an area of concern within the oil and gas industry where natural gas mixtures are piped from offshore at conditions that are ideal for hydrate formation. The obstruction of the pipelines costs companies millions of dollars in production loss and equipment damages. In order to avoid hydrate phase melting in the arctic permafrost and hydrate phase formation in natural gas production pipelines, the ability to accurately know the thermodynamic equilibrium of these systems over large ranges of conditions is necessary.

CO_2 and CH_4 do not typically exist as pure fluids and so it is important to study them in mixtures with various other components. The composition of the mixtures depends on the source of the natural gas and the technology used to extract and treat it. In turn, the composition of the mixtures affects the phase equilibria. Thus, a full understanding of these concepts and

the optimization of each process relies on the ability to accurately model systems containing these species alone, in multicomponent mixtures and in different phases over a range of temperatures, pressures and compositions. In this project, two thermodynamic equations of state (EoS), one cubic and the other a higher order equation rooted in statistical mechanics, are used to model equilibrium and thermodynamic properties. This work will include an assessment of the accuracy of these models and evaluate methods to improve the performance of these models across a wide range of conditions. A more comprehensive list of objectives is available in Section 0.

This thesis is divided into three main sections: literature review, methodology, and results and discussion. The Literature Review (Section 2) section covers an analysis of previous work done in the field in two parts: Section 2.1 is based on the CCS and Section 2.2 is based on hydrate phase equilibrium. The Models and Computational Methodology (Section 3) introduces the procedures used to calculate the different properties of interest. The Results and Discussion (Section 4) is split into three different sections. Section 4.1 shows the accuracy of the EoS for the prediction of phase equilibria and derivative properties of pure components. Section 4.2 studies the complexities that arise when more components are added to the mixture. Finally, Section 0 explores the effect of the formation of a hydrate phase on the prediction of the three-phase equilibrium of the hydrate, liquid and vapor phases.

1.1 Objectives of Study

The purpose of this thesis is to study:

1. The accuracy of thermodynamic EoS to predict the phase equilibria and derivative thermodynamic properties, including speed of sound, isothermal compressibility and isochoric and isobaric heat capacities, of pure components. The focus lies on the components usually found in CCS processes which in addition to CO_2 also includes CH_4, CO, Ar, N_2, and O_2.
2. The use of thermodynamic EoS to predict the vapor-liquid phase equilibria and derivative properties of multicomponent mixtures containing CO_2.
3. The ability of a thermodynamic EoS in conjunction with the van der Waals-Platteeuw to model the equilibrium pressure of hydrates systems for a wide range of components and conditions. The focus of these calculations lies in the prediction of liquid-vapor-hydrate equilibrium for the components mentioned previously and also for ethane (C_2H_6), propane (C_3H_8), isobutane (iC_4H_{10}) and hydrogen sulfide (H_2S).
4. The effect of using the statistical mechanics-based EoS, Perturbed Chain-Statistical Associating Fluid Theory (PC-SAFT), compared to a simple cubic EoS, Peng-Robinson (PR) in modeling the complex systems described above.
5. The effect of varying different parameters, including the binary interaction parameter and interaction potential parameters, for the systems under consideration for the studied range of conditions and optimizing the parameters to improve predictions.

2. LITERATURE REVIEW

2.1 Carbon Capture and Sequestration

The renewed interest in carbon capture technologies is primarily a result of global regulations, such as the Clean Development Mechanism of the Kyoto Protocol, which committed to reduce concentrations of greenhouse gases, chiefly CO_2, released to the atmosphere in the period of 2008-2012. The energy sector has recognized that the most favorable strategy for reduction of GHG concentrations is the recovery of CO_2 at the source of emission. To achieve this, various separation technologies are being developed and optimized, as discussed by Mondal et al.[5] After capture, the concentrated CO_2 stream is either transported to storage sites, deep in the seabed or in depleted oil reservoirs, or alternatively repurposed and utilized.[6] Optimization of these processes requires accurate understanding of the properties of the components commonly found in these systems and models that can accurately reproduce their behaviors under various conditions.

All three stages of the CCS process (capture, transportation and storage) are rich in CO_2 and contain impurities like argon (Ar), nitrogen (N_2), methane (CH_4), water (H_2O), oxygen (O_2), sulfur dioxide (SO_2), hydrogen sulfide (H_2S) and many others. The presence and concentration of the contaminants depend on the source and method used to capture CO_2.[7] There are three common industrial processes used to capture CO_2 from processes streams: pre-combustion, post-combustion, and oxyfuel combustion.

In a post-combustion process, CO_2 is separated at a stage after the fossil fuel is used to produce energy and results in streams containing N_2, O_2, CO, SO_2 and H_2O. In a pre-combustion process, the fuel is purified of CO_2 prior to combustion stage resulting in streams

free of O_2 and SO_2 but containing Ar, CH_4, H_2 and H_2S. Finally, oxy-fuel combustions result in concentrated CO_2 streams similar to that of pre-combustion with the addition of Ar. The concentration of these impurities ranges from the order of 10 ppm up to 10 to 15% by mole of the composition of the stream.[8,9]

The three stages of CCS have varied operating conditions typically ranging from 0 to 50 MPa in pressure and temperatures above 218.15 K.[10] Capture of CO_2 via one of the previously discussed technologies occurs at pressures less than 10 MPa. Transportation of CO_2 streams in the liquid or dense fluid phase, at pressures above 9.6 MPa, is favored as it reduces the cost by avoiding two-phase fluid flow and lessens the burden of further compression for storage. After transportation, CO_2 is stored at pressures up to 50 MPa.[3] Due to the large range of operating conditions for these processes and the different phases that occur the use of thermodynamic models for precise property evaluation becomes crucial.

The concentration of impurities significantly impacts the conditions at which the process operates, the pipeline integrity and flow assurance.[11] The operating conditions are influenced by the density and the phase of the stream, making the accurate prediction of these properties important for the design of pipelines. Furthermore, the integrity of pipelines may be affected by impurities with corrosive properties, as is the case with H_2O and CO_2, making selection of the material a critical factor in the design stage.[3] If the concentration of water vapor in the process stream is high enough, the flow of the process stream may be interrupted by the formation of carbon dioxide hydrates.[12]

Properties of the pure gas species related to CCS have been studied extensively in the literature. The NIST database[13] has archived large quantities of experimental data on pure component vapor pressures, saturation densities, and primary and derivative properties on a

variety of components including those relevant to the CCS process. Others have also studied the density, speed of sound and isothermal compressibility of pure CO_2. A review of the literature has shown vast interest in the effect of impurities on these properties, and various authors have performed experiments to determine the effect of concentration of the impurity over different conditions.

Experimental vapor-liquid equilibrium (VLE) and density data on binary mixtures of CO_2 with impurities such as Ar[14,15], SO_2[16,17], CH_4[18–22], N_2[18,23–25], CO[26,27] and O_2[28,29] are widely available in the literature.[30] However, multicomponent CO_2 mixtures with more components are less common. Experimental data on multicomponent mixtures is useful for the validation of models fitted to pure component properties.

Li et al.[10,11] comprehensively reviewed available binary and ternary vapor-liquid equilibrium (VLE) data containing CO_2 for mixtures relevant to CCS. They noted a scarcity of experimental data in the ranges of conditions under which these mixtures have been studied and inconsistencies in the available data, especially close to the critical point of the binary mixtures.

Muirbrook et al.[31] and Zenner and Dana[32] studied the mixture of CO_2 with N_2 and O_2 over temperatures ranging from 218.15 to 273.15 K and 1.3 to 15 MPa. Experimental VLE of CO_2 with N_2 and CH_4 has been studied at temperatures ranging from 220-273 K.[33,34] Later, Seitz et al.[35] experimentally studied the volumetric properties of the same mixture. Creton et al.[30] measured the densities of several binary mixtures and two CO_2 rich quaternary mixtures CO_2-N_2-Ar-O_2 and CO_2-N_2-Ar-O_2-SO_2 at ranges from low to high density.

The availability of experimental data is essential for model validation. There are various types of EoS used to predict thermodynamic properties, the most commonly studied are cubic EoS such as Peng-Robinson, those EoS based on statistical mechanics such as the Statistical Associating Fluid Theory (SAFT) family of EoS and non-analytical, multi-parameter approaches such as the GERG (European Gas Research Group) model.

Much work has been done on the prediction of VLE for pure CO_2 and binary mixtures containing impurities using cubic EoS such as Peng Robinson[36] (PR) and Soave-Redlich-Kwong[37] (SRK). Li and Yan[38] fitted different binary interaction parameters to each of the liquid and vapor phases. They also noted the inaccuracy in the ability of PR to properly predict volumetric properties of the different phases.

Al-Sahhaf[34] compared the ability of PR and Patel-Teja EoS in predicting the VLE of the ternary system N_2-CO_2-CH_4 at 230 K and 250 K and found them to be comparable. Thiery et al.[39] studied the same ternary mixture with the Soave-Redlich-Kwong (SRK) EoS. Vrabec et al.[40] reviewed the use of several EoS for the prediction of N_2-O_2-CO_2 at low temperatures. Of the cubic EoS, PR was found to perform best across a range of conditions.

Xu et al.[41] used the modified PR EoS[42] to predict VLE of CO_2 with N_2 and CH_4 at high pressure and concluded that improved bubble point pressure and compositions predictions are based on the use of temperature independent binary interaction coefficients. Many more studies have been conducted using cubic and virial EoS.[12,43,44]

Recently, more studies have been conducted on the use of statistical mechanics based EoS, such as SAFT and Perturbed Chain-SAFT (PC-SAFT) for these applications. Belkadi et al.[45] predicted the VLE curves of CO_2 with nitrogen dioxide (NO_2) and dinitrogen tetraoxide

(N_2O_4) using soft-SAFT. Sanchez et al.[46] studied the performance of PC-SAFT in the prediction of vapor-liquid equilibrium of binary mixtures of N_2 and various hydrocarbons including, CH_4, C_2H_6, C_3H_8 and i-C_4H_{10}. The predictions were in good agreement with experimental data, with errors in the order of 1-10% in the equilibrium pressure for binary mixtures containing shorter hydrocarbons. For the binary mixtures containing longer hydrocarbons, it was seen that the error increased. More importantly, they studied a ternary system containing CO_2 in a mixture with CH_4 and N_2. Through fitted binary interaction parameters, they were able to predict the VLE boundaries accurately at 230 K and 8.62 MPa.

Second order derivative properties such as isochoric and isobaric heat capacities, isothermal compressibility, and Joule-Thompson coefficients are important in the design of industrial processes. For example, speed of sound is a useful property for the detection of leaks in pipelines and for flow assurance.[47] Isothermal compressibility factors are used in the design of high-pressure equipment.[48]

Al-Siyabi[8] measured experimental data for the speed of sound and isothermal compressibility of several binary mixtures containing CO_2 and N_2, CH_4, H_2, O_2, Ar, CO. In addition, he reported the derivative properties of the ternary mixture CO_2-Ar-CO and the quaternary mixture CO_2-N_2-CH_4-H_2. Kachanov et al.[49] measured speed of sound for the binary CO_2-N_2 mixture in the high-pressure region ranging from 50 to 400 MPa. There are still only a limited number of available experimental data for derivative properties in the relevant ranges of conditions.[50] Diamantonis et al.[51] suggested that for CO_2 rich multicomponent mixtures representative of the compositions and conditions of actual pipeline systems, derivative properties such as speed of sound, Joule-Thomson coefficients, isothermal compressibility and heat capacities should be measured.

Diamantonis et al.[52] reported on the efficiency of the PC-SAFT EoS for the prediction of the isothermal compressibility for the same quaternary system. Liang et al.[53] conducted an in-depth study on the prediction of the speed of sound of pure alkanes using various EoS including soft-PC-SAFT, Cubic Plus Association (CPA) and others. They determined that PC-SAFT could most accurately predicted the speed of sound over pressure ranges up to 50 MPa most accurately. Lafitte et al.[54] used SAFT to predict second-order derivative properties and suggested that the fitting of SAFT pure component parameters to both vapor pressure and speed of sound would improve accuracy. However, Llovell et al.[55] argue that this detracts from the predictive power of the EoS.

2.2 Gas Hydrates

One important class of solid structures that are known to occur in a number of industrial applications including CCS processes and the oil and gas industry are gas hydrates. Gas hydrates have become important in flow assurance in pipelines where even low-level water content can cause hydrate formation in pipelines used to transport CO_2 or CH_4 rich streams. Recently, gas hydrates have been considered as an alternative storage method for CO_2 due to their potential to store large volumes of gases in relatively small volumes.[56] Hydrates are also a promising technology for the capture of CO_2 in CCS processes.[57] Naturally occurring methane hydrates are plentiful in the arctic permafrost and have been considered an alternative energy source to natural gas reservoirs.[58]

Gas hydrates occur when water forms 3-dimensional networks through hydrogen bonding and arranges in crystalline structures with cavities. As empty cages, these hydrate cavities are unstable and require the presence of guest molecules to stabilize them. However, hydrates are nonstoichiometric and do not require full occupancy for stabilization of the

structure. Many gases in a range of sizes from Ar to cyclo-octane have been documented to form hydrates under conditions of low temperatures and moderate to high pressures.[58,59] The intermolecular interactions between the guest molecules and the water molecules influence the size and shape of the structure.

Hydrates are known to form in many structures though the most common formations occur in either cubic structure I (sI), cubic structure II (sII) or hexagonal structure (sH) depending on the size of the guest. sI structures are typically formed by small molecules diameters less than 5Å, sII accommodates slightly larger atoms with molecular diameters between 5 and 7 Å and sH is formed by even larger molecules with smaller molecules stabilizing the smaller cages in the lattice. An exception occurs when the structure formed by the guest molecules is dependent on the pressure conditions of the system. For example, at pressures below 280 MPa argon forms an sII structure and as the pressure rises above this limit the structure reforms to an sI type. Under even higher pressure, the hydrate will restructure into sH.[59] For the pressure ranges seen in gas production and processing units, the structures of hydrates for the gas hydrate formers studied in this work are presented in Table 1.

Table 1. Hydrate forming structures for common gas hydrates[60]

Guest Molecule	Hydrate Structure
Methane	sI
Ethane	sI
Propane	sII
Iso-butane	sII
Carbon Dioxide	sI
Nitrogen	sI
Hydrogen Sulfide	sI
Argon	sII/sI/sH
Oxygen	sI

The difference in the geometry of each structure effects the thermodynamic properties of the hydrate phase. A single sI structure cell consists of two pentagonal dodecahedrons, a 12 sided cage of pentagons (5^{12}), and six tetrakaidecahedron, a 14 sided cavity of 12 pentagonal and 2 hexagonal sides ($5^{12}6^2$). Similarly, a sII unit cell consists of sixteen pentagonal dodecahedrons and eight hexakaidecahedron, a 16 sided cavity of 12 pentagonal and 4 hexagonal sides ($5^{12}6^4$). Finally, an sH hydrate configuration consists of three differently sized cages: three pentagonal dodecahedrons, two irregular dodecahedron, a 12 sided cavity with 3 square, 6 pentagonal and 3 hexagonal sides, and a single icosahedron, a 20 sided cavity consisting of 12 pentagonal and 8 hexagonal sides. A visualization of all three hydrate structures are presented in Figure 1. It should be noted that the structures presented in the figure below are partial representations of each cell unit.

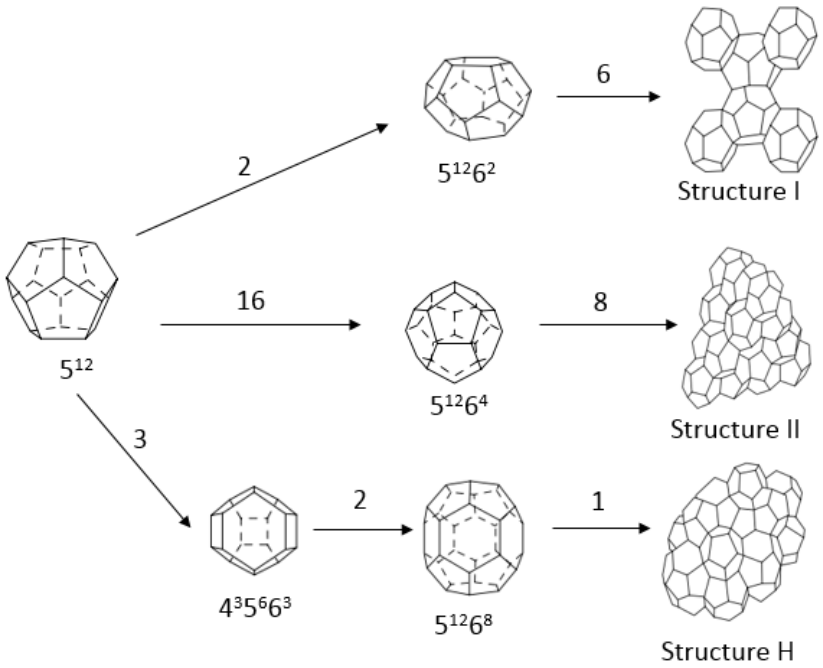

Figure 1. Geometry of cavities and unit cells in each of the sI, sII and sH hydrate structures.[58]

Other properties of the structure, summarized in Table 2, include the number of water molecules that each unit cell is composed of, the average cavity radius and the coordination number of the encaged guest molecule in each cavity space.

Table 2. Hydrate lattice structure properties [58,59,61]

Hydrate Structure	sI		sII		sH		
Cavity	Small	Large	Small	Large	Small	Medium	Large
Description	5^{12}	$5^{12}6^2$	5^{12}	$5^{12}6^4$	5^{12}	$4^3 5^6 6^3$	$5^{12}6^8$
Number of Cavities per unit cell	2	6	16	8	3	2	1
Average Cavity Radius (Å)	3.975	4.30	3.91	4.73	3.94	4.04	5.79
Coordination Number	20	24	20	28	20	20	36
Number of water molecules per unit cell	46		136		34		

Experimental studies of gas hydrates with both pure guest and guest mixtures are common in literature and have been reviewed in detail by Sloan and Koh[59] and archived by NIST[62]. Holder et al.[60] have empirical correlations that describe available experimental data for several pure guest hydrate systems at temperatures below 300 K.

Fluid-hydrate phase equilibrium has been studied theoretically, on both macroscopic and microscopic scales. At the macroscopic scale, the development of a theoretical EoS is needed for accurate prediction of properties and phase equilibria calculations.[59,63,64] At the molecular level, Molecular Dynamics (MD) and Metropolis Monte Carlo (MC) simulations[65,66] are used for the elucidation of microscopic structures[67–69] and the prediction of the equilibrium conditions[70–74]. However, due to the time-consuming nature of these simulations, developing an EoS can provide a simple tool for the prediction of hydrate properties.

EoS for fluids, such as PC-SAFT and PR, do not have the intrinsic ability to describe the thermodynamic properties of the hydrate phase. As such, in order to model fluid-hydrate

equilibrium, EoS are used in conjunction with models able to describe hydrate phase properties. The van der Waals-Platteeuw (vdW-P) model is one such model that is widely used to generate predictions of the chemical potential of the hydrate phase at specified conditions. In this way, calculation of the chemical potential of water in the different phases can be made to predict the fluid-hydrate equilibrium conditions.

Van der Waals and Platteeuw[75] derived an expression to model the hydrate phase relative to a theoretical metastable empty hydrate lattice. This model assumes that the hydrates form spherical cavities that contain a single guest and that the guests in different cages do not interact. It also makes the assumption that the guest molecules do not cause distortion in the lattice structure. This assumption allows for the contributions to the Helmholtz free energy to be simplified to the sum of the energy of the guest molecule and that of the empty lattice.[76] In addition, a secondary result of this assumption is that the reference chemical potential of the empty hydrate lattice is the same for different guest molecules.[77] Finally, it assumes that Boltzmann statistics is applicable which allows for the canonical partition function to be simplified to a one-dimensional integral Lennard-Jones Devonshire approximation of a smooth cell potential function.[66]

Chen and Guo[78,79] noted that the vdW-P theory neglects a full physical description of the hydrate phase as it does not account for the local stability of the hydrate and the kinetic mechanism. They define the local hydrate stability based on the local occupancy of the hydrate cages. Karakatsani and Kontogeorgis[63] have shown that neglecting cage distortion may not be valid for larger hydrocarbon gases such as propane. On average, the radius of the hydrate cage is dependent on temperature, pressure and the composition of the guest molecules.[59]

An alternative method to the vdW-P model was developed by Klauda and Sandler[77] and is based on adjusting the reference chemical potential and enthalpy to depend on the guest molecule introduced into the system. This dependency was accomplished through fitting the vapor pressure, $P_w^{sat,\beta}(T)$, of the empty lattice in Equation [1] to experimental hydrate equilibrium data to allow for the subsequent calculation of the fugacity, $f_w^{\beta}(T)$. This approach showed promising results and was later extended to mixtures of guest molecules.[80]

$$f_w^{\beta}(\mathrm{T},\mathrm{P}) = \mathrm{P}_w^{sat,\beta}(T)\phi_w^{sat,\beta}\exp\left(\frac{V_w^{\beta}(T,P)\left(P - P_w^{sat,\beta}(T)\right)}{RT}\right) \qquad [1]$$

where $\varphi_w^{sat,\beta}$ is the fugacity coefficient of water phase at saturation conditions, $V_w^{\beta}(T,P)$ is the molar volume of water at the temperature, T, and pressure, P, of the system and R is the gas constant.

Various studies have investigated the EoS used to model the fluid phase. Sun and Chen[81] studied pure CO_2 and H_2S by adjusting the Patel-Teja cubic EoS to account for electrostatic contributions. The addition of this term accounts for the solubility and dissolution of CO_2 and H_2S in water and resulted in significant improvements when compared to the predictions generated by the Chen-Guo model. Delavar and Haghtalab[82] studied pure and binary gas systems using Soave-Redlich-Kwong (SRK) EoS for the fluid phase in combination with the UNIQUAC model to account for the activity coefficient of water in the liquid phase. They recorded an improvement in results when compared to results generated with the typical assumption of the activity coefficient being unity. Li et al.[83] used SAFT with vdW-P to model binary combinations of CO_2, H_2, H_2S, N_2 and hydrocarbon from CH_4 to C_4H_{10} with good

accuracy. However, they evaluate hydrates at relatively low pressures where good accuracy can be expected from SAFT-type EoS.

3. MODELS AND COMPUTATIONAL METHODOLOGY

3.1 Cubic Equations of State

In this work, the Peng-Robinson[36] (PR) cubic EoS was used. It is a model that is commonly used both in industry and research as it is relatively accurate for the prediction of vapor pressure and density of non-polar and slightly polar fluids; however, it is not as precise for predicting properties of associating compounds such as water. The equation is a pressure explicit expression formulated as follows:

$$P = \frac{RT}{v-b} - \frac{a(T)}{v(v+b)+b(v-b)} \qquad [2]$$

where T is the temperature of the system, R is the gas constant, v is the molar volume, and a and b are constants specific to each component. For a fluid, b is proportional to the size of the molecule or the molecular volume and is calculated based only on the critical temperature, T_c, and the critical pressure, P_c, in accordance with Equation [3].

$$b = 0.07780\frac{RT_c}{P_c} \qquad [3]$$

The term $a(T)$ is an expression that characterizes the intermolecular attractive interactions as a product of a temperature dependent term, $\alpha(T)$, and a constant, $a(T_c)$ as indicated by Equation [4]. A dimensional analysis of the units of this terms shows that $a(T)$ is proportional to the product of the molar energy and the molar volume.

$$a(T) = a(T_c)\alpha(T,\omega) \qquad [4]$$

where each of these terms are expressed by Equations [5] to [7] and depend on an additional parameter, ω, the acentric factor which represents the deviations of the intermolecular potential from that of a perfectly spherical molecule.[84]

$$a\left(T_c\right) = 0.45724\frac{\left(RT_c\right)^2}{P_c} \quad [5]$$

$$\alpha\left(T\right) = \left[1+\beta\left(1-\sqrt{\frac{T}{T_c}}\right)\right]^2 \quad [6]$$

$$\beta = 0.37464 + 1.54226\omega - 0.26992\omega^2 \quad [7]$$

From this formulation, in order for a system to be fully defined the critical temperature, critical pressure, and the acentric factor for each component are required. In Table 3 these properties are given for the various components examined here.

Table 3. Molar mass, critical properties and acentric factor of pure component species[84]

Chemical Species	MM [g/mol]	T_c [K]	P_c [MPa]	ω
O_2	32.00	154.6	5.04	0.025
Ar	39.95	150.8	4.87	0.001
N_2	28.00	126.2	3.39	0.039
CO	28.01	132.9	3.50	0.066
CO_2	44.01	304.1	7.38	0.239
CH_4	16.04	190.4	4.60	0.011
C_2H_6	30.07	305.3	4.87	0.099
C_3H_8	44.1	369.8	4.25	0.153
i-C_4H_{10}	58.12	408.2	3.65	0.183
H_2O	18.01	647.3	22.12	0.344
H_2S	34.08	373.2	8.94	0.081

The PR EoS is extended to mixtures using appropriate mixing rules. The most common mixing rules are the one-fluid van der Waals mixing rules:

$$a = \sum_i \sum_j x_i x_j a_{ij} \quad [8]$$

where a_{ij} is the cross interaction parameter and is mathematically defined using Equation [9].

$$a_{ij} = \sqrt{a_i a_j}\left(1 - k_{ij}\right) \quad [9]$$

$$b = \sum_i x_i b_i \quad [10]$$

In Equation [9], k_{ij} is the temperature independent binary interaction parameter, an adjustable parameter that is fitted to binary vapor-liquid equilibrium experimental data; typically, through the minimization of the objective function. This function is defined as the absolute average deviation (AAD) between the EoS's prediction of the bubble pressure and its experimental value.

$$O.F. = \frac{|P^{\text{sat,prediction}} - P^{\text{sat,experimental}}|}{P^{\text{sat,experimental}}} \quad [11]$$

In this thesis, when calculations assume a value of 0 for the binary interaction parameter, the calculations are referred to as predictions. On the other hand, when calculations include a non-zero k_{ij} value, they are referred to as correlations.

3.2 Perturbed Chain- Statistical Associating Fluid Theory

Unlike cubic EoS, which are based on the van der Waals EoS, the SAFT family of EoS are based on statistical mechanics principles. The development of these molecular-based theories has become popular in the recent years due to their improved accuracy compared to more classical methods. Chapman developed the original SAFT[85,86] EoS based on Wertheim's first order thermodynamic perturbation theory that defined a relationship between the Helmholtz energy and the association interactions of a molecule.[87–90] In particular, this theory models the behavior of real fluids by describing different interactions as a series of perturbations to a reference fluid. SAFT is based on a reference fluid composed of hard spheres where the attractive and repulsive interaction are based on the modified square well potential model suggested by Chen and Kreglewski[91].

After the development of the original SAFT, many other versions of the EoS were derived and vary from the original in the type of reference fluid or potential model used. SAFT-VR[92,93] implemented the use of a variable range square well intermolecular potential; however, soft-SAFT[94,95] used a Lennard-Jones reference fluid while PC-SAFT is based on a hard-chain reference fluid. There are many other variations of the SAFT EoS, and several comprehensive reviews[96,97] have covered their differences in detail.

The formulation of the PC-SAFT EoS is based on the calculation of the residual Helmholtz energy, a^{res}, in terms of the summation the Helmholtz contributions of different intermolecular interactions, according to the expression:

$$\frac{a^{res}}{RT} = \frac{a}{RT} - \frac{a^{ideal}}{RT} = \frac{a^{hc}}{RT} + \frac{a^{disp}}{RT} + \frac{a^{assoc}}{RT} \qquad [12]$$

The reference fluid is composed of a hard-chain fluid, where its segments are freely jointed and defined exclusively by their hard-core repulsive interactions. The Helmholtz energy contribution of the reference fluid, a^{hc}, is a mathematical combination of the Helmholtz free energy of a hard sphere reference fluid used in the SAFT EoS (the Carnahan-Starling expression[98]) and the energy of chain formation. The explicit description of this term is provided in the Appendix (Section 7.1.1)

The addition of the dispersion perturbation, a^{disp}, to the reference fluid is used to calculate attractive interactions in the fluid. This potential model is described by the chain segment diameter, σ, and the energy of dispersion interactions between segments, ε. For simple non-associating molecules, PC-SAFT utilizes an additional parameter, the number of segments in the non-spherical molecule, m, for a full description of the molecular shape and size. The full mathematical description of dispersion terms are provided in the Appendix (Section 7.1.2).

Dispersion interactions in PC-SAFT are modeled using a two-term perturbation expansion. Both terms in the expansion are dependent on the integral of the radial distribution function. Gross and Sadowski[99] simplified these integrals to a density power series (Equations [56] and [58] in Appendix I, Section 7.1.2) by neglecting to account for the temperature dependence of the hard-chain radial distribution function. After this simplification, these power series depend only on constant coefficients fitted to pure alkane data and the number of segments.

Within this work, the final perturbation to a system that was considered is the associating interactions of a molecule, such as the ability of water to form hydrogen bonds.

The contribution of the association interactions to the Helmholtz energy, a^{assoc}, have been derived based on the Wertheim's perturbation theory. The central conclusion of Wertheim's work was the derivation of the fraction associating sites of a component, X. Chapman et al. later extended this theory and introduced the strength of association between unlike sites, Δ^{AB}. To be able to calculate this quantity, two additional parameters are used: the association energy between sites A and B of molecule i, $\varepsilon^{A_iB_i}$, and the volume of associating interactions, $\kappa^{A_iB_i}$. The full mathematical description of the association term is provided in the Appendix (Section 7.1.3).

In their work on PC-SAFT, Gross and Sadowski[99,100] have calculated all necessary parameters for a variety of non-associating and associating components.

All five parameters described here were fitted to pure component saturation data from temperatures near the triple point to slightly below the critical point. These parameters were fitted by minimizing the difference between the equilibrium pressures and saturated liquid density calculated using the EoS and the experimental values. The fundamental basis of the EoS remains unchanged when multicomponent mixtures are studied by fitting the parameters this way.

A number of other intermediate and long range intermolecular forces such as polarization effects and ionic interactions can be accounted for by the inclusion of additional terms to the expression. Such forces are not accounted for explicitly in this work.

In order to extend PC-SAFT to the prediction for mixtures, the mixing rules in Equations [13] and [14], derived based on the van der Waals mixing rules, are used to describe the dispersion interactions between different molecules[99]:

$$\overline{m^2\varepsilon\sigma^3} = \sum_i \sum_j x_i x_j m_i m_j \left(\frac{\varepsilon_{ij}}{kT}\right)\sigma_{ij}^3 \quad [13]$$

$$\overline{m^2\varepsilon^2\sigma^3} = \sum_i \sum_j x_i x_j m_i m_j \left(\frac{\varepsilon_{ij}}{kT}\right)^2 \sigma_{ij}^3 \quad [14]$$

In these equations, the binary cross interaction parameters, σ_{ij} and ε_{ij}, are calculated using the classical Lorentz-Berthelot combining rules:

$$\sigma_{ij} = \tfrac{1}{2}\left(\sigma_i + \sigma_j\right) \quad [15]$$

$$\varepsilon_{ij} = \sqrt{\varepsilon_i \varepsilon_j}\left(1 - k_{ij}\right) \quad [16]$$

3.3 Derivative Properties

Derivative properties can be calculated directly from the EoS using Equations [17] through [21] in terms of the state variables temperature, pressure and density, ρ.[101,102] These equations represent single phase properties and can be used for both pure components and mixtures.

Isothermal compressibility: $$\kappa_T^{-1} = \rho\left(\frac{\partial P}{\partial \rho}\right)_T \quad [17]$$

Thermal expansion coefficient: $$\alpha = -\kappa_T\left(\frac{\partial P}{\partial T}\right)_v \quad [18]$$

Isochoric heat capacity: $$C_v = -T\left(\frac{\partial^2 \alpha}{\partial T^2}\right)_v \quad [19]$$

Isobaric heat capacity: $$C_p = C_v + \frac{T\alpha^2}{\kappa_T \rho} \quad [20]$$

Speed of sound: $$\omega = \sqrt{\frac{C_p}{C_v}\left(\frac{\partial P}{\partial \rho}\right)_T} \quad [21]$$

The accuracy of the calculation of these properties depends on the ability of the EoS to predict the phase equilibrium. For this reason, it can be expected that a binary interaction parameter fitted to experimental phase equilibrium data will improve the accuracy of the calculations.

3.4 Vapor-Liquid Equilibrium Algorithms

According to Gibbs, the conditions for equilibrium of an arbitrary number of phases is the simultaneous equality of the pressure, P (mechanical equilibrium), temperature, T (thermal equilibrium) and chemical potential, μ (chemical equilibrium) of every component in each phase.[84] Equivalently, chemical equilibrium can be described by the equality of the fugacity of different phases. The fugacity of component *i* in phase *n*, f_i^n, can be calculated using an EoS, based on the following expression:

$$f_i^n = x_i^n \phi_i^n P \qquad [22]$$

where ϕ_i^n is the fugacity coefficient of component *i* in phase *n* and is calculated from the EoS based on the following expression[84]:

$$RT \ln \phi_i = \int_V^\infty \left[\left(\frac{\partial P}{\partial n_i} \right)_{T,V,n_j} - \frac{RT}{V} \right] dV - RT \ln z \qquad [23]$$

Equilibrium properties may be calculated through bubble point or dew point calculations, flash calculations or a stability analysis. In bubble point calculations, the temperature and the composition of the liquid phase are fixed, and through the calculation of the fugacity coefficients using the EoS, the pressure of the system and the composition of the vapor phase are calculated. On the other hand, dew point calculations require foreknowledge of the vapor phase composition in order to calculate the compositions of the components in the liquid phase. Finally, the stability analysis is based on the minimization of Gibbs free energy. This is the concept on which flash calculations are based. In these calculations, the compositions of both phases are unknown, and the temperature and pressure are fixed.

More specifically, in this work, the most commonly considered equilibrium is between a vapor and a liquid phase; the conditions of which are calculated primarily by either bubble point or flash calculations. The bubble point calculations require an initial guess of the pressure and the vapor composition. With these initial estimates, the fugacity coefficients of both phases can be calculated from the EoS. In turn, the vapor compositions of each component are calculated. The function, *g*, in Equation [24], only equates to 1 when the correct pressure is calculated.

$$g = \sum_i y_i = \sum_i x_i K_i \qquad [24]$$

where K_i is the K-factor defined as the ratio of the mole fraction of component *i* in the vapor phase to the mole fraction of component *i* in the liquid phase as expressed in Equation [25].

$$K_i = \frac{y_i}{x_i} = \frac{\phi_i^l}{\phi_i^v} \qquad [25]$$

For the next iteration, the pressure of the system can be calculated according to the Newton-Raphson iteration scheme using Equation [26]. g' is the derivative of the function with respect to pressure and is the expression presented in Equation [27].

$$P^{x+1} = P^x - \frac{g}{g'} \qquad [26]$$

$$g' = \sum_i x_i K_i \left(\frac{\partial \ln \phi_i^l}{\partial P} - \frac{\partial \ln \phi_i^v}{\partial P} \right) \qquad [27]$$

On the other hand, flash calculations are based on the Rachford-Rice equation, for which an initial guess of the K-factor is required. The initial estimate of the K-factor is based on the Wilson correlation[103] and the subsequent calculation of the fraction of each phase, β.

$$f = \sum_i \frac{z_i \left(K_i - 1\right)}{1 + \beta\left(K_i - 1\right)} = 0 \qquad [28]$$

Knowing the phase fraction and mass balance, it is possible to calculate the composition of each phase using Equations [25] and [29]. The quantification of these variables allows for the calculation of the fugacity coefficient of each phase from the EoS and the calculation of the next iteration of the K-factor. The correct vapor and liquid compositions are achieved when their sums are unity, according to the expression in Equation [30].

$$x_i = \frac{z_i}{1 + \beta\left(K_i - 1\right)} \qquad [29]$$

$$\sum_i x_i = \sum_i y_i = 1 \qquad [30]$$

The algorithms used to converge to the equilibrium conditions using bubble point and flash point calculations are shown in Figure 2.

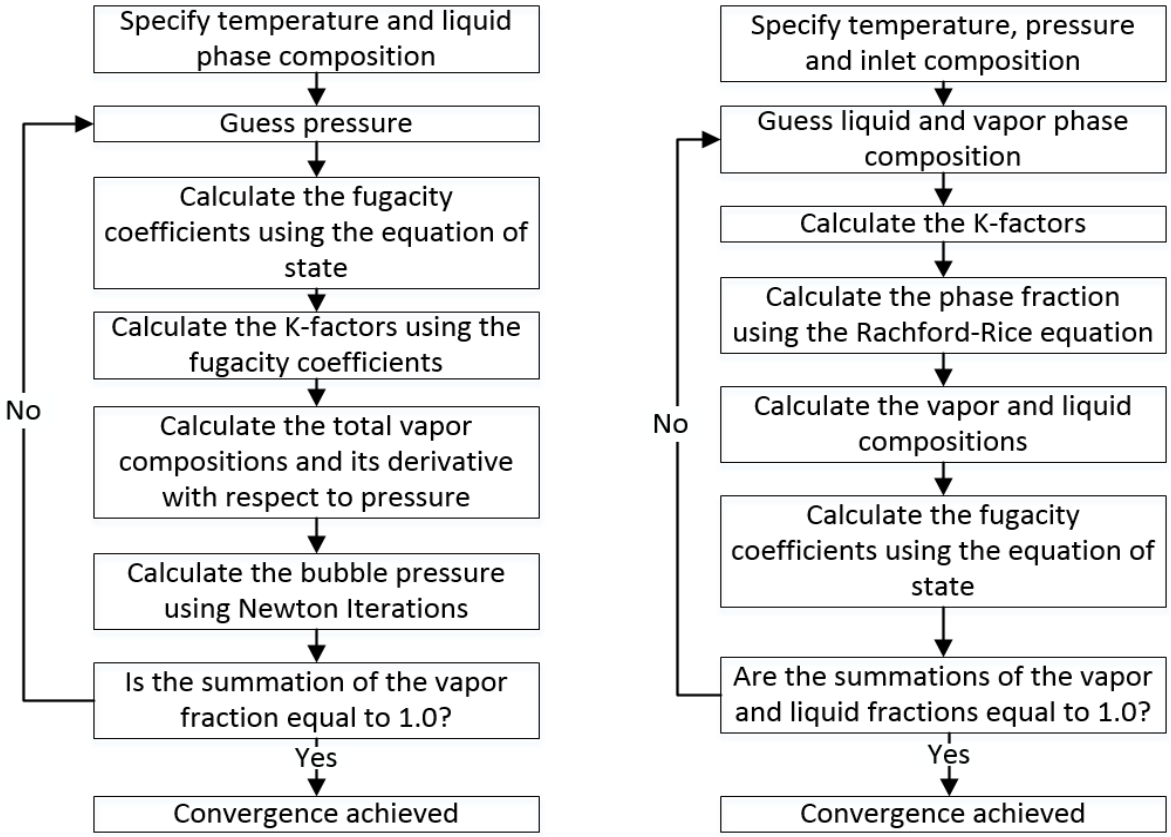

Figure 2. Numerical algorithms for bubble pressure (left) and flash calculations (right)

3.5 Fluid-Hydrate Equilibrium Methodology and Algorithms

Fluid-hydrate equilibrium is modeled based on the equality of the chemical potentials of every component in each of the phases in equilibrium. One such approach is based on the classical van der Waals-Platteeuw (vdW-P) model developed in 1959.[75] The general methodology for the calculation of the equilibrium conditions has been developed in detail by various authors[59–61,75] and is used here to calculate the equilibrium pressure at constant temperature and composition.

The expression developed by van der Waals and Platteeuw for the chemical potential of the hydrate phase, Equation [31], relative to the empty hydrate lattice is defined on the basis of both the fractional occupancy, θ_{ij}, and the number of cavities of type i per water molecule, v_i,

in the hydrate lattice. v_i is a constant which is dependent on the hydrate lattice structure and is defined as the inverse of the number of water molecules per unit cell, the values for each structure type are provided in Table 2.

$$\Delta\mu_H = -RT\sum_{i=1}^{2} v_i \ln\left(1-\sum\theta_{ij}\right) \quad [31]$$

This vdW-P theory is based on the adsorption-like quality of hydrates and uses a multicomponent Langmuir isotherm paired with the Kihara potential to allow for the calculation of the fractional occupancy which is defined as the number of cavities of type *i* occupied by guest molecule of type *j* based on the fugacity, f_j, in the vapor phase.

$$\theta_{ij} = \frac{C_{ij} f_j}{1+\sum_j C_{ij} f_j} \quad [32]$$

The calculation of the fractional occupancy also requires the calculation of the Langmuir constant, C_{ij}, which is based on the calculation of the configurational integral. The Devonshire approximation is used to simplify the integral to the one dimensional from according to Equation [33].

$$C = \frac{4\pi}{kT}\int_0^R \exp\left(-\frac{W_1(r)+W_2(r)+W_3(r)}{kT}\right) r^2 dr \quad [33]$$

where $W_i(r)$ is the smooth cell potentials that account for the intermolecular interactions over the first, second and third shells and are derived based on the Kihara potential.

The classical depiction of the Kihara interaction potential uses three adjustable parameters where a is the radius of the spherical molecular core, ε is the depth of the energy

well and σ is the collision diameter to describe the interaction between a single guest molecule and a single water molecule.[84] This classical description is presented mathematically in Equations [34] and [35] and graphically in Figure 3.

$$\Gamma(r) = \infty, r \leq 2a \qquad [34]$$

$$\Gamma(r) = 4\varepsilon\left[\left(\frac{\sigma}{r-2a}\right)^{12} - \left(\frac{\sigma}{r-2a}\right)^{6}\right], r > 2a \qquad [35]$$

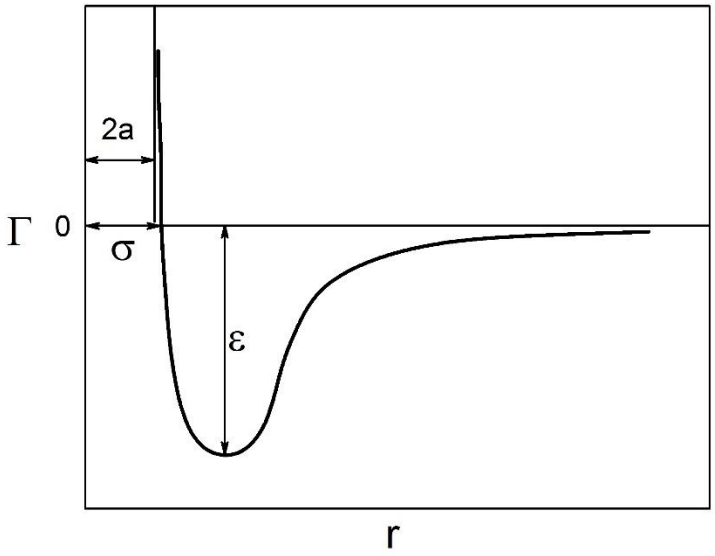

Figure 3. Kihara potential with three adjustable parameters ε, σ, and a

In order to account for the interaction of the guest molecule within the empty hydrate cage and the outer water lattice shells these equations need to be rewritten in the form of a smooth cell potential, $W(r)$, of the form:

$$W(r) = 2Z\varepsilon\left[\frac{\sigma^{12}}{R^{11}r}\left(\delta^{10} + \frac{a}{R}\delta^{11}\right) - \frac{\sigma^{6}}{R^{5}r}\left(\delta^{4} + \frac{a}{R}\delta^{5}\right)\right] \qquad [36]$$

The smooth cell potential is written in terms of the coordination number, Z, the radius of the cell, R, and the distance between the gas molecule and the center of the cavity, r, where δ^n is:

$$\delta^n = \frac{1}{n}\left[\left(1-\frac{r}{R}-\frac{a}{R}\right)^{-n} - \left(1+\frac{r}{R}-\frac{a}{R}\right)^{-n}\right] \qquad n = 4,5,10,11 \qquad [37]$$

The Kihara parameters, a, ε, and σ are characteristic of the guest molecule within the hydrate lattice and can be adjusted to provide a better fit of the model to experimental data. The Langmuir constant, as calculated using the Kihara potential, is disadvantaged in that it can only accurately calculate the hydrate equilibrium conditions of small spherical molecules such as argon, krypton, and methane. In order to be able to account for this deficiency in larger molecules, these parameters can be optimized by fitting them to experimental data of pure hydrate equilibrium as per the algorithm discussed later. However, they do not quantitatively agree with those obtained from the second virial coefficient.

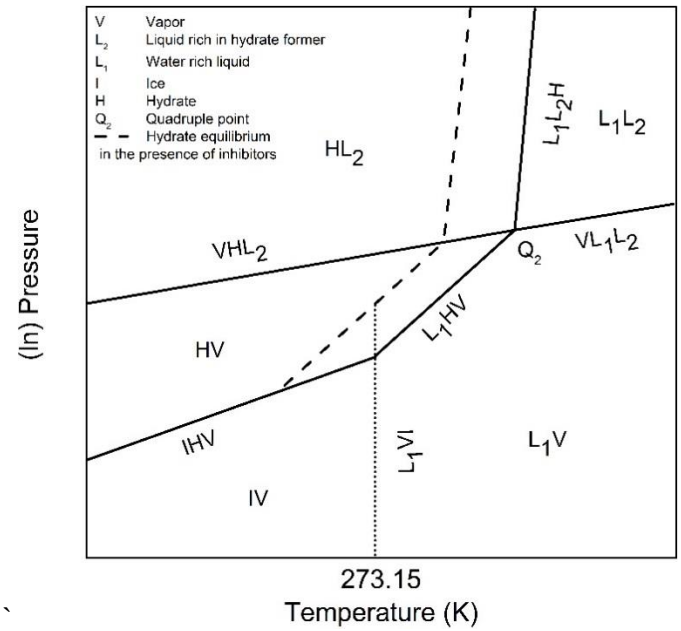

Figure 4. General hydrate-fluid phase equilibrium figure[60]

To satisfy the equilibrium conditions, the chemical potential of water in the hydrate phase is equated to that of water in the coexisting liquid, vapor or ice phase. The focus of this thesis lies in the calculation of the equilibrium between a vapor phase rich in hydrate former, a water-rich liquid phase and the hydrate phase (denoted as L_1HV in Figure 4 or alternatively referred to as L_wHV). To calculate equilibrium between the liquid water and the hydrate phase, the chemical potential of liquid water is needed. An alternative chemical potential formula is required for temperatures less than 273.15 K or calculations of Ice-Hydrate-Vapor (*IHV*) equilibrium.

$$\frac{\Delta\mu_w}{RT} = \frac{\Delta\mu_w^\circ}{RT} - \int_{T_\circ}^{T} \frac{\Delta h_w'}{RT^2} dT + \int_0^P \frac{\Delta V_w'}{RT} dP - \ln\left(\gamma_w x_w\right) \qquad [38]$$

The first term is the reference chemical potential that is defined to be the chemical potential of water at 273.15 K and 0 MPa, and is an experimentally determined value. In order to calculate the chemical potential of the real fluid, the reference potential is corrected to the temperature, pressure and composition of the system. The enthalpy difference is incorporated using the integral of the isobaric heat capacities between the reference temperature and the temperature of the system using Equations [39] and [40].

$$\Delta h_w' = \Delta h_w^\circ + \int_{T_\circ}^{T} \Delta C_p' dT \qquad [39]$$

$$\Delta C_p' = \Delta C_p^\circ + b\left(T - T_\circ\right) \qquad [40]$$

The various thermodynamic reference property values for hydrate structures I and II are given in Table 4. The final term accounts for the solubility of gas of the type *i* in water, x_w, and is calculated using the flash calculation routine. This is the condition that ensures that the hydrate phase is in equilibrium with both the liquid and vapor phases and the activity

coefficient, γ_w, modifies the calculated equilibrium pressure when hydrates are formed in the presence of inhibitors. However, for the purpose of this work, the activity coefficient has been set to unity.

Table 4. Thermodynamic properties defined relative to an empty hydrate lattice[61]

Reference property	Unit	Structure I	Structure II
$\Delta\mu_w^\circ$	J/mol	1263.568	882.824
$\Delta h_w'$	J/mol	1150.6	807.512
$\Delta V_w'$	cm^3/mol	3.0	3.4
ΔC_p°	J/mol.K	$38.14-0.0141(T-T_\circ)$	

In order for the equilibrium pressure to be attained the chemical potentials should be equal, so an iteration scheme is needed to converge to the equilibrium pressure. The algorithm in Figure 5 allows for the implementation of the vdW-P model together with an EoS for the calculation of the hydrate equilibrium pressure in the L_wHV and IHV ranges for both pure gas hydrates and hydrate mixtures. In this work, the use of PC-SAFT and PR EoS for the calculation of hydrate mixture phase equilibria is evaluated.

The calculation of the L_wHV equilibrium in the manner explained in this methodology relies on accurate Kihara parameters. These parameters are fitted to three-phase equilibrium experimental data according to the algorithm in Figure 5. The initial guess of the Kihara parameters are values obtained from the literature, following which they are used to calculate the equilibrium pressure of all data points according the previously explained methodology. The function, g, in the Newton-Raphson scheme is defined based on the average error produced by the current iterations of the Kihara parameters.

$$g = E(x) \qquad [41]$$

The function's derivative is calculated using the finite difference method:

$$g' = \frac{E(x+\Delta x) - E(x-\Delta x)}{2\Delta x} \qquad [42]$$

where Δx is the spacing to the Kihara parameter being fitted and is set to 1.0×10^{-6}.

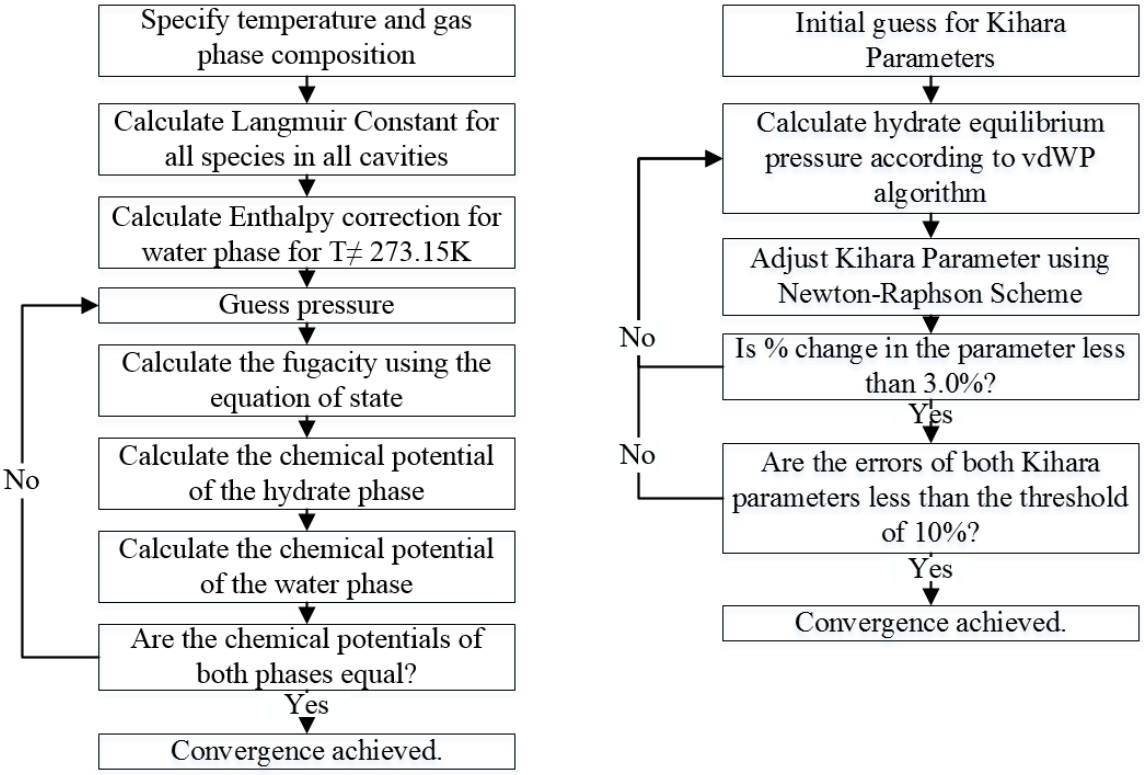

Figure 5. Numerical algorithm for hydrate equilibrium calculations (left) and Kihara parameter regression (right)

3.6 Results Analysis

Within this work, a quantitative comparison of all points calculated using EoS or any alternative modeling method to experimental data is evaluated using an average absolute deviation defined by the formula:

$$\%AAD = \frac{1}{N}\sum_{i=1}^{N}\frac{\left|X_{\text{calc}} - X_{\text{exp}}\right|}{X_{\text{exp}}} \times 100\% \qquad [43]$$

where, N refers to the number of data points in the data set that is being calculated, X refers to the property under consideration such as pressure, heat capacity, speed of sound or isothermal compressibility for either the calculated point (*calc*) or the experimental data point (*exp*). This method normalizes the error and is used for analysis as it allows for equivalent comparison between various different properties.

In addition to the quantitative comparison of the prediction capabilities of the PR and PC-SAFT EoS, a qualitative analysis of the figures is also presented in the next chapter.

4. RESULTS AND DISCUSSION

4.1 Single Component Primary and Derivative Properties

4.1.1 Vapor-Liquid Equilibrium

To calculate thermodynamic properties of fluids in different phases, the pure component PC-SAFT parameters m, σ, ε, ε^{AB} and κ^{AB} need to be fitted to vapor pressure and saturated liquid density data. In this work, experimental data from the National Institute of Standards and Technology[13] (NIST) database was used for this purpose. All molecules studied within this work are modeled as non-associating molecules with the exception of water, which is modeled as a molecule with two associating sites. The optimization of these parameters is achieved through the minimization of the deviation of the EoS prediction of both the saturation pressure and liquid density of the components from the experimental value. The parameters for all of the components studied in this work are displayed in Table 5. These parameters have been refitted for this work and are consistent with the parameters previously published by the research group at Texas A&M university at Qatar.[104,105]

The accuracy of these parameters is ensured by the subsequent calculation of the saturation pressure, P^{sat}, and the liquid and vapor densities, ρ^{liq} and ρ^{vap}, respectively. Table 6 provides a summary of the %AAD for each property, the number and range of conditions of the data used to fit the PC-SAFT parameters. The saturation curves, presented in both Figure 6 and Figure 7, are those of select pure components and provide an indicative sample of the qualitative value of the fitted parameters.

Table 5. PC-SAFT pure component parameters

Component	MM [g/mol]	m	σ [Å]	ε/κ [K]	ε^{AB}/κ [K]	κ^{AB}
CO_2	44.01	2.6037	2.555	151.04		
CH_4	16.04	1.0000	3.704	150.03		
O_2	32.00	1.1217	3.210	114.96		
Ar	39.95	0.9285	3.478	122.23		
N_2	28.00	1.2053	3.313	90.96		
CO	28.01	1.3195	3.231	91.41		
H_2O	18.02	1.9599	2.362	279.42	2059.28	0.1750
H_2S	34.08	1.7129	3.053	224.01		
C_2H_6	30.07	1.6040	3.532	191.47		
C_3H_8	44.10	2.0011	3.630	207.90		
i-C_4H_{10}	58.12	2.2599	3.774	216.25		

On average, PC-SAFT systematically predicts the saturated liquid and vapor densities of all components more accurately than the PR EoS for temperatures slightly above the triple point to almost critical conditions. For SAFT type EoS, %AAD less than 2% are expected which is in accordance with the results obtained for PC-SAFT.[99,106] Higher errors are expected from the PR EoS, especially when the liquid density is considered. For this reason, the implementation of the Peneloux density correction for improvement of the liquid phase density prediction is usually preferred.

Both PC-SAFT and PR EoS are mean-field models and they are inaccurate at near critical conditions. Figure 6 provides an overview of the accuracy of PC-SAFT for CO_2 at conditions away from the critical point (both sub- and supercritical conditions) and the relative inaccuracy at near critical conditions.

Table 6. Pure component densities calculated by PC-SAFT

Species	Number of Data Points	Temperature Range [K]	PC-SAFT			PR	
			P^{sat} [MPa]	%AAD ρ^{liq}	%AAD ρ^{vap}	%AAD ρ^{liq}	%AAD ρ^{vap}
CO_2	88	217 -304	0.37	0.86	3.56	4.38	0.57
CH_4	99	92-190	0.27	0.77	0.90	9.47	0.62
O_2	99	56-154	1.48	0.98	0.38	9.79	0.70
Ar	66	85-150	0.37	1.06	0.80	9.14	1.17
N_2	63	64-126	0.26	2.16	0.76	9.36	1.08
CO	64	69-132	0.34	1.73	0.45	9.68	1.31
H_2O	187	274-646	1.20	4.11	6.36	19.04	2.87
H_2S	93	188-372	0.30	4.77	0.82	6.11	0.65
C_2H_6	108	91-305	4.05	0.49	1.27	6.91	0.37
C_3H_8	142	150- 368	0.33	1.19	1.22	10.60	0.30
i-C_4H_{10}	147	114-406	1.04	1.26	1.33	7.68	0.32
		Averages	**0.91**	**1.71**	**1.79**	**8.74**	**0.93**

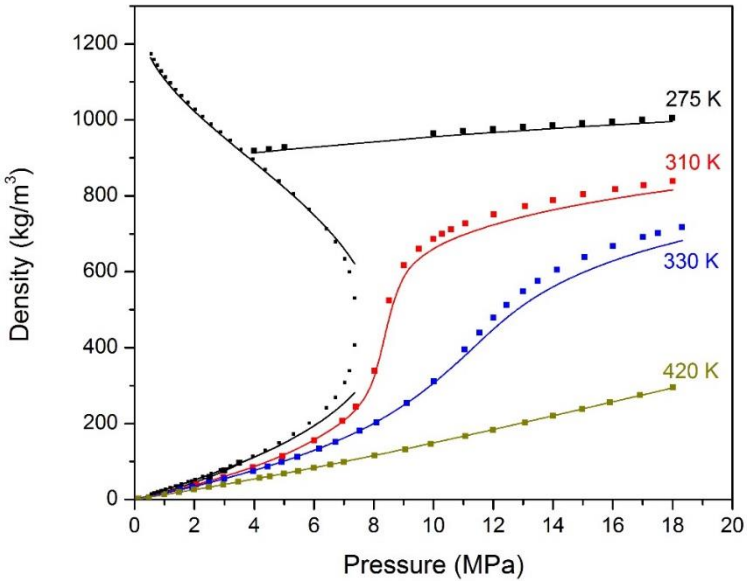

Figure 6. Density of CO_2 at four isotherms ranging from below to above T_c, experimental data (points) and PC-SAFT model predictions (lines)

The density curves in Figure 7 reiterate this point qualitatively for several other components showing that all EoS perform equally well for the vapor phase but not for the liquid phase.

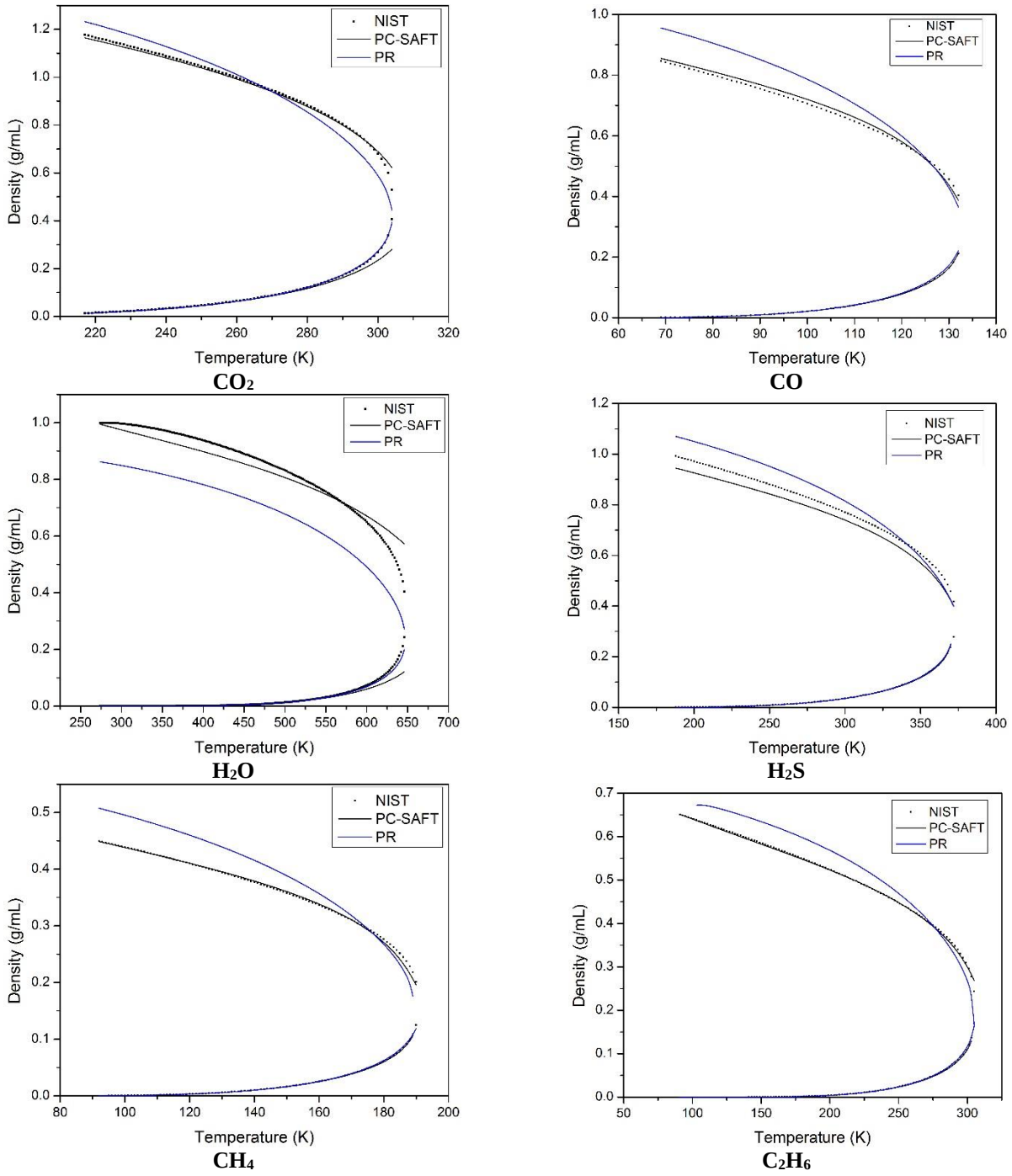

Figure 7. Phase equilibrium density diagrams for select pure component species examined in this thesis

4.1.2 Derivative Properties of Single Component Systems

Derivative properties, such as isothermal compressibility and speed of sound, are directly related to the isobaric, C_p, and isochoric, C_v, heat capacities. Thus, a proper

understanding of the abilities of both EoS to predict C_p and C_v is essential. Overall, both PC-SAFT and PR can predict these properties with relatively good accuracy, with, on average, errors less than 4.5%. The individual %AAD for each component are listed in Table 7; these are averages taken over a range of temperatures that include the critical temperature of the component and six isobars ranging from 2-12 MPa.

Table 7. Percentage average absolute deviations in EoS predictions of pure component isochoric and isobaric heat capacities and the corresponding residual properties

Components	Temperature Range [K]	PC-SAFT				PR			
		C_p	C_p^{res}	C_v	C_v^{res}	C_p	C_p^{res}	C_v	C_v^{res}
CO_2	220-500	3.83	10.28	4.80	39.33	3.90	12.14	3.05	24.35
CH_4	100-300	3.27	7.06	3.02	21.32	3.27	7.17	3.34	30.42
O_2	70-200	5.07	9.80	4.99	25.28	4.81	9.52	3.82	25.32
Ar	90-200	5.92	9.94	5.18	20.88	5.12	8.81	5.80	29.02
CO	80-200	3.73	6.69	3.54	16.31	3.61	6.95	2.89	16.56
N_2	75-200	3.79	7.07	4.06	21.92	3.58	6.94	3.05	21.06
	Averages	**4.27**	**8.47**	**4.26**	**24.17**	**4.05**	**8.59**	**3.66**	**24.46**

However, these deviations may be a little misleading as they include the ideal contribution to the EoS. Once this contribution is eliminated, the residual property is calculated.

$$X^{res}(T,P) = X(T,P) - X^{ideal}(T,P) \qquad [44]$$

where X refers to any arbitrary property under consideration, in this case, $X = C_p$ or C_v.

The substantial increase in error in both residual C_p and C_v indicate that the prediction capabilities of both EoS are relatively poor. For C_p, the error increases as a result of the asymptotic behavior of the property at the critical point. This behavior is exhibited by the experimental data measured in the critical region and is mimicked by both EoS. This phenomenon can be seen in Figure 8 which is representative of the behavior of C_p around the

critical point for all the components studied. The figures for the other components have been compiled in the Appendix (Section 7.2.1). C_p calculations for all components exhibit the same behavior, where both EoS are accurate in regions away from the critical point but deteriorate in the critical region. This is due to the fact that both EoS are mean-field theories and as such do not account for critical fluctuation.

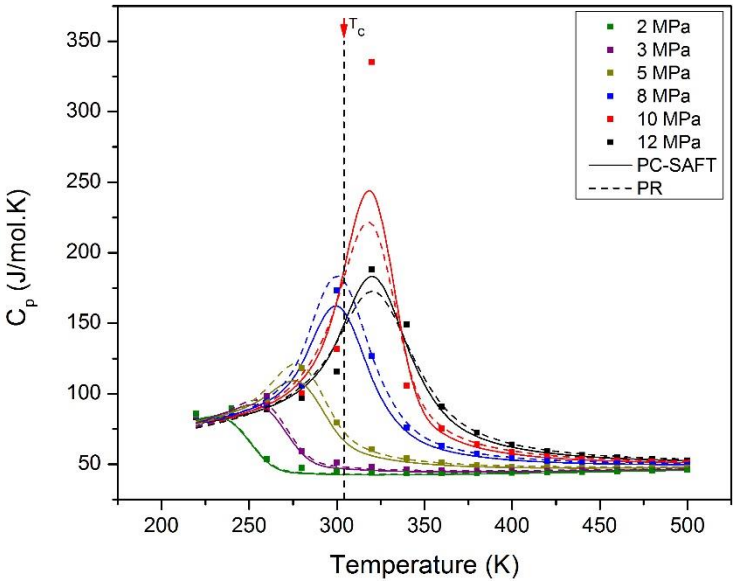

Figure 8. Isobaric heat capacity (C_p) of CO_2, experimental data (points) and model predictions (lines)

Similarly, the significant increase in the error in residual C_v is also due to the approach to the critical point. However, unlike C_p the EoS entirely lose their predictive capabilities. Outside the critical region, the behavior is more consistent. For example, at temperatures above 400 K, each isobar is in the supercritical phase. Deviations are to be expected at lower temperatures as the critical region, phase transitions, and low temperatures exhibit highly non-ideal behavior.

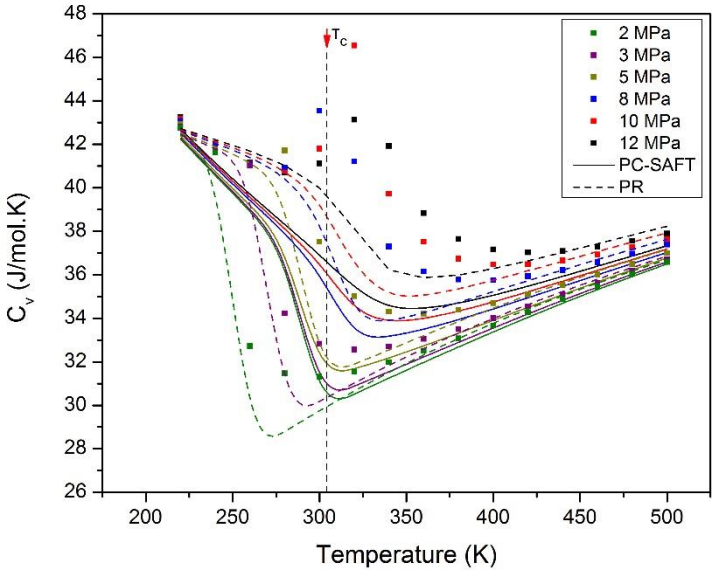

Figure 9. Isochoric heat capacity (C_v) of CO_2, experimental data (points) and model predictions (lines)

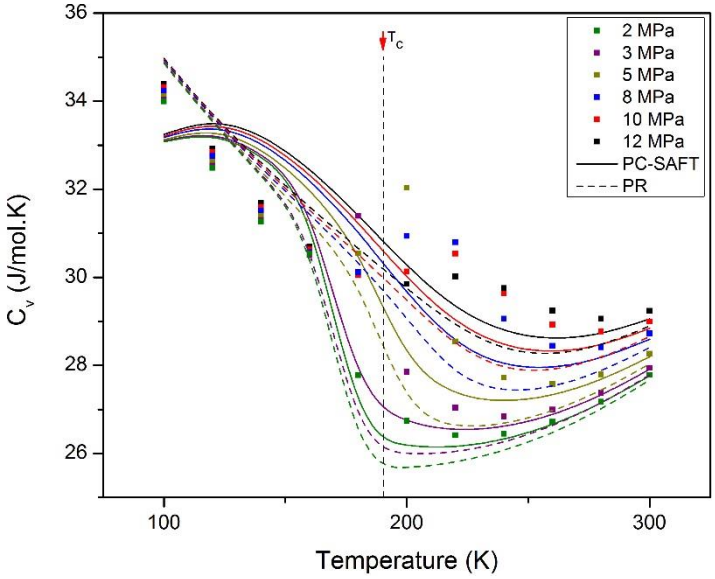

Figure 10. Isochoric heat capacity (C_v) of CH_4, experimental data (points) and model predictions (lines)

The speed of sound and the isothermal compressibility of pure carbon dioxide are studied in the high-pressure liquid region indicated by Figure 11. Specifically, six isotherms ranging in temperature from 268.15 to 301.15 K and in pressure from approximately 3 to 42 MPa.

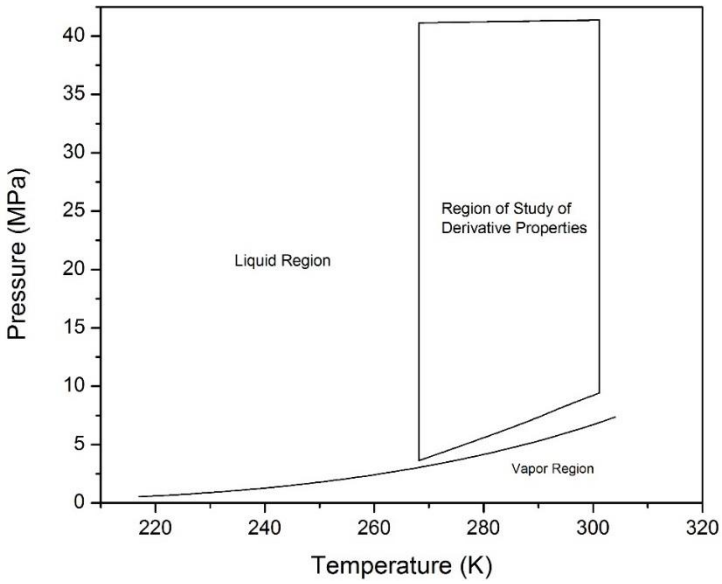

Figure 11. Temperature and pressure region of experimental data points of derivative properties compared to the saturation curve of CO_2

This range of conditions is typical of a CCS process stream. In this range, the common impurities found in CCS streams are typically supercritical. As the impurities are supercritical in the temperature and pressure regions under consideration, a different behavior of the single phase properties for these components should be expected.

The %AAD for each of the pure component speed of sound calculations are in Table 8 for both the PC-SAFT and PR EoS. The phase of the impurities makes their derivative properties easier to predict relative to the prediction of properties of pure liquid CO_2. This results in an appreciably lower %AAD of the components in the supercritical phase compared to CO_2. This behavior is true of both EoS, although PC-SAFT does so with more precision. On average, PC-SAFT is able to predict the speed of sound in the supercritical phase with a %AAD of 1.2%, PR with a %AAD of 4.5%. These percentages account for almost a third of the error for prediction of the same property in the liquid phase as documented in Table 8. The error for

the isothermal compressibility of pure liquid CO_2 is higher with %AAD for 4.18% with PC-SAFT and 39.23% with PR.

Table 8. Deviations in pure component speed of sound by both EoS for the component in the indicated phase for temperatures ranging from 268.15 K to 301.15 K and pressures ranging from 3.63 MPa to 41.64 MPa

Component	Phase	%AAD PC-SAFT	% AAD PR
CO_2	Liquid	3.86	15.56
CH_4	Supercritical	1.73	5.68
O_2	Supercritical	0.76	3.45
Ar	Supercritical	0.88	3.74
CO	Supercritical	1.05	4.56
N_2	Supercritical	1.63	4.83

While PC-SAFT accurately predicts the trends of both isothermal compressibility and speed of sound over broad conditions, it can also follow the data patterns of both properties. Overall, PC-SAFT tends to over-predict the properties under consideration. This can be seen explicitly in Figure 12 in the low pressure region.

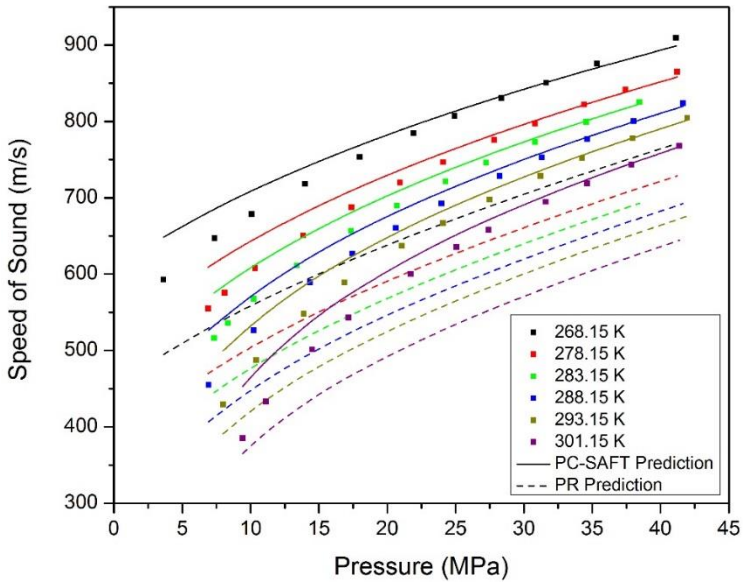

Figure 12. Speed of sound of CO_2, experimental data (points) and model predictions (lines)

As the critical point is crossed and the speed of sound of a supercritical fluid is calculated in the high pressure spectrum, PC-SAFT begins to slightly under predict the property. This can be seen qualitatively in Figure 13.

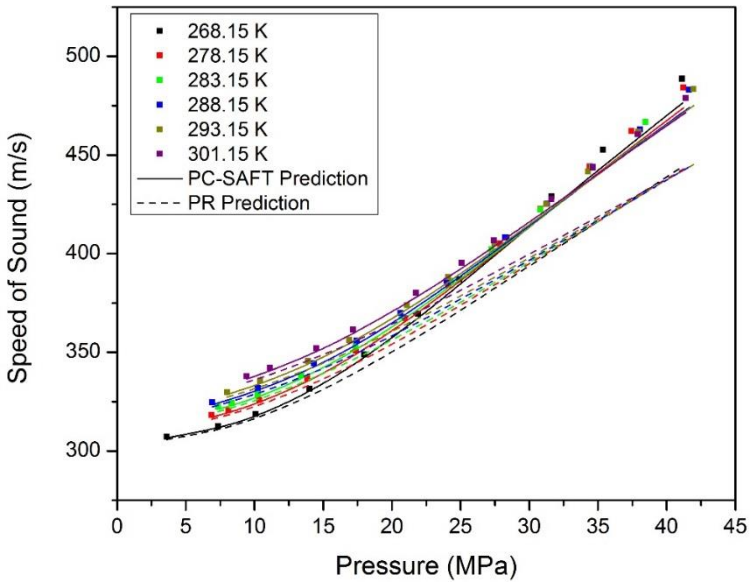

Figure 13. Supercritical speed of sound of Ar, experimental data (points) and model predictions (lines)

On the other hand, in both of the previously presented figures PR consistently under-predicts the speed of sound. Both EoS lose their accuracy in the low-pressure region as saturation conditions are reached and variations in temperature have a much smaller effect on the speed of sound of supercritical species compared to those in subcritical conditions.

For isothermal compressibility, PC-SAFT remains consistent in its trends as seen in Figure 14. It over predicts the property at low pressures and becomes more accurate at high pressures in the liquid phase calculations. Similarly, PR also over predicts the isothermal compressibility, this is contrary to its behavior in the prediction of speed of sound.

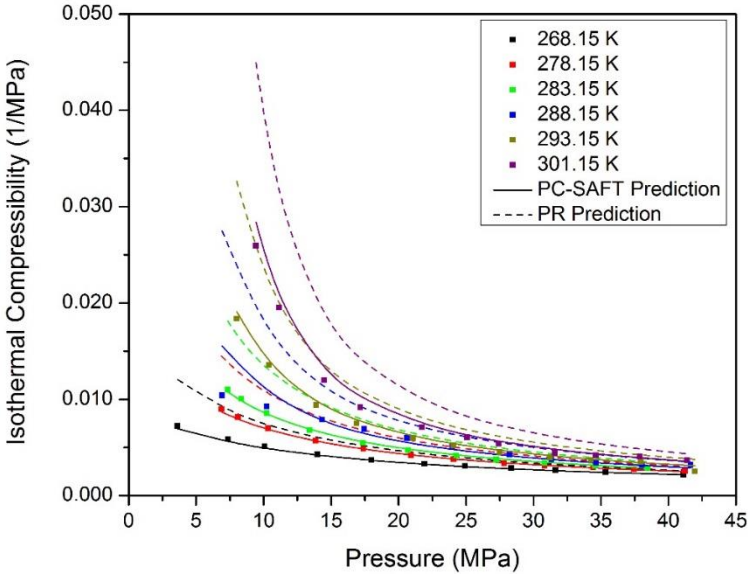

Figure 14. Isothermal compressibility of CO_2, experimental data (points) and model predictions (lines)

The figures presented in this section are of select pure components and provide an illustration of the qualitative behavior of both properties. Additional figures of the properties of the remaining components have been placed in Appendix II (Section 7.2.4). The conclusions that can be drawn from the figures presented in the Appendix are indentical to the conclusions discussed here.

4.2 Binary and Select Ternary Mixtures Relevant to CCS

4.2.1 Vapor-Liquid Equilibrium of Binary Mixtures

Pure component VLE calculations are relatively easy to perform, and the algorithms are robust. Increasing the number of components in the system increases the complexity of the calculations. More specifically, this section focuses on the study of the degree of improvement observed in VLE calculations with the implantation of a binary interaction parameter, k_{ij}. The binary interaction parameters are independent of temperature meaning that to be able to use

them with confidence for the prediction of other properties, they should be fitted to as wide a temperature range as possible.

Figure 15 display the ability of PC-SAFT to predict the VLE region for the binary mixture of CO_2-CH_4. The results of four cases of calculations, a set of prediction and correlation calculations using both the PC-SAFT and PR EoS are presented. It can be concluded qualitatively that both EoS become more accurate after the implementation of the binary interaction parameter.

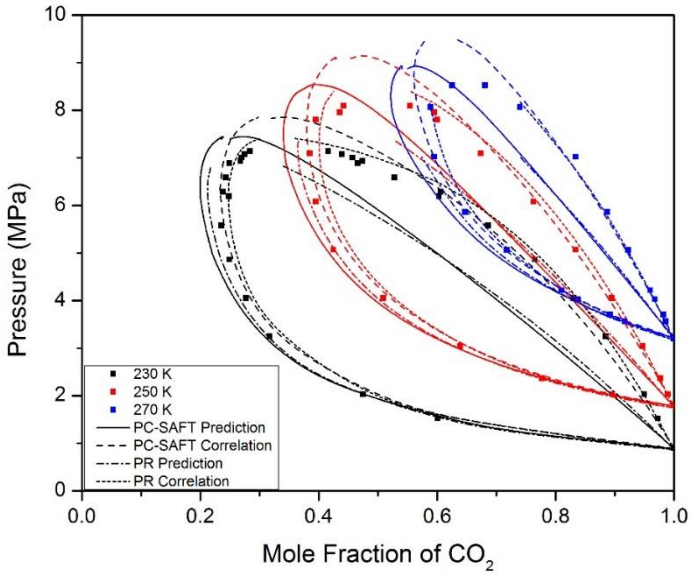

Figure 15. VLE for the binary mixture CO_2-CH_4 mixture, experimental data (points) and model predictions (lines)

The VLE diagrams for the remaining five systems studied in this work are summarized in Appendix II (Section 7.2.3). The results presented there are consistent with those presented in the following section. The binary interaction parameter was fitted for all six mixtures over as wide a range of temperatures as possible. The k_{ij} parameters for both EoS are summarized in Table 9. These parameters have been refitted specifically for this work, but they do not differ significantly from those fitted previously.[105]

Table 9. Average deviations of VLE pressures and binary interaction parameters (k_{ij}) for mixtures relating to CCS

			PC-SAFT	k_{ij}=0	k_{ij}≠0	PR	k_{ij}=0	k_{ij}≠0
System	#DP	T Range [K]	k_{ij}	%AAD Pressure	%AAD Pressure	k_{ij}	%AAD Pressure	%AAD Pressure
CO_2-CH_4[19]	36	230-270	0.0561	14.52	3.71	0.1000	14.87	2.48
CO_2-O_2[28]	71	223-283	0.0488	18.50	5.07	0.1050	22.87	5.14
CO_2-Ar[14]	62	233-299	0.0439	10.99	3.73	0.1200	23.93	8.58
CO_2-CO[107]	38	223-283	-0.0161	9.62	6.51	-0.0200	13.30	8.16
CO_2-N_2[18]	14	223-273	-0.0105	6.73	5.40	-0.0177	6.90	3.90
CO-Ar[108]	15	123-137	-0.0012	0.66	0.64	0.0010	0.75	0.68
			Average	10.17	4.18		13.77	5.23

Based on the results summarized in Table 9, PC-SAFT is able to predict the VLE pressure for a binary mixture with an average accuracy of 10.17%; however, when the k_{ij} is fitted to these data the average deviation between experimental data and model calculations for the pressure decreases to 4.18%. The prediction ability of the PR EoS shows similar improvement with %AAD decreasing from 13.77% to 5.23% upon fitting of the k_{ij}. These errors are still large compared to the predictions of pure componenet vapor pressure. Both EoS algorithms show a loss of accuracy as the critical point of the mixture is approached; a phenomenon that can also be seen in the pure component saturation curves in Figure 7. With the fitting of the k_{ij}, a more accurate calculation of VLE curve in the region around the critical point is possible.

4.2.2 Derivative Properties of Mixtures

Accurate calculation of second order derivative properties are a well-known challenge for any EoS.[55] Assuming that the binary interaction parameter would also work as well for improving calculations of the speed of sound and isothermal compressibility as it has for VLE calculations. Calculations of properties with and without the parameter are presented. The

following analysis describes the effect of the binary interaction parameters of derivative property predictions for the five binary and single ternary mixtures, the compositions for which are noted in Table 10.

Table 10. Composition of mixtures for which second order derivative properties are studied

	CO_2+N_2	CO_2+CH_4	CO_2+O_2	CO_2+Ar	CO_2+CO	CO_2+Ar+CO
CO_2	0.9556	0.9539	0.9348	0.9554	0.9569	0.9884
N_2	0.0444					
CH_4		0.0461				
O_2			0.0652			
Ar				0.0446		0.0116
CO					0.0431	0.0229

Based on the results summarized in Table 11, the use of the binary interaction parameter only slightly improves both predictions of speed of sound and isothermal compressibility with PC-SAFT. However, the same conclusion cannot be reached for PR, as the %AAD increases with the implementation of the binary interaction parameter, which is unexpected.

Table 11. Average deviation (%AAD) in speed of sound and isothermal compressibility predictions using PC-SAFT and PR

Mixtures	#DP	Predictions (k_{ij}=0)				Correlations ($k_{ij} \neq 0$)			
		Speed of Sound		Isothermal Comp		Speed of Sound		Isothermal Comp	
		PC-SAFT	PR	PC-SAFT	PR	PC-SAFT	PR	PC-SAFT	PR
CO_2+CH_4	61	6.53	13.30	7.81	31.40	5.41	14.10	5.70	35.89
CO_2+O_2	62	4.98	13.42	4.42	28.35	4.08	14.26	4.06	32.53
CO_2+Ar	59	4.40	14.31	6.15	28.67	3.83	14.96	5.52	31.94
CO_2+CO	61	5.84	13.24	6.82	28.11	6.07	13.15	7.38	27.63
CO_2+N_2	60	2.99	15.74	3.81	36.77	3.09	15.73	3.52	36.72
CO_2+Ar+CO	58	7.62	13.51	11.53	27.72	7.48	13.62	11.19	28.24
Average		**5.39**	**13.92**	**6.76**	**30.17**	**4.99**	**14.30**	**6.23**	**32.16**

An analysis of the Figure 16 indicates that PC-SAFT over-predicts the speed of sound while PR under-predicts the property. The use of the binary interaction parameter has the net

effect of reducing the speed of sound of the system. This shift the PC-SAFT correlation closer to the experimental value but shifts the PR correlation away from the datasets. Thus, reducing the %AAD of the PC-SAFT prediction and increasing that of the PR.

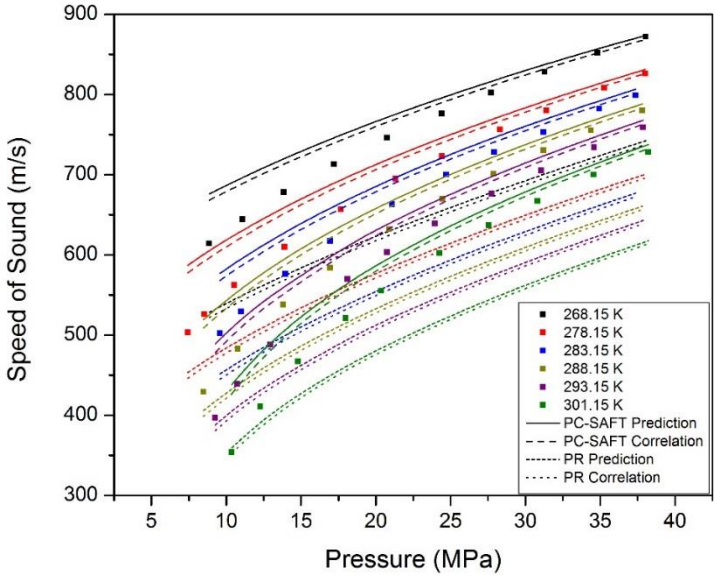

Figure 16. Speed of sound of the CO_2 -CH_4 mixture, experimental data (points) and model predictions (lines)

On the other hand, PR always overestimates isothermal compressibility. Here again, the use of the binary interaction parameter increases both EoS predictions of the property. This leads to the further deviation of the PR EoS prediction from the experimental data. However, this does not lead to increasing %AAD for PC-SAFT as the EoS tends to only over predict the property at high temperatures. Thus, introducing the binary interaction parameter only furthers deviations in the PC-SAFT prediction of isothermal compressibility at temperatures above 301 K.

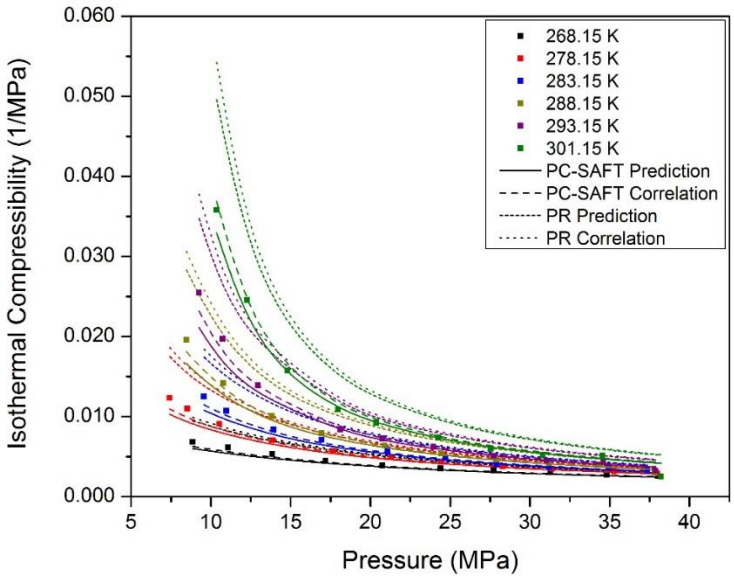

Figure 17. Isothermal compressibility of the CO_2 -CH_4 mixture, experimental data (points) and model predictions (lines)

Overall, it may be concluded that the implementation of the binary interaction parameter in the prediction of derivative properties has a negligible effect on the accuracy of the EoS. A similar analysis may be concluded from the remainder of the binary mixtures, the figures for which are provided in Appendix II (Section 7.2.5). More importantly, the analysis remains the same for the results of the ternary mixture of CO_2-Ar-CO that was studied. The results for this ternary mixture are displayed in Figure 18 and Figure 19. Three k_{ij} values were used each of which were fitted to binary VLE data, in a manner consistent with the binary mixtures studied in this section. Based on the results summarized both in the figures below and in Table 11, the use of the k_{ij} parameter has even smaller effect on the prediction of the properties compared to its effect on the properties of the binary system.

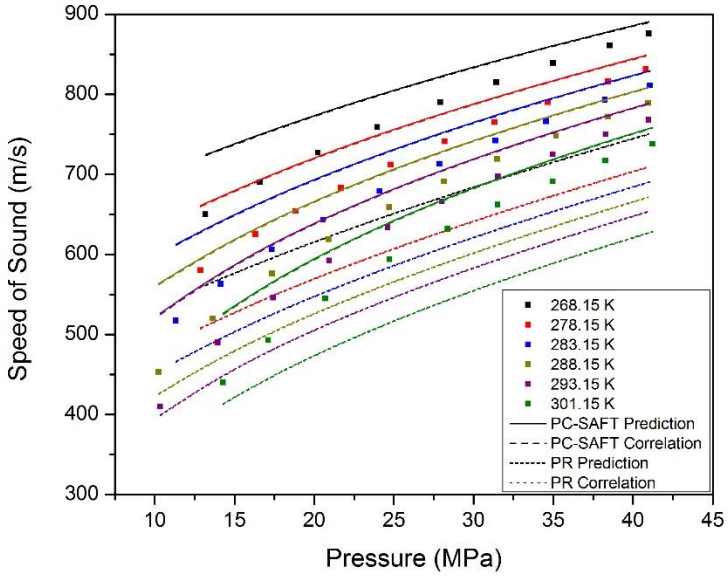

Figure 18. Speed of sound of the CO_2 –Ar – CO mixture, experimental data (points) and model predictions (lines)

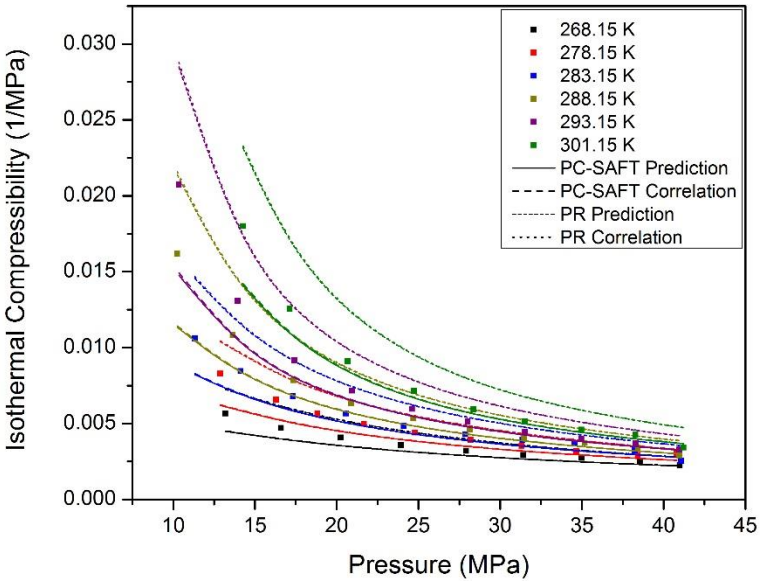

Figure 19. Isothermal compressibility of the CO_2 –Ar – CO mixture, experimental data (points) and model predictions (lines)

4.3 Fluid-Hydrate Equilibrium

4.3.1 Pure Hydrate Formers

The primary focus of this section lies in the prediction of the equilibrium pressure of the hydrate phase with a liquid and a vapor phase. The liquid is primarily composed of water, and the vapor phase is rich in the guest molecule used to stabilize the hydrate phase. For example, in the case of methane, the system under study would consist of the hydrate phase with guest methane molecules, a liquid water phase with a low concentration of dissolved methane molecules, and a methane-rich vapor phase. The correct compositions of the vapor and liquid phases are determined using the 2-phase flash algorithm outlined in Section 3.4. The composition is then used in Equation [38] to ensure simultaneous equilibrium with the hydrate phase.

In order to describe the hydrate phase properties with the model formulated in Section 3.5, two cases of Kihara potential parameters (a, ε and σ) provided in the literature are studied. The first set of parameters were proposed by Parish and Prausnit[61,109] (P&P) and the second are those presented by Sloan and Koh[59] (S&K). The relevant parameters are summarized in Table 12. For the case of S&K there are no parameters available for Ar or O_2. For Ar, an alternative set was obtained from literature while those of O_2 have been designated "N/A" as no secondary set of parameters was found.

Using these parameters, calculations of the equilibrium pressure were performed for the systems and under the ranges of conditions summarized in Table 13. Calculations were performed between the lower and upper quadruple points. The quadruple points are conditions under which L_wHV phases are in equilibrium with a fourth phase. The first quadruple (Q1)

point has these phases in equilibrium with an ice phase (I) whereas the second quadruple point (Q2) occurs when L_wHV is equilibrium with a second guest-rich liquid phase (L_g).

Table 12. Kihara potential parameters from P&P and S&K. Sources of parameters are those listed in column headings unless cited otherwise.

Guest Molecule	Parrish and Prausnitz[61,109]			Sloan and Koh[59]		
	a [Å]	ε/k (K)	σ (Å)	a [Å]	ε/k (K)	σ (Å)
CH_4	0.300	153.17	3.2398	0.3834	155.59	3.1439
C_2H_6	0.400	174.97	3.2941	0.5651	188.18	3.2469
C_3H_8	0.680	200.94	3.3030	0.6502	192.86	3.4167
iC_4H_{10}	0.800	220.52	3.1244	0.8706	198.33	3.4169
CO_2	0.3600	169.09	2.9681	0.6805	175.41	2.9764
O_2	0.3600	166.37	2.7673	N/A		
N_2	0.3500	127.95	3.2199	0.3526	127.43	3.1351
Ar	0.184	170.50	2.9434	0.4520 [110]	155.30 [110]	2.829 [110]
H_2S	0.3600	205.85	3.1558	0.3600	212.05	3.1000

Table 13. Conditions of pure guest hydrate formation in L_wHV region

Guest Species	Experimental Data Sources	#DP	Temperature Range [K]	Pressure Range [MPa]	L_wHVL_g Point [Q2]	
					T [K]	P [MPa]
CH_4	Deaton and Frost[111] and Marshall et al.[112]	33	273.70-320.10	2.77-397.00	--	
C_2H_6	Holder et al.[60]	24	273.15-284.65	0.47-2.10	287.35	3.303
C_3H_8	Holder et al.[60]	21	273.15-278.15	0.18-0.54	278.40	0.560
iC_4H_{10}	Rouher and Barduhn[113]	21	273.15-274.80	0.12-0.16	275.03	0.167
CO_2	Holder et al.[60]	21	273.15-283.15	1.12-4.43	283.10	4.502
O_2	Van Cleeff et al.[114]	42	269.15-291.05	10.94-95.85	--	
N_2	Holder et al.[60]	25	273.15-298.15	15.09-166.06	--	
Ar	Marshall et al.[112]	13	274.32-299.98	10.65-207.84	--	
H_2S	Holder et al.[60]	12	273.65-295.65	0.10-0.96	302.70	2.239

The deviations in the ability of both EoS to predict the equilibrium pressure of L_wHV phases are summarized in Table 14.

Table 14. Average deviation in EoS prediction of equilibrium pressure of pure gas hydrates

Guest Species		PC-SAFT		PR		CSMGem
		P&P	S&K	P&P	S&K	
CH_4	Figure 24	11.12	11.04	6.86	7.41	1.94
C_2H_6	Figure 57	19.97	(1)	20.05	(1)	2.40
C_3H_8	Figure 56	4.97	22.04	4.90	22.00	10.85
iC_4H_{10}	Figure 23	1.04	51.19	1.17	51.18	4.06
CO_2	Figure 22	(1)	48.60	(1)	50.57	3.78
O_2	Figure 55	57.68	N/A	64.25	N/A	N/A
N_2	Figure 54	2.24	26.46	6.61	41.36	7.12
Ar	Figure 25	(1)	52.74	(1)	52.92	N/A
H_2S	Figure 58	3.46	4.58	5.49	2.86	5.67
	Averages	**14.35**	**30.95**	**15.63**	**32.61**	**5.12**

(1) These calculations did not converge.

Of the parameters studied, three cases denoted with (1) did not converge. This instability is most likely due to an insufficient or inaccurate description of the collision diameter, well depth or soft-core radius. An immediate comparison of the values provided in Table 12 indicates that the divergence in C_2H_6 and Ar is caused by the given values of the radius, a, while the divergence in CO_2 calculations may be caused by the combination of ε and σ. From these preliminary calculations, it is apparent that the P&P parameters are better optimized compared to those of S&K. However, both sets of parameters perform poorly compared to the predictions of CSMGem, also shown in Table 14. CSMGem a commercialized software that calculates equilibrium conditions using a routine based on the minimization of Gibbs free energy.[115]

In order to improve the accuracy of these predictions, the Kihara potential well depth, ε, was fitted to experimental L_wHV equilibrium data using the iteration scheme described in Section 3.5. For all of the cases examined, the adjusted ε parameters are presented in Table 15.

Table 15. Fitted Kihara epsilon parameter for all cases and average deviation in EoS prediction of equilibrium pressure

Guest Species	PC-SAFT				PR				CSMGem
	r. P&P		r. S&K		r. P&P		r. S&K		
	ε	%AAD	ε	%AAD	ε	%AAD	ε	%AAD	
CH_4	153.17	11.12	155.59	11.04	153.77	6.21	156.45	5.87	1.94
C_2H_6	171.35	9.89	(1)		172.24	7.40	(1)		2.40
C_3H_8	199.98	3.25	189.82	3.25	200.35	0.46	190.17	0.42	10.85
iC_4H_{10}	220.55	0.91	190.93	1.09	220.61	0.72	(1)		4.06
CO_2	(1)		165.92	9.26	188.07	7.53	166.47	5.80	3.78
O_2	170.95	16.46	N/A		174.02	13.88	N/A		N/A
N_2	128.08	2.24	131.05	2.56	128.52	6.61	131.59	4.67	7.12
Ar	(1)		143.86	8.99	(1)		145.17	8.23	N/A
H_2S	204.49	3.46	211.34	9.81	205.01	2.02	211.89	2.53	5.67
Averages	**6.76**		**6.57**		**5.59**		**4.87**		**5.12**

For the cases of CH_4, N_2, and H_2S, the values of ε regressed by the routine described in Section 3.5 are the same as those originally proposed in Table 12. To evaluate the sensitivity of the Kihara parameter values in the phase equilibrium calculations, the error in hydrate-fluid equilibrium pressure produced by varying each of the Kihara parameters is presented. For the case of CH_4, %AAD are calculated and plotted against the Kihara ε and Kihara σ in Figure 20 and Figure 21, respectively.

From Figure 20, it may be concluded that the original value of the Kihara ε results in the global error minimum when paired with the PC-SAFT EoS. However, when the same parameters are used to describe the hydrate phase in conjunction with the PR EoS a different value of ε produces a global error minimum. This behavior indicates that the optimum value of ε is EoS dependent; the same conclusion was reached by Diamantonis et al.[64] In addition, by varying σ (solid to dashed lines) by 3% no notable improvement or loss of accuracy in the prediction capabilities of either EoS is seen. This analysis is also evident in a similar investigation of N_2 and H_2S hydrates.

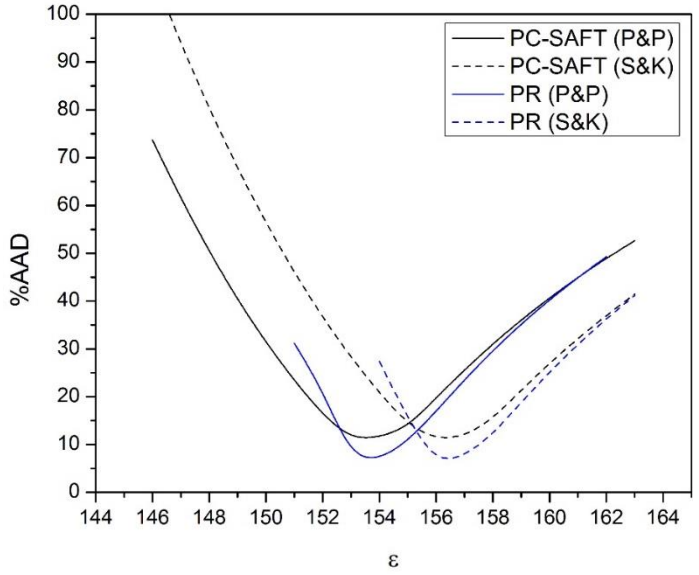

Figure 20. %AAD of CH_4 hydrate-fluid equilibrium with change in Kihara ε

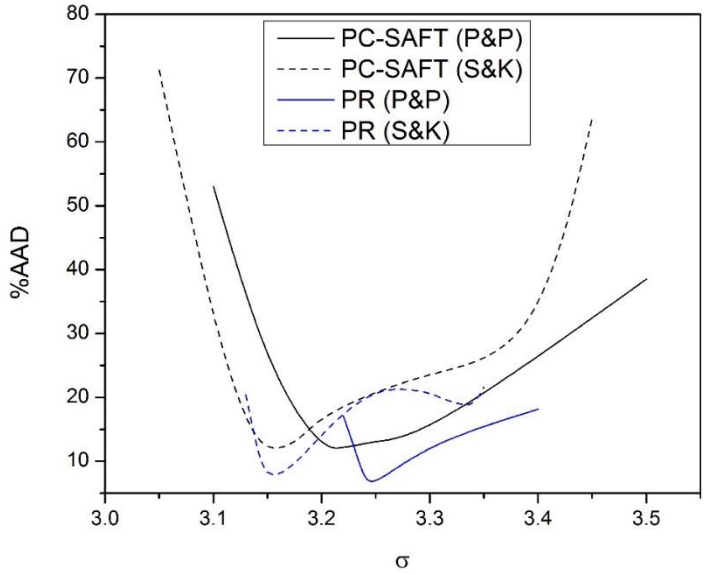

Figure 21. %AAD of CH_4 hydrate-fluid equilibrium with change in Kihara σ

Furthermore, an analysis of Figure 20 and Figure 21 provides information on the sensitivity of %AAD to small changes in σ and ε. PR EoS is more sensitive to changes in both Kihara parameters than PC-SAFT, and the algorithm is unable to converge outside of the ranges presented in both figures. This instability occurs with parameter changes of less than

5% from the values given in Table 12, indicating that only small changes in either parameter can cause convergence issues. While both parameters are sensitive to change, σ is more so as indicated by the sharp cutoff in Figure 21. An additional complexity arises with the appearance of a local minimum in the %AAD of PR with the S&K Kihara ε that may prevent convergence on a value of sigma that provides a global minimum in the %AAD. As a result of these conclusions, only ε has been fitted to experimental data and has shown significant improvement in prediction of the equilibrium pressure.

A fair comparison of the abilities of each EoS to predict the L_wHV phase equilibria conditions can only be done by excluding the components, Ar and O_2, which CSMGem cannot predict. Table 16 shows that PR is the most accurate while PC-SAFT and CSMGem perform comparably.

Table 16. Direct comparison of the prediction capabilities of PC-SAFT, PR, and CSMGem

Guest Species	PC-SAFT	PR	CSMGem
CH_4	11.04	5.87	1.94
C_2H_6	7.81	6.97	2.40
C_3H_8	3.25	0.42	10.85
iC_4H_{10}	0.91	0.72	4.06
CO_2	9.26	5.8	3.78
N_2	2.24	6.04	7.12
H_2S	2.72	2.34	5.67
Average	**5.32**	**4.02**	**5.12**

Based on these results, it is concluded that overall PR is better than PC-SAFT. However, PC-SAFT has the added advantage of being able to predict the phase equilibrium line closer to the upper quadruple point. This phenomenon that can be seen explicitly in Figure 22 and Figure 23. However, the consistency to which the algorithm is able to converge upon a solution near Q2 varies.

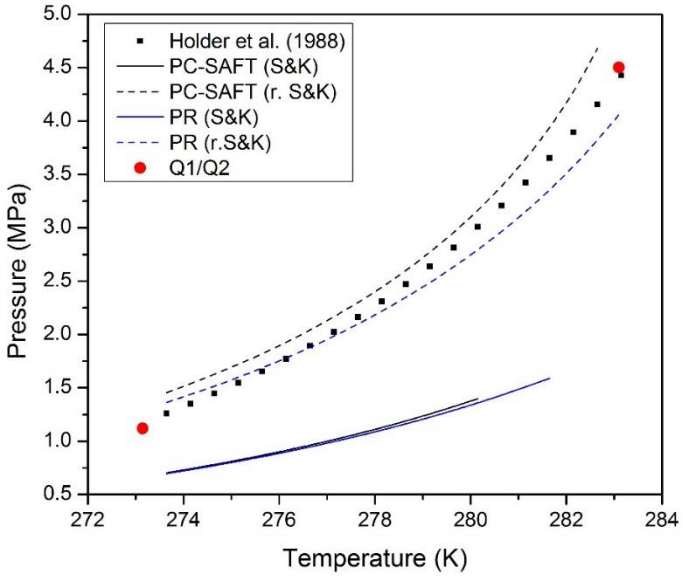

Figure 22. *L*$_w$*HV* phase equilibrium of CO_2, experimental data (points) and model predictions (lines)

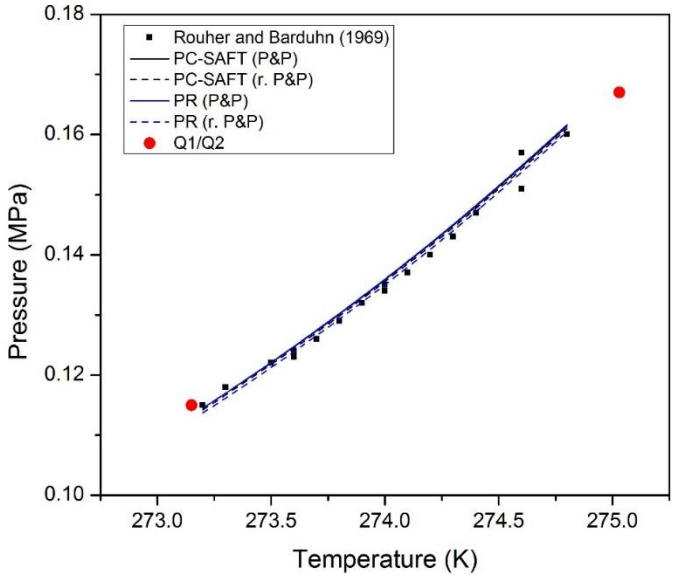

Figure 23. *L*$_w$*HV* phase equilibrium of *i*C_4H_{10}, experimental data (points) and model predictions (lines)

The accuracy of the EoS falls at higher pressures, a phenomenon that can be seen in Figure 24.

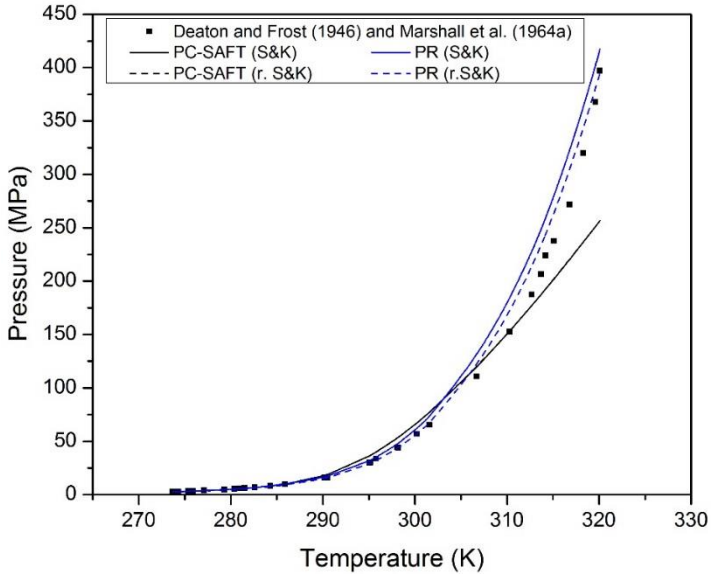

Figure 24. L_wHV phase equilibrium of CH_4, experimental data (points) and model predictions (lines)

In an effort to improve the results of the PC-SAFT EoS in the higher temperature region, an adjustment was made to temperature correction term in Equation [38]. This was based on the assumption that these deviations result from the reference potential of the empty hydrate lattice. Specifically, Equation [45] was used in place of Equation [40]

$$\Delta C_P' = 37.89 - 0.195\left(T - T_o\right) + 0.006\left(T - T_o\right)^{1.5} \qquad [45]$$

However, this change resulted in insignificant changes in the predictions at high temperatures and as such was not implemented in the algorithm.

Finally, Figure 25 shows that fitting only the Kihara ε not only improves the accuracy of the prediction but also the temperature range over which the algorithms are able to converge.

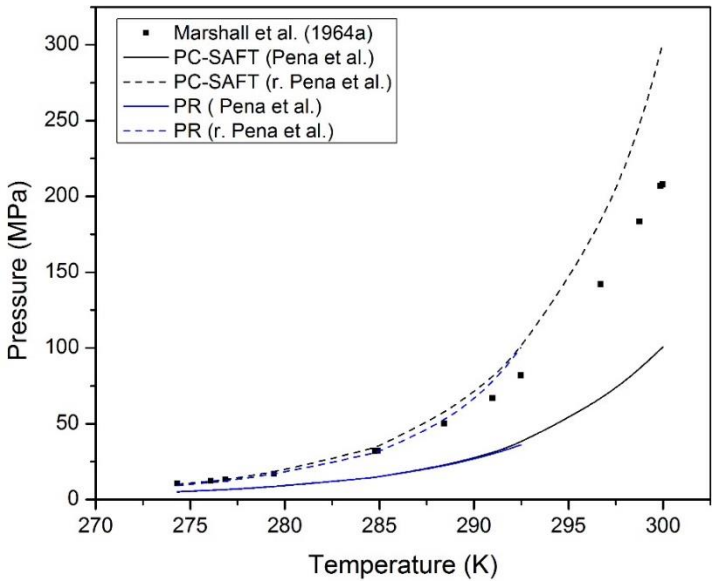

Figure 25. *L_wHV* phase equilibrium of Ar, experimental data (points) and model predictions (lines)

4.3.2 Mixtures of Hydrate Formers

Introducing a second hydrate former to the system, adds additional complications due to the expected change in hydrate structure with changes in the composition of the mixture. Here mixtures containing two, three and four components are studied. A review of available experimental data in the literature was conducted, and it became apparent that there remain many more mixtures and conditions that have yet to be studied. In an attempt to cover as wide a range of mixtures as possible, a scan of all the binary combinations of the pure hydrate formers has been done. The binary mixtures available in the literature are summarized in Table 17, and it can be seen that no experimental data sets exist for binary mixtures containing H_2S, Ar and O_2.

Table 17. Binary mixtures of guests considered for hydrate-fluid equilibrium calculations

Species	CH_4								
C_2H_6	x	C_2H_6							
C_3H_8	x	x	C_3H_8						
iC_4H_{10}	x			iC_4H_{10}					
CO_2	x	x	x	x	CO_2				
O_2						O_2			
N_2	x		x		x		N_2		
Ar								Ar	
H_2S	x								H_2S

A similar scan of combinations was done for both ternary and quaternary mixtures of hydrate formers, and it was found that for mixtures with more components there are even fewer data sets available. In general, the most popular mixtures are those containing CH_4 and CO_2.

Table 18. %AAD in EoS prediction of equilibrium pressure of binary gas mixture hydrates

Binary Guest Mixtures		PC-SAFT		PR		CSMGEM
		r. P&P	r. S&K	r. P&P	r. S&K	
CH_4	C_2H_6	20.37	(1)	17.02	(1)	2.54
	C_3H_8	4.54	9.69	3.46	13.40	4.61
	iC_4H_{10}	21.52	7.88	22.25	(3)	8.74
	CO_2	(2)	4.64	6.23	3.75	1.91
	N_2	9.80	11.10	8.76	8.61	20.42
CO_2	C_2H_6	(2)	(1)	11.97	(1)	50.09
	C_3H_8	(2)	20.17	18.86	11.97	17.44
	iC_4H_{10}	(2)	39.03	(2)	(3)	17.17
	N_2	(2)	10.14	14.67	14.37	14.20
C_3H_8	C_2H_6	11.73	(1)	8.28	(1)	12.83
	N_2	42.09	13.96	34.41	15.55	7.85
Average		18.34	14.58	14.59	11.28	14.35

(1) Lack of convergence due to C_2H_6 Kihara parameters (2) Lack of convergence due to CO_2 Kihara parameters (3) Lack of convergence due to iC_4H_{10} Kihara parameters

For the systems with mixtures of hydrate formers, only the fitted Kihara potential parameters are used to predict the equilibrium pressure due to their better accuracy in the prediction of the pure gas hydrate systems. However, as some combinations of parameters do not converge, a phenomenon noted in the previous section, it is not always possible to predict the equilibrium pressure of each of the previously defined cases. The convergence of the binary cases indicates that the sensitivity of the parameters fitted to the pure gas hydrate formers

remains in the analysis of the multicomponent hydrate formers. For this reason, where only one set of parameters for a component was available for the ternary and quaternary cases, the available parameter set was used for both r. P&P and r. S&K cases.

Based on the deviations between EoS predictions and experimental data tabulated in both Table 18 and Table 19, it can be concluded that the r. S&K parameters allow for more accurate predictions in the multicomponent mixtures. r. S&K parameters produce results 4-6% more accurate than those predicted using the r. P&P. This improvement in equilibrium pressure prediction by both EoS is consistent with the pure hydrate system calculations although with larger error margins. In addition, prediction of the L_wHV equilibrium of mixtures containing alkanes is less accurate.

Table 19. %AAD in EoS prediction of equilibrium pressure of ternary and quaternary gas mixture hydrates

Guest Mixtures	PC-SAFT		PR	
	r. P&P	r. S&K	r. P&P	r. S&K
Ternary mixture of hydrate former				
CH_4-CO_2-N_2	0.83	1.52	13.20	3.82
CH_4-CO_2-H_2S	27.96	26.03	15.30	14.85
CH_4-C_2H_6-C_3H_8	42.96	13.62	26.16	6.46
CH_4-C_2H_6-N_2	20.34	21.85	20.77	15.39
CH_4-C_3H_8-iC_4H_{10}	8.61	7.21	8.08	7.97
Average	20.14	14.05	16.70	9.70
Quaternary mixture of hydrate former				
CH_4-CO_2-N_2-C_2H_6	17.38	18.48	8.28	11.44
CH_4-CO_2-N_2-C_3H_8	22.17	0.45	27.02	4.45
CO_2-N_2-O_2-Ar	44.95	52.76	50.03	56.30
Average	28.17	23.90	28.44	24.06

More information can be obtained from the qualitative analysis of the hydrate fluid equilibrium predictions. Based on the representation of the results in Figure 26, the effect of hydrate structure on equilibrium pressure can be seen.

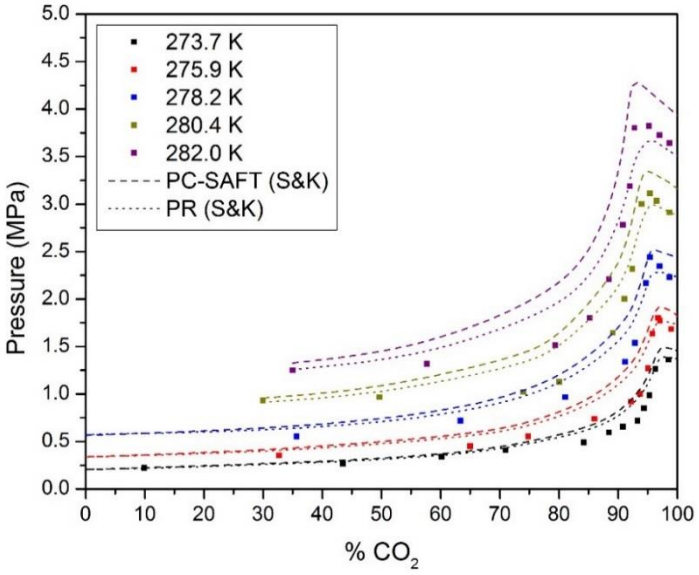

Figure 26. Prediction of L_wHV equilibrium for a binary mixture of CO_2 with C_3H_8 over a range of compositions, experimental data (points) and model predictions (lines)

Pure CO_2 hydrates exist as sI structured hydrates while C_3H_8 exists in sII hydrate structures. Thus, at some intermediate concentration, there is a transition between structures. For this specific mixture, this transition appears in the form of the sudden pressure drop that occurs at a mole fraction of CO_2 slightly above 0.95. This conclusion can be confirmed by studying those mixtures where both pure hydrate form in the sI structure, such as the binary CO_2 with N_2 where the hydrate equilibrium do not exhibit this peak in pressure, indicating that the phenomenon can be attributed to the change in structure. Both EoS have the ability to predict this change in equilibrium pressure that results from the changing structure at the correct concentration.

It is worth noting that the quadruple point of pure C_3H_8 occurs at 0.56 MPa. Therefore, in Figure 26, for the 280.4 K and the 282.0 K isotherms, at some concentration of CO_2 less than 30%, the three-phase equilibrium shifts to liquid CO_2, Hydrate and liquid water equilibrium and the methodology used to calculated that equilibrium differs from that

implemented in this work. In addition to the two-phase flash calculation of the liquid-liquid equilibrium (LLE) to find the mole fraction of CO_2 in the liquid water phase, the implementation of a non-unity activity coefficient to further account for the impurities in the liquid water phase (in Equation [38]) should be considered to improve the calculations further.

The error in EoS prediction tends to increase at high temperatures, which is consistent with the trends seen in the pure hydrate systems and can be seen explicitly in Figure 27.

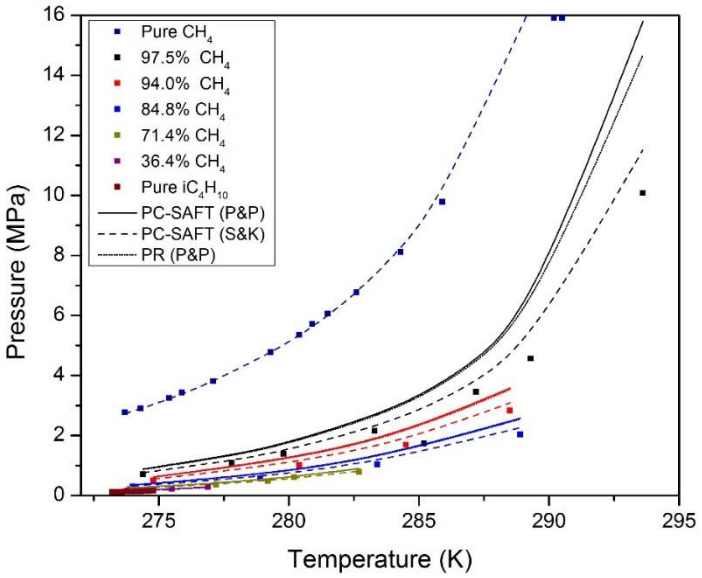

Figure 27. Prediction of *LwHV* equilibrium for a binary mixture of CO_2 with *i*C_4H_{10} over a range of temperatures, experimental data (points) and model predictions (lines)

Generally, predictions become less accurate with the addition of impurities to the mixture. This feature of the calculation is exhibited clearly in almost all binary, ternary and quaternary hydrate equilibrium mixtures. The apparent exception being in Figure 59 with the mixture of CO_2 and N_2 where higher deviations occur at relatively small concentrations of CO_2.

Alkanes tend to be hydrate promoters, where small quantities of the alkane can vastly reduce the equilibrium pressure. As seen in Figure 27, the addition of less than 3% of isobutane

to methane hydrate reduces the equilibrium pressure by approximately half of its original value. Thus promoting hydrate growth over a much wider range of conditions compared to the pure hydrate former. In addition, both PC-SAFT and PR tend to over-predict the equilibrium pressure, especially at high temperatures, indicating that they do not fully capture the effect of the alkanes in the mixture. This analysis leads to the conclusion that the addition of alkanes to the hydrate former mixture raises the %AAD. The same phenomenon is exhibited by ternary mixtures of hydrate formers such as CH_4-C_2H_6-C_3H_8 in Figure 28.

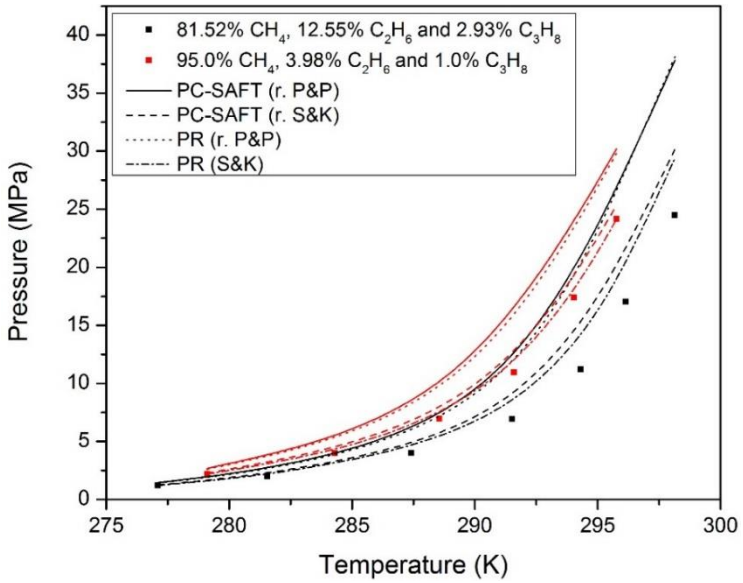

Figure 28. *HVL$_w$* equilibrium for the ternary system of CH_4, C_2H_6 and C_3H_8, experimental data (points) and model predictions (lines)

5. CONCLUSIONS

In an effort to better understand the range of conditions, number of phases and the components that macroscopic theories are best suited for, this thesis has studied a variety of complex systems. A comprehensive review of the literature revealed two EoS to be prime candidates for a detailed study of several multicomponent, multiphase systems. In addition to being known to perform well over a wide range of conditions, these EoS are popularly used in both research and industrial pursuits. The two EoS used are PC-SAFT, an equation derived based on statistical mechanical theories and PR a cubic equation commonly used in industry. The prediction capabilities of these two EoS were compared over a wide range of conditions, and various conclusions were drawn.

Both EoS were used saturation properties of pure components and derivative properties from the liquid to the supercritical range. Overall, PC-SAFT outperformed PR in all cases. The isochoric and isobaric heat capacities were studied in a range of conditions that covered the critical point of each component under review. Both EoS were able to predict the isobaric heat capacity relatively well. However, both were unable to adequately predict the trends exhibited by the isochoric heat capacity near critical conditions. In addition, PC-SAFT and PR can predict the speed of sound and isothermal compressibility of the pure components fairly accurately.

The VLE, speed of sound and isothermal compressibility of several binary and a ternary mixture were studied. The prediction capabilities of both EoS were relatively poor. Thus, the binary interaction parameter was introduced and fitted to binary mixture VLE. This procedure

drastically improved the quality of the bubble pressure calculations. However, only had a moderate influence on the derivative properties.

The introduction of a hydrate phase further complicates the calculations. Due to the inability of these particular EoS to predict properties of hydrates, they were used in conjunction with the van der Waals-Platteeuw model. It was concluded that the accuracy of the predictions of the three-phase equilibrium is highly dependent on the reliability of the Kihara parameters, one of which was fitted to equilibrium data and resulted in a significant improvement in the accuracy of both EoS predictions. An analysis of the results lead to various conclusions about the performance ability of both EoS. Mainly, that PR systematically outperformed PC-SAFT for L_wHV equilibrium calculations. The set of fitted Kihara parameters were used to predict the same three-phase equilibrium of several binary, ternary and quaternary mixtures of hydrate forming agents. Again the performance of both equations remain consistent; on average, PR performed better than PC-SAFT.

Several suggestions for further improvements of the calculations completed in this work can be made. The first relies on further optimization of the parameters for the pure methane hydrate calculations. Currently, the equilibrium pressure prediction for methane is almost twice the average of the remaining species. This above average deviation is due to the high deviation of prediction in the high-temperature range. In addition, improvements in predictions of both EoS could be made with the implementation of the binary interaction parameter to improve prediction of the solubility in the estimation of the chemical potential of the liquid water phase.

REFERENCES

1. Cubasch U, Wuebbles D, Chen D, Facchini MC, Frame D, Mahowald N, Winther J-G. Introduction. In: Ding Y, Mearns L, Wadhams P, eds. *Climate Change 2013: The Physical Basis. Contribution of Working Group I to the Fifth Assessment Report of the Intergovernmental Panel on Climate Change*. Cambridge University Press; 2013:119-158.

2. Ciais P, Sabine C, Bala G, Bopp L, Brovkin V, Canadell J, Chhabra A, DeFries R, Galloway J, Heimann M, Jones C, Le Quere C, Myneni R, Piao S, Thomton P. Carbon and Other Biogeochemical Cycles. In: Heinze C, Tans P, Vesala T, eds. *Climate Change 2013: The Physical Basis. Contribution of Working Group I to the Fifth Assessment Report of the Intergovernmental Panel on Climate Change*. Cambridge University Press; 2013:465-570.

3. Freund P, Gale J, Thambinmuthu K, Soltanieh M, Abanades JC, Doctor R, Palmer A, Benson S, Cook P, Caldeira K, Akai M, Mazzotti M, Herzog H, Smekens K, Osman-Elasha B, Pipatti R. *IPCC Specail Report on Carbon Dioxide Capture and Storage*. (Metz B, Davidson O, De Coninck H, Loos M, Meyer L, eds.). Intergovernmental Panel on Climate Change; 2005:1-443.

4. Klauda JB, Sandler SI. Global Distribution of Methane Hydrate in Ocean Sediment. *Energy & Fuels* 2005;19(2):459-470.

5. Mondal MK, Balsora HK, Varshney P. Progress and trends in CO_2 capture/separation technologies: A review. *Energy* 2012;46(1):431-441.

6. Markewitz P, Kuckshinrichs W, Leitner W, Linssen J, Zapp P, Bongartz R, Schreiber A, Müller TE. Worldwide innovations in the development of carbon capture technologies and the utilization of CO_2. *Energy Environ. Sci.* 2012;5:7281.

7. Mazzoccoli M, Bosio B, Arato E. Pressure–density–temperature measurements of binary mixtures rich in CO_2 for pipeline transportation in the CCS process. *J. Chem. Eng. Data* 2012;57(10):2774-2783.

8. Al-Siyabi I. Effect of impurities on CO2 stream properties. *PhD Thesis. Heriot-Watt Univ.* 2013:1-182.

9. Rubin ES, Mantripragada H, Marks A, Versteeg P, Kitchin J. The outlook for improved carbon capture technology. *Prog. Energy Combust. Sci.* 2012;38:630-671.

10. Li H, Jakobsen JP, Wilhelmsen Ø, Yan J. PVTxy properties of CO_2 mixtures relevant for CO_2 capture, transport and storage: Review of available experimental data and theoretical models. *Appl. Energy* 2011;88(11):3567-3579.

11. Li H. Thermodynamic properties of CO_2 mixtures and their applications in advanced power cycles with CO_2 capture processes. *PhD Thesis. R. Insititute Techonology* 2008:1-63.

12. Oosterkamp A, Ramsen J. State-of-the-art overview of CO_2 pipeline transport with relevance to offshore pipelines. *Polytech Rep.* 2008;POL-O-2007:1-87.

13. Lemmon EW, McLinden MO, Friend DG. Thermophysical Properties of Fluid Systems. In: Linstrom PJ, Mallard WG, eds. *NIST Chemistry WebBook, NIST Standard Refernce Database Number 69*. Available at: http://webbook.nist.gov.

14. Coquelet C, Valtz A, Dieu F, Richon D, Arpentinier P, Lockwood F. Isothermal P,x,y data for the Argon+ Carbon Dioxide system at six temperatures from 233.32 to 299.21K and pressures up to 14MPa. *Fluid Phase Equilib.* 2008;273(1-2):38-43.

15. Sarashina E, Arai Y, Sasto S. the P-V-T-X Relation for the Carbon Dioxide-Argon System. *J. Chem. Eng. Japan* 1971;4(4):379-381.

16. Blümcke A. Ueber die Bestimmung der specifischen Gewichte und Dampfspannungen einiger Gemische von schwefliger Säure und Kohlensäure. *Ann. Phys.* 1887;270(5):10-21.

17. Lachet V, de Bruin T, Ungerer P, Coquelet C, Valtz A, Hasanov V, Lockwood F, Richon D. Thermodynamic behavior of the CO_2+SO_2 mixture: Experimental and Monte Carlo simulation studies. *Energy Procedia* 2009;1(1):1641-1647.

18. Arai Y, Kaminshi G-I, Saito S. The Experimental Determination of the PVTX Relations for the Carbon Dioxide-Nitrogen and the Carbon Dioxide-Methane Systems. *J. Chem. Eng. Japan* 1971;4(2):113-122.

19. Davalos J, Anderson WR, Phelps RE, Kidnay AJ. Liquid-Vapor Equilibria at 250.00K for Systems Containing Methane, Ethane, and Carbon Dioxide. *J. Chem. Eng. Data* 1976;21(1):81-84.

20. Donnelly HG, Katz DL. Phase Equilibria in the Carbon Dioxide-Methane System. *Ind. Eng. Chem.* 1954;46(3):511-517.

21. Esper GJ, Bailey DM, Holste JC, Hall KR. Volumetric Behavior of Near-Equimolar Mixtures for CO_2+CH_4 and CO_2+N_2. *Fluid Phase Equilib.* 1989;49:35-47.

22. Hwang C, Iglesias-silva GA, Holste JC, Hall KR, Gammon BE, Marsh KN. Densities of Carbon Dioxide + Methane Mixtures from 225 K to 350 K at Pressures up to 35 MPa. *J. Chem. Eng. Data* 1997;42:897-899.

23. Haney RED, Bliss H. Compressibilities of Nitrogen–Carbon Dioxide Mixtures. *Ind. Eng. Chem.* 1944;36(11):985-989.

24. Hacura A, Yoon J-H, Baglin FG. Density Values of Carbon Dioxide and Nitrugen Mixtures from 500 to 2500 bar at 323 and 348 K. *J. Chem. Eng. Data* 1988;33:152-154.

25. Ely J., Haynes W., Bain B. Isochoric (p,V,T) measurements on from 250 to 330 K at pressures to 35 MPa. *J. Chem. Thermodyn.* 1989;21:879-894.

26. Mallu B., Natarajan G, Viswanath D. Compression factors and second virial coefficients of CO_2, CO and $CO+CO_2$. *J. Chem. Therm* 1987;19:549-554.

27. Christiansen LJ, Fredenslund A, Gardner N. Gas-Liquid Equilibria of the CO_2-CO and CO_2-CH_4-CO Systems. *Adv. Cyrogenic Eng.* 1995;19:309-319.

28. Fredenslund A, Sather GA. Gas-liquid equilibrium of the Oxygen-Carbon Dioxide system. *J. Chem. Eng. Data* 1970;15(1):17-22.

29. Fredenslund A, Mollerup J, Persson O. Gas-liquid Equilibrium of Oxygen-Carbon Dioxide System. *J. Chem. Eng. Data* 1972;17(4):440-443.

30. Creton B, de Bruin T, Le Roux D, Duchet-Suchaux P, Veronique L. Impact of associated gases on equilibrium and transport properties of a CO_2 stream : molecular simulation and experimental studies . *Int. J. Thermophys.* 2014;35:256-276.

31. Muirbrook NK, Prausnitz JM. Multicomponent Vapor-Liquid Equilibria at High Pressures: Part I. Experimental Study of Nitrogen-Oxygen-Carbon Dioxide System at 0C. *AIChE J.* 1965;11(6):1092-1096.

32. Zenner G, Dana L. Liquid-Vapor equilibrium compositions of carbondioxide-oxygen-nitrogen mixtures. In: *Chemical Engineering Progress Symposium*.Vol 59.; 1963:44.

33. Trappehl G, Knapp H. Vapour-liquid equilibria in the ternary mixture N_2-CH_4-CO_2 and the quaternary mixture N_2-CH_4-C_2H_6-C_3H_8. *Cryogenics (Guildf).* 1989;29:42-50.

34. Al-Sahhaf T. Vapor-liquid equilibria for the ternary system $N_2+CO_2+CH_4$ at 230 and 250K. *Fluid Phase Equilib.* 1990;55(1-2):159-172.

35. Seitz JC, Blencoe JG, Bodnar RJ. Volumetric Properties for $CO_2+CH_4+N_2$ at the Pressures (19.94, 39.94, 59.93, and 99.93) MPa and Temperatures (323.15, 373.15, 473.15, and 573.15) K. *J. Chem. Thermodyn.* 1996;28:539-550.

36. Peng DY, Robinson DB. A new two-constant equation of state. *Ind. Eng. Chem. Fundam.* 1976;15(1):59-64.

37. Soave G. Equilibrium constants from a modified Redlich-Kwong equation of state. *Chem. Eng. Sci.* 1972;27(6):1197-1203.

38. Li H, Yan J. Impacts of equations of state (EOS) and impurities on the volume calculation of CO_2 mixtures in the applications of CO_2 capture and storage (CCS) processes. *Appl. Energy* 2009;86(12):2760-2770.

39. Thiery R, Vidal J, Dubessy J, Cedex RM. Phase equilibria modelling applied to fluid inclusions: Liquid-vapour equilibria and calculation of the molar volume in the CO_2-CH_4-N_2 system. *Geochim. Cosmochim. Acta* 1994;58(3):1073-1082.

40. Vrabec J, Kedia GK, Buchhauser U, Meyer-Pittroff R, Hasse H. Thermodynamic models for vapor–liquid equilibria of Nitrogen+Oxygen+Carbon Dioxide at low temperatures. *Cryogenics (Guildf).* 2009;49(2):72-79.

41. Xu N, Dong J, Wang Y, Shi J. High Pressure Vapor Liquid Equilibria at 293 K for Systems containing Nitrogen, Methane and Carbon Dioxide. *Fluid Phase Equilib.* 1992;81:176-186.

42. Melhem G, Saini R, Goodwin BM. A Modified Peng-Robinson Equation of State. *Fluid Phase Equilib.* 1989;47:189-237.

43. Wilhelmsen Ø, Skaugen G, Jørstad O, Li H. Evaluation of SPUNG and other Equations of State for use in Carbon Capture and Storage modelling. *Energy Procedia* 2012;23:236-245.

44. Austegard A, Solbraa E, De Koeijer G, Mølnvik MJ. Thermodynamic Models for Calculating Mutual Solubilities in H_2O–CO_2–CH_4 Mixtures. *Chem. Eng. Res. Des.* 2006;84(9):781-794.

45. Belkadi A, Llovell F, Gerbaud V, Vega L. Modeling the vapor–liquid equilibrium and association of Nitrogen Dioxide/Dinitrogen Tetroxide and its mixtures with Carbon Dioxide. *Fluid Phase Equilib.* 2008;266(1-2):154-163.

46. García-Sánchez F, Eliosa-Jiménez G, Silva-Oliver G, Vázquez-Román R. Vapor–liquid equilibria of nitrogen–hydrocarbon systems using the PC-SAFT equation of state. *Fluid Phase Equilib.* 2004;217(2):241-253.

47. Llovell F, Vega LF. Prediction of thermodynamic derivative properties of pure fluids through the soft-SAFT equation of state. *J. Phys. Chem. B* 2006;110(23):11427-11437.

48. Adepoju O. Coefficient of Isothermal Oil Compressibility for Reservoir fluids by cubic Equations of State. *PhD Thesis. Texas Tech Univ.* 2006.

49. Kachanov Y, Kanishchev B, Pitaevskaya L. Velocity of Sound in Argon and in Helium-Argon and Nitrogen-Carbon Dioxide Gas Mixtures at High Pressures. *J. Eng. Phys.* 1983;44(1):1-4.

50. Løvseth SW, Skaugen G, Stang HGJ, Jakobsen JP, Wilhelmsen Ø, Span R, Wegge R. CO_2Mix Project: Experimental Determination of Thermo-physical Properties of CO_2-rich Mixtures. *Energy Procedia* 2013;37:7841-7849.

51. Diamantonis N, Boulougouris G, Tsangaris DM, Economou IG. A report that identifies knowledge gaps for thermodynamic properties of CO_2 mixtures with impurities. *CO_2 Quest* 2013:1-21.

52. Diamantonis NI, Boulougouris GC, Tsangaris DM, El Kadi MJ, Saadawi H, Negahban S, Economou IG. Thermodynamic and transport property models for carbon capture and sequestration (CCS) processes with emphasis on CO_2 transport. *Chem. Eng. Res. Des.* 2013;91(10):1793-1806.

53. Liang X, Maribo-Mogensen B, Thomsen K, Yan W, Kontogeorgis GM. Approach to Improve Speed of Sound Calculation within PC-SAFT Framework. *Ind. Eng. Chem. Res.* 2012;51(45):14903-14914.

54. Lafitte T, Bessieres D, Piñeiro MM, Daridon JL. Simultaneous estimation of phase behavior and second-derivative properties using the statistical associating fluid theory with variable range approach. *J. Chem. Phys.* 2006;124(2):024509.

55. Llovell F, Peters CJ, Vega LF. Second-order thermodynamic derivative properties of selected mixtures by the soft-SAFT equation of state. *Fluid Phase Equilib.* 2006;248(2):115-122.

56. Saito T, Kajishima T, Nagaosa R. CO_2 sequestration at sea by gas-lift system of shallow injection and deep releasing. *Environ. Sci. Technol.* 2000;34(19):4140-4145.

57. Yang M, Song Y, Jiang L, Zhao Y, Ruan X, Zhang Y, Wang S. Hydrate-based technology for CO_2 capture from fossil fuel power plants. *Appl. Energy* 2014;116:26-40.

58. Sloan E. Fundamental principles and applications of natural gas hydrates. *Nature* 2003;426(November):353-359.

59. Sloan ED, Koh CA. *Clathrate Hydrates of Natural Gases*. 3rd ed. (Heinemann H, ed.). Taylor & Francis Group, LLC; 2008.

60. Holder GD, Zetts SP, Pradhan N. Phase behavior in systems containing clathrate hydrates: a review. *Rev. Chem. Eng.* 1988;5:1-70.

61. Parrish W, Prausnitz J. Dissociation pressures of gas hydrates formed by gas mixtures. *Ind. Eng. Chem. Process Des. Dev.* 1972;11(1):26-35.

62. Kroenlein K, Muzny C., Kazakov A, Diky VV, Chirico R., Sloan E., Frenkel M. Database of Thermodynamic and Crystallographic Properties of Gas Hydrates. In: *NIST Chemistry WebBook, NIST Standard Reference Database #156*.; 2009. Available at: http://webbook.nist.gov.

63. Karakatsani EK, Kontogeorgis GM. Thermodynamic Modeling of Natural Gas Systems Containing Water. *Ind. Eng. Chem. Res.* 2013;52(9):3499-3513.

64. Diamantonis NI, Tsimpanogiannis IN, Economou IG, Stubos AK. Hydrate Equilibrium Calculations of Pure Gas Hydrates Using A SAFT-Type EoS. In: *Proceedings of the 8th International Conference on Gas Hydrates*.; 2014.

65. English NJ, Macelroy JMD. Perspectives on molecular simulation of clathrate hydrates : Progress, prospects and challenges. *Chem. Eng. Sci.* 2015;121:133-156.

66. Sparks KA, Tester JW, Cao Z, Trout BL. Configurational Properties of Water Clathrates: Monte Carlo and Multidimensional Integration versus the Lennard-Jones and Devonshire Approximation. *J. Phys. Chem. B* 1999;103(3):6300-6308.

67. Jatkar K, Lee JW, Lee S. Determination of Reference Chemical Potential Using Molecular Dynamics Simulations. *J. Thermodyn.* 2010;2010:1-5.

68. Walsh MR, Beckham GT, Koh CA, Sloan ED, Wu DT, Sum AK. Methane hydrate nucleation rates from molecular dynamics simulations: Effects of aqueous methane concentration, interfacial curvature, and system size. *J. Phys. Chem. C* 2011;115:21241-21248.

69. English NJ, Clarke ET. Molecular dynamics study of CO_2 hydrate dissociation: Fluctuation-dissipation and non-equilibrium analysis. *J. Chem. Phys.* 2013;139:097401.

70. Conde MM, Vega C. Determining the three-phase coexistence line in methane hydrates using computer simulations. *J. Chem. Phys.* 2010;133:064507.

71. Michalis VK, Costandy J, Tsimpanogiannis IN, Stubos AK, Economou IG. Prediction of the phase equilibria of methane hydrates using the direct phase coexistence methodology. *J. Chem. Phys.* 2015;142:044501.

72. Miguez JM, Miqueu C, Mendiboure B, Torré J, Blas FJ, Aplicada DDF, Huelva U De, Pineiro MM, Conde MM, Vega C. Molecular Dynamics and Thermodynamical Modelling Using SAFT-VR To Predict Hydrate Phase Equilibria: Application To CO_2 Hydrates. In: *Proceedings of the 8th International Conference on Gas Hydrates*.; 2014.

73. Tung YT, Chen LJ, Chen YP, Lin ST. The Growth of Structure I Methane Hydrate from Molecular Dynamics Simulation. *J. Phys. Chem. B* 2010;114:10804-10813.

74. Tung YT, Chen LJ, Chen YP, Lin ST. The Growth of Structure I Carbon Dioxide Hydrate from Molecular Dynamics Simulations. *J. Phys. Chem. C* 2011;115:7504-7515.

75. Platteeuw JC, van der Waals JH. Thermodynamic properties of gas hydrates. *Mol. Phys.* 1957;1(1):91-96.

76. Cao Z. Modeling of gas hydrates from first principles. *PhD Thesis. Massachusetts Inst. Technol.* 2002.

77. Klauda JB, Sandler SI. A Fugacity Model for Gas Hydrate Phase Equilibria. *Ind. Eng. Chem. Res.* 2000;39:3377-3386.

78. Chen G, Guo T. Thermodynamic modeling of hydrate formation based on new concepts. *Fluid Phase Equilib.* 1996;122:43-65.

79. Chen G, Guo T. A new approach to gas hydrate modelling. *Chem. Eng. J.* 1998;71:145-151.

80. Klauda JB, Sandler SI. Phase behavior of clathrate hydrates: A model for single and multiple gas component hydrates. *Chem. Eng. Sci.* 2003;58:27-41.

81. Sun CY, Chen GJ. Modelling the hydrate formation condition for sour gas and mixtures. *Chem. Eng. Sci.* 2005;60:4879-4885.

82. Delavar H, Haghtalab A. Prediction of hydrate formation conditions using GE-EOS and UNIQUAC models for pure and mixed-gas systems. *Fluid Phase Equilib.* 2014;369:1-12.

83. Li XS, Wu HJ, Li YG, Feng ZP, Tang LG, Fan SS. Hydrate dissociation conditions for gas mixtures containing carbon dioxide, hydrogen, hydrogen sulfide, nitrogen, and hydrocarbons using SAFT. *J. Chem. Thermodyn.* 2007;39:417-425.

84. Prausnitz JM, Lichtenthaler RN, de Azevedo EG. *Molecular Thermodynamics of Fluid-Phase Equilibria*. 3rd ed.; 1999.

85. Chapman W, Gubbins K, Jackson G, Radosz M. New Reference Equation of State for Associating Liquids. *Ind. Eng. Chem. Res.* 1990;29(8):1709-1721.

86. Chapman WG, Gubbins K., Jackson G, Radosz M. SAFT: equation-of-state solution model for associating fluids. *Fluid Phase Equilib.* 1989;52:31-38.

87. Wertheim MS. Fluids with highly directional attractive forces. I. Statistical Thermodynamics. *J. Stat. Phys.* 1984;35(1):19-34.

88. Wertheim MS. Fluids with highly directional attractive forces. II. Thermodynamic perturbation theory and integral equations. *J. Stat. Phys.* 1984;35:35-47.

89. Wertheim MS. Fluids with Highly Directional Attractive Forces . III. Multiple Attraction Sites. *J. Stat. Phys.* 1986;42:459-476.

90. Wertheim MS. Fluids with highly directional attractive forces. IV. Equilibrium Polymerization. *J. Stat. Phys.* 1986;42:477-492.

91. Chen S, Kreglewski A. Applications of the Augmented van der Waals Theory of Fluids. I. Pure Fluids. *Berichte der Bunsen-Gesekkschaft* 1977;81(10):1048-1052.

92. Gil-Villegas A, Galindo A, Whitehead PJ, Mills SJ, Jackson G, Burgess AN. Statistical associating fluid theory for chain molecules with attractive potentials of variable range. *J. Chem. Phys.* 1997;106:4168.

93. Galindo A, Davies L, Gil-Villegas A, Jackson G. The Thermodynamics of Mixtures and the Corresponding Mixing Rules in the SAFT-VR Approach for Potentials of Variable Range. *Mol. Phys.* 1998;106:241-252.

94. Blas FJ, Vega LF. Thermodynamic Behaviour of Homonuclear and heteronuclear Lennard-Jones Chains with Association Sites from Simulation and Theory. *Mol. Phys.* 1997;92:135-150.

95. Blas FJ, Vega LF. Prediction of Binary and Ternary Diagrams Using the Statistical Associating Fluid Theory (SAFT) Equation of State. *Ind. Eng. Chem. Res.* 1998;37:660-674.

96. Müller E, Gubbins K. Molecular-based equations of state for associating fluids: A review of SAFT and related approaches. *Ind. Eng. Chem. Res.* 2001;40:2193-2211.

97. Economou I. Statistical associating fluid theory: A successful model for the calculation of thermodynamic and phase equilibrium properties of complex fluid mixtures. *Ind. Eng. Chem. Res.* 2002;41:953-962.

98. Mansoori GA, Carnahan NF, Starling KE, Leland Jr. TW. Equilibrium Thermodynamic Properties of the Mixture of Hard Spheres. *J. Chem. Phys.* 1971;54(4):1523.

99. Gross J, Sadowski G. Perturbed-chain SAFT: An equation of state based on a perturbation theory for chain molecules. *Ind. Eng. Chem. Res.* 2001;40(4):1244-1260.

100. Gross J, Sadowski G. Application of the perturbed-chain SAFT equation of state to associating systems. *Ind. Eng. Chem. Res.* 2002;41(22):5510-5515.

101. Diamantonis NI, Economou IG. Evaluation of statistical associating fluid theory (SAFT) and perturbed chain-SAFT equations of state for the calculation of

thermodynamic derivative properties of fluids related to carbon capture and sequestration. *Energy & Fuels* 2011;25(7):3334-3343.

102. Thorade M, Saadat A. Partial derivatives of thermodynamic state properties for dynamic simulation. *Environ. Earth Sci.* 2013;70(8):3497-3503.

103. Wilson G. A Modified Redlich-Kwong Equation of State; Application to General Physical Data Calculation. In: *1969 AIChE 65th National Meeting*. Cleveland, OH; 1969.

104. Diamantonis N, Boulougouris GC, Mansoor E, Tsangaris D, Economou IG. Evaluation of cubic, SAFT, and PC-SAFT equations of state for the vapor-liquid equilibrium modeling of CO_2 mixtures with other gases. *Ind. Eng. Chem. Res.* 2013;52:3933-3942.

105. Diamantonis NI. Mathematical modeling of thermophysical properties and phase equilibria of pure carbon dioxide and multicomponent mixtures. *PhD Thesis. Natl. Tech. Univ. Athens.* 2013.

106. Tihic A. Group Contribution sPC-SAFT Equation of State. *PhD Thesis. Tech. Univ. Denmark.* 2008.

107. Christiansen LJ, Fredenslund A, Gardner N. Gas liquid equilibria of the CO_2-CO and CO_2-CH_4-CO systems. *Adv. Cyrogenic Eng.* 1974;19:309-319.

108. Christiansen LJ. Vapour-liquid equilibrium of the CH_4-Ar, CH_4-CO, and Ar-CO systems at elevated pressures. *Cryogenics (Guildf).* 1973;13(7):405-413.

109. Parrish W, Prausnitz JM. Correction- Dissociation Pressure of Gas Hydrates Formed by Gas Mixtures. *Ind. Eng. Chem. Process Des. Dev.* 1972;11(3):462.

110. Diaz Peña M. Combination rules for intermolecular potential parameters. I. Rules based on approximations for the long-range dispersion energy. *J. Chem. Phys.* 1982;76(1):325.

111. Deaton W, Frost E. *Gas Hydrates and Their Relation to the Operation of Natural-Gas Pipe Lines.* U.S. Bureau of Mines Monograph 8; 1946:101.

112. Marshall DR, Saito S, Kobayashi R. High Pressures : Part I. Methane-Water, Argon-Water, and Nitrogen-Water Systems. *AIChE J.* 1964;10(2):202-205.

113. Rouher OS, Barduhn AJ. Hydrates of iso- and normal butane and their mixtures. *Desalination* 1969;6:57-73.

114. Van Cleef A, Diepen G. Gas Hydrates of Nitrogen and Oxygen. II. *Recl. des Trav. Chim. des Pays-Bas* 1965;84(8):1085-1093.

115. Ballard AL, Sloan ED. The next generation of hydrate prediction: An overview. *J. Supramol. Chem.* 2002;2(4):385-392.

116. Gross J, Sadowski G. Application of perturbation theory to a hard-chain reference fluid: an equation of state for square-well chains. *Fluid Phase Equilib.* 2000;168:183-199.

APPENDIX

7.1 Appendix I: Mathematical Formulation of PC-SAFT

The following appendix specifics the mathematical description of each Helmholtz free energy term in the PC-SAFT EoS.[99,100,116]

$$\frac{a^{res}}{RT} = \frac{a}{RT} - \frac{a^{ideal}}{RT} = \frac{a^{hc}}{RT} + \frac{a^{disp}}{RT} + \frac{a^{assoc}}{RT} \qquad [46]$$

The ideal Helmholtz free energy:

$$\frac{a^{ideal}}{RT} = \ln \rho - 1 \qquad [47]$$

7.1.1 Hard-Chain Reference Fluid

This section explains the terms needed to calculate the Helmholtz free energy of hard-chain reference fluid, a^{hc}:

$$\frac{a^{hc}}{RT} = \bar{m}\frac{a^{hs}}{RT} - \sum_i x_i \left(m_i - 1\right) \ln g_{ii}^{hs}\left(d_{ii}\right) \qquad [48]$$

The only input parameters that are directly required by Equation [48] are m, the number of segments in the non-spherical molecule, and, x_i, the mole fraction of component i. $\bar{m}$ is defined as the average number of segments:

$$\bar{m} = \sum_i x_i m_i \qquad [49]$$

This equations also requires the Helmholtz energy of hard-spheres that constitute the chain, a^{hs}:

$$\frac{a^{hs}}{RT} = \frac{1}{\zeta_0}\left(\frac{3\zeta_1\zeta_2}{(1-\zeta_3)} + \frac{\zeta_2^3}{\zeta_3(1-\zeta_3)^2} + \left(\frac{\zeta_2^3}{\zeta_3^2} - \zeta_0\right)\ln(1-\zeta_3)\right) \quad [50]$$

The final parameter in Equation [48] is the hard-sphere radial distribution function, g_{ij}^{hs}:

$$g_{ij}^{hs} = \frac{1}{(1-\zeta_3)} + \left(\frac{d_i d_j}{d_i + d_j}\right)\frac{3\zeta_2}{(1-\zeta_3)^2} + \left(\frac{d_i d_j}{d_i + d_j}\right)^2 \frac{3\zeta_2^2}{(1-\zeta_3)^3} \quad [51]$$

Both the radial distribution function and the Helmholtz free energy of the hard sphere reference fluid require the partial volume fraction:

$$\zeta_n = \frac{\rho\pi}{6}\sum_i x_i m_i d_i^n \qquad n \in \{0,1,2,3\} \quad [52]$$

The number density of the fluid is defined as the partial volume fraction at $n = 3$. The number density can then be converted to the density of the fluid.

$$\eta = \zeta_3 \quad [53]$$

In Equation [52], d is the segment diameter that is a function of temperature and two required inputs; the chain segment diameter, σ_i, and the energy of dispersion, ε_i:

$$d_i = \sigma_i\left[1 - 0.12\exp\left(-3\frac{\varepsilon_i}{kT}\right)\right] \quad [54]$$

7.1.2 Dispersion Interactions

The dispersion contribution to the residual Helmholtz free energy is based on the second order perturbation theory which models a^{disp} as a function of two terms:

$$\frac{a^{disp}}{RT} = -2\pi\rho I_1(\eta,\bar{m})\overline{m^2\varepsilon\sigma^3} - \pi\rho\bar{m}C_1 I_2(\eta,\bar{m})\overline{m^2\varepsilon^2\sigma^3} \quad [55]$$

I_1 and I_2 are power series that represent simplified integrals of the radial distribution function of the hard-chain that depend only on the average number of segments and the number density.

$$I_1(\eta,\bar{m}) = \sum_{i=0}^{6} a_i(\bar{m})\eta^i \quad [56]$$

$$a_i(\bar{m}) = a_{0i} + \frac{\bar{m}-1}{\bar{m}}a_{1i} + \frac{\bar{m}-1}{\bar{m}}\frac{\bar{m}-2}{\bar{m}}a_{2i} \quad [57]$$

$$I_2(\eta,\bar{m}) = \sum_{i=0}^{6} b_i(\bar{m})\eta^i \quad [58]$$

$$b_i(\bar{m}) = b_{0i} + \frac{\bar{m}-1}{\bar{m}}b_{1i} + \frac{\bar{m}-1}{\bar{m}}\frac{\bar{m}-2}{\bar{m}}b_{2i} \quad [59]$$

The parameters, a_{0i} to a_{2i} and b_{0i} to b_{2i}, are constants presented in the original paper by Gross and Sadowski.[99] In Equation [55], C_1 represents an abbreviation of the following term:

$$C_1 = 1 + \bar{m}\frac{8\eta-2\eta^2}{(1-\eta)^4} + (1-\bar{m})\frac{20\eta-27\eta^2+12\eta^3-2\eta^4}{(2-3\eta+\eta^2)^2} \quad [60]$$

These equations are extended to mixtures using the van der Waal's mining rules shown previously in Section 3.2:

$$\overline{m^2\varepsilon\sigma^3} = \sum_i \sum_j x_i x_j m_i m_j \left(\frac{\varepsilon_{ij}}{kT}\right)\sigma_{ij}^3 \quad [61]$$

$$\overline{m^2\varepsilon^2\sigma^3} = \sum \sum x_i x_j m_i m_j \left(\frac{\varepsilon_{ij}}{kT}\right)^2 \sigma_{ij}^3 \quad [62]$$

The cross interaction parameters are defined by the Lorentz-Berthelot parameters in Equations [63] and [64]:

$$\sigma_{ij} = \frac{1}{2}\left(\sigma_i + \sigma_j\right) \quad [63]$$

$$\varepsilon_{ij} = \sqrt{\varepsilon_i \varepsilon_j}\left(1 - k_{ij}\right) \quad [64]$$

7.1.3 Association Interactions

The association contribution to Helmholtz free energy is defined as follows:

$$\frac{a^{assoc}}{RT} = \sum_i x_i \left[\sum_{A_i}\left(\ln X^{A_i} - \frac{X^{A_i}}{2}\right) + \frac{M_i}{2}\right] \quad [65]$$

where X is the fraction of associating sites in a fluid:

$$X^{A_i} = \left[1 + \sum_j \sum_{B_j} \rho_j X^{B_j} \Delta^{A_i B_j}\right]^{-1} \quad [66]$$

The strength of association between unlike sites, Δ^{AB}, is:

$$\Delta^{A_iB_j} = d_{ij}^3 g_{ij}\left(d_{ij}\right)^{seg} \kappa^{A_iB_j}\left[\exp\left(\frac{\varepsilon^{A_iB_j}}{kT}\right)-1\right] \quad [67]$$

where,

$$d_{ij} = \frac{1}{2}\left(d_i + d_j\right) \quad [68]$$

7.2 Appendix II: Supplementary Figures

7.2.1 Isobaric Heat Capacity of Pure Fluids

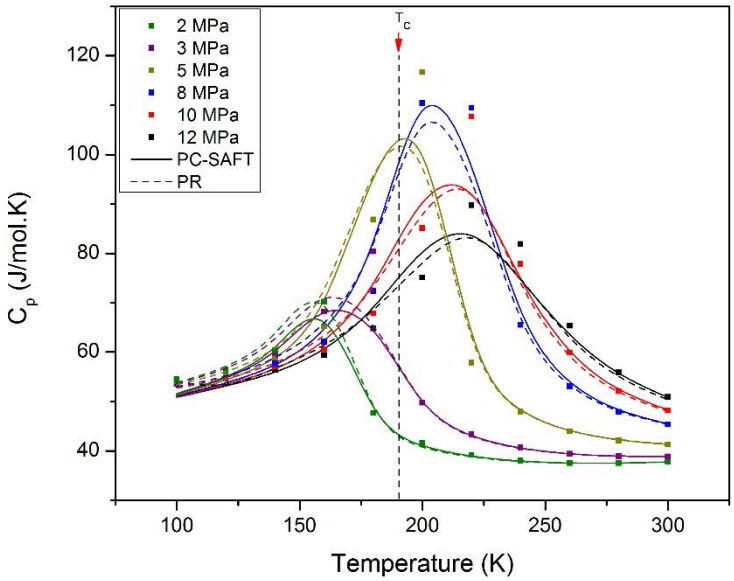

Figure 29. Isobaric heat capacity (C_p) of CH_4, experimental data (points) and model predictions lines)

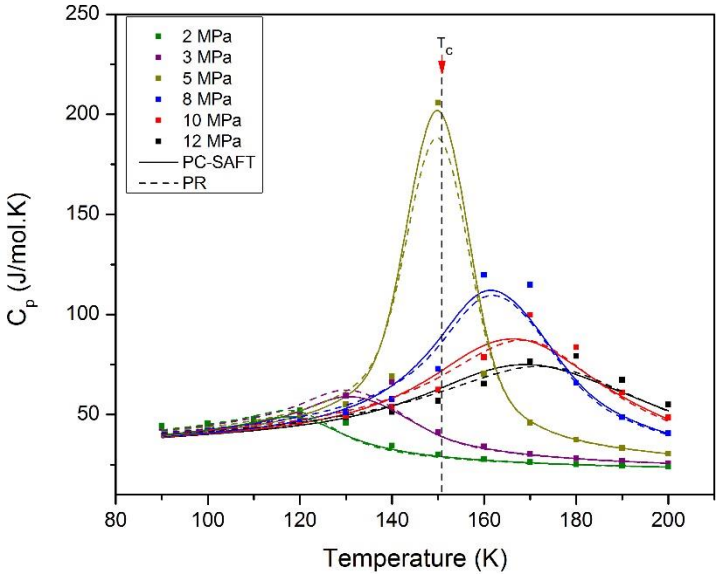

Figure 30. Isobaric heat capacity (C_p) of Ar, experimental data (points) and model predictions (lines)

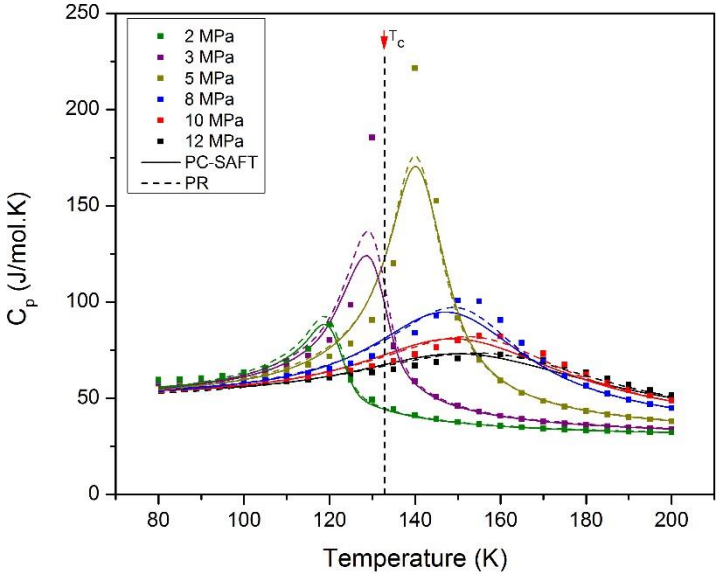

Figure 31. Isobaric heat capacity (C_p) of CO, experimental data (points) and model predictions (lines)

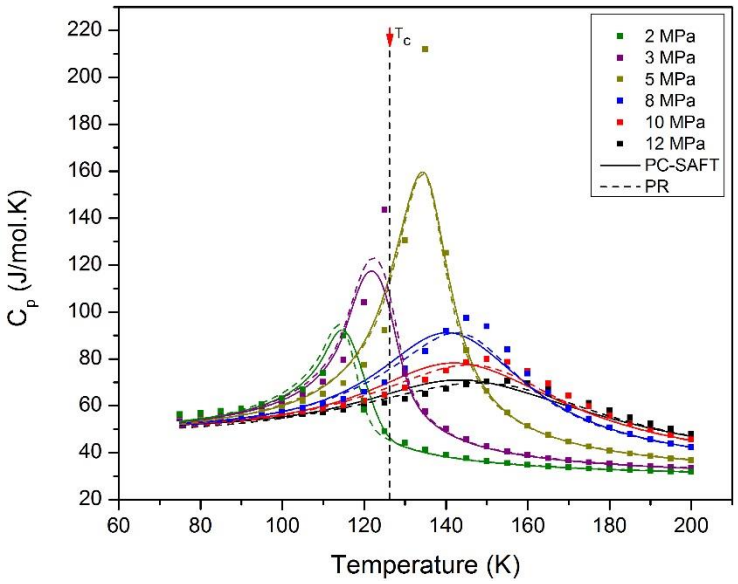

Figure 32. Isobaric heat capacity (C_p) of N_2, experimental data (points) and model predictions (lines)

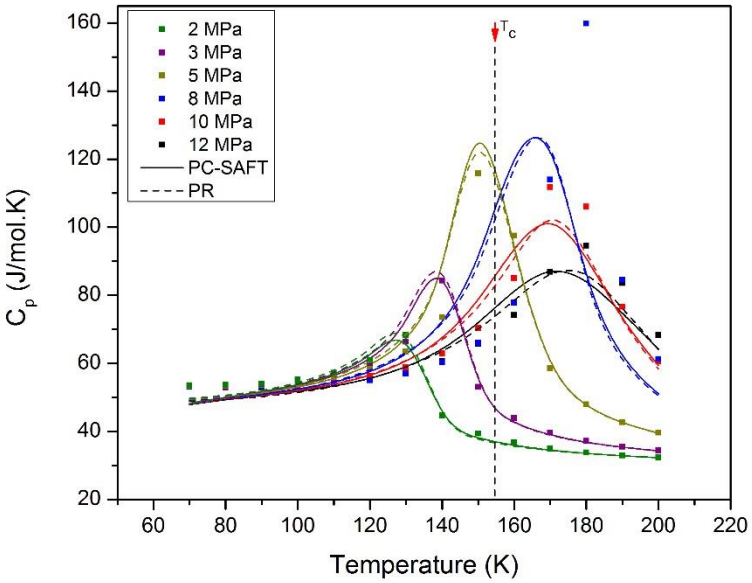

Figure 33. Isobaric heat capacity (C_p) of O_2, experimental data (points) and model predictions (lines)

7.2.2 Isochoric Heat Capacity of Pure Fluids

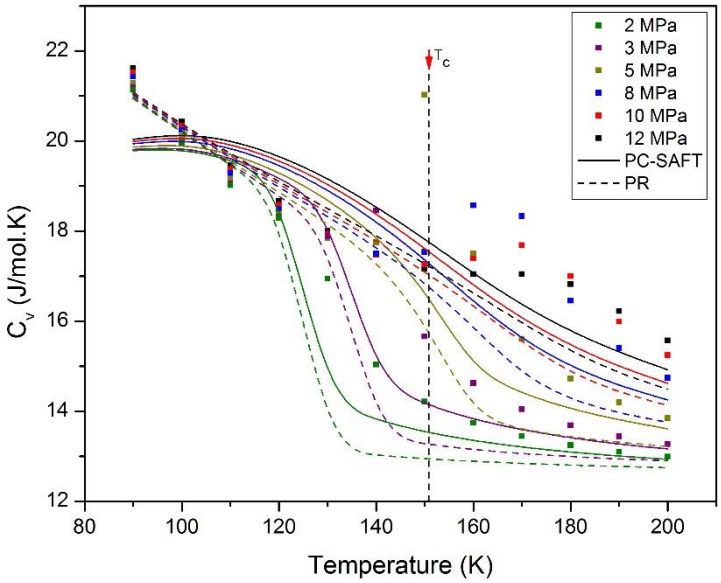

Figure 34. Isochoric heat capacity (C_v) of Ar, experimental data (points) and model predictions (lines)

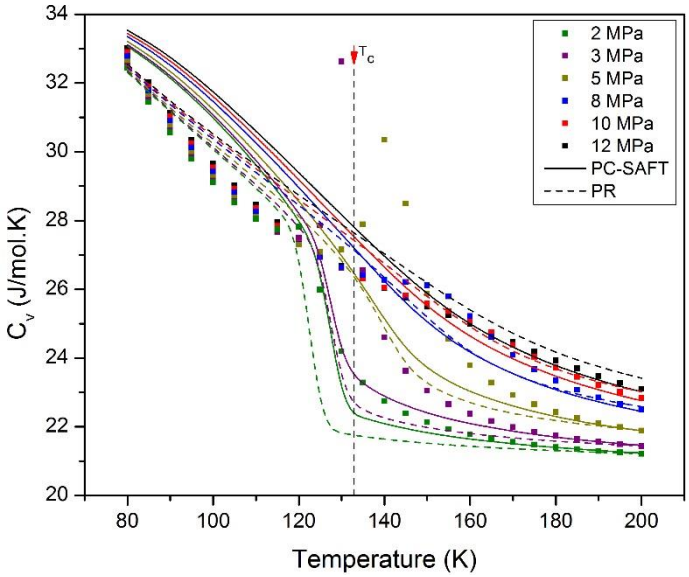

Figure 35. Isochoric heat capacity (C_v) of CO, experimental data (points) and model predictions (lines)

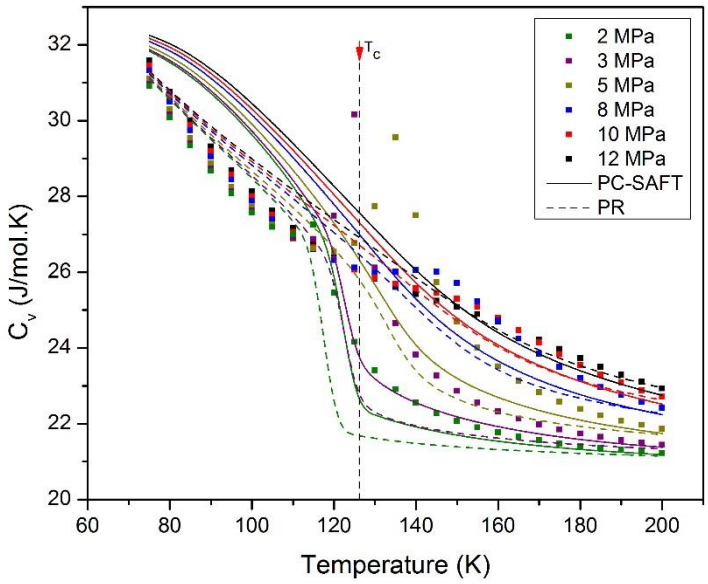

Figure 36. Isochoric heat capacity (C_v) of N_2, experimental data (points) and model predictions (lines)

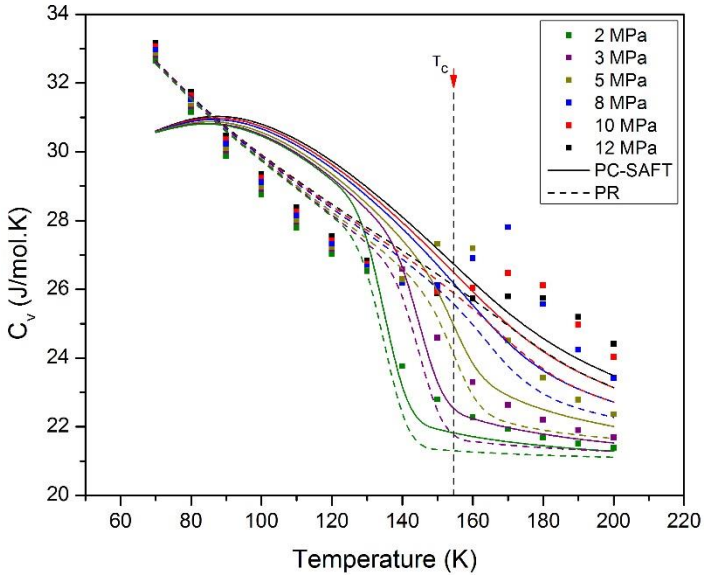

Figure 37. Isochoric heat capacity (C_v) of O_2, experimental data (points) and model predictions (lines)

7.2.3 Vapor-Liquid Equilibrium

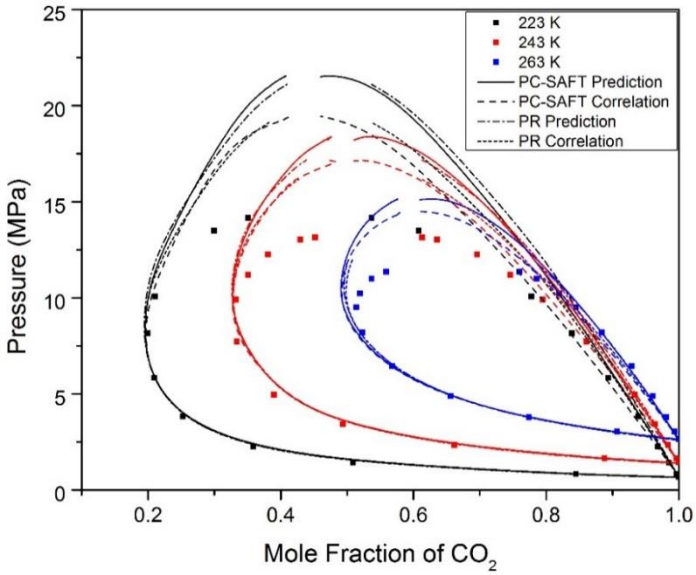

Figure 38. VLE for the binary mixture CO_2-CO, experimental data (points) and model predictions (lines)

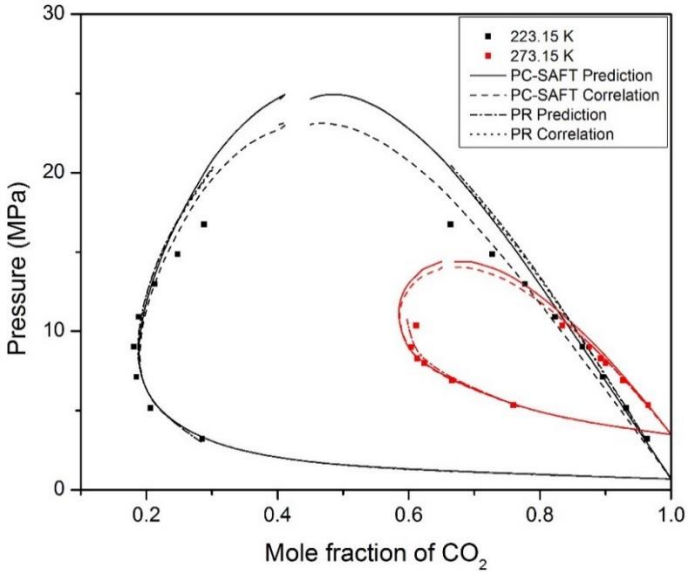

Figure 39. VLE for the binary mixture CO_2-N_2, experimental data (points) and model predictions (lines)

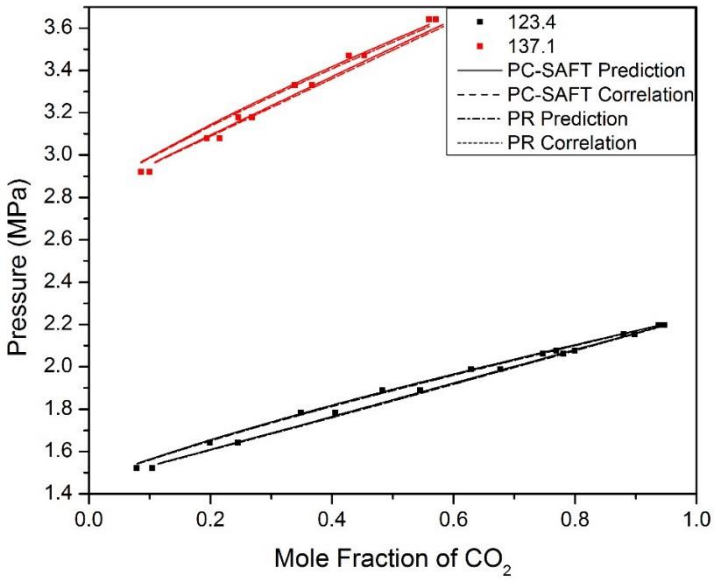

Figure 40. VLE for the binary mixture of CO-Ar, experimental data (points) and model predictions (lines)

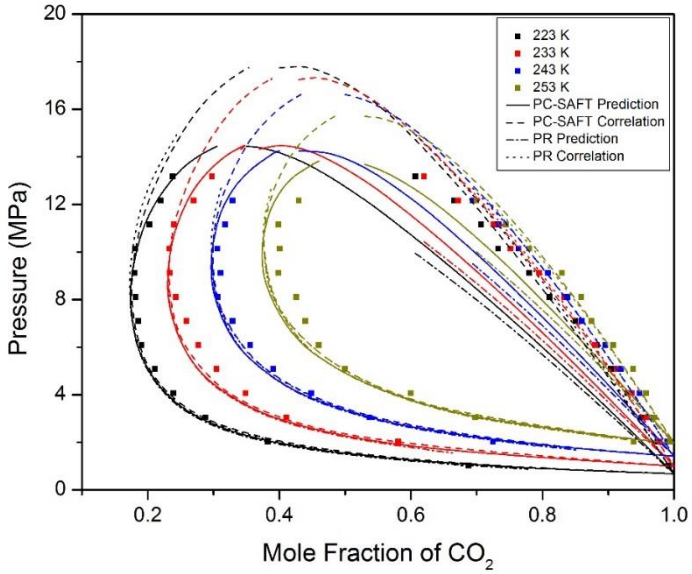

Figure 41. VLE for the binary mixture CO_2-O_2 mixture, experimental data (points) and model predictions (lines)

7.2.4 Speed of Sound of Pure Fluids

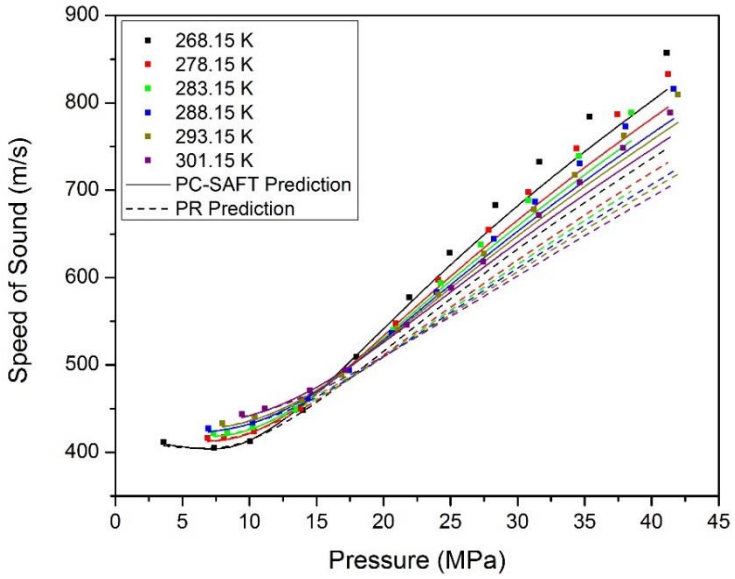

Figure 42. Speed of sound of CH_4, experimental data (points) and model predictions (lines)

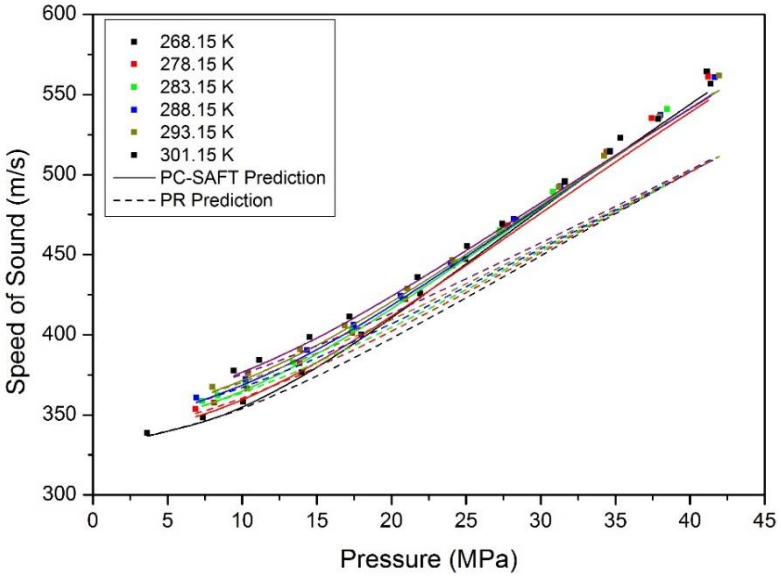

Figure 43. Speed of sound of CO, experimental data (points) and model predictions (lines)

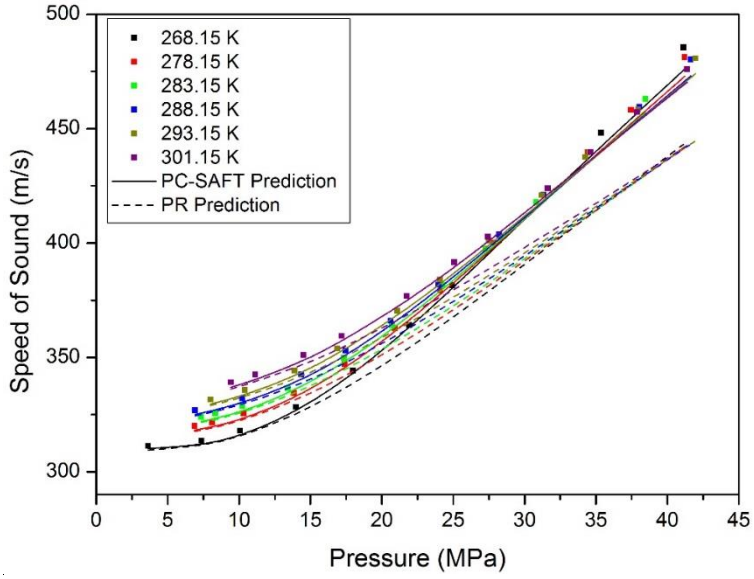

Figure 44. Speed of sound of O_2, experimental data (points) and model predictions (lines)

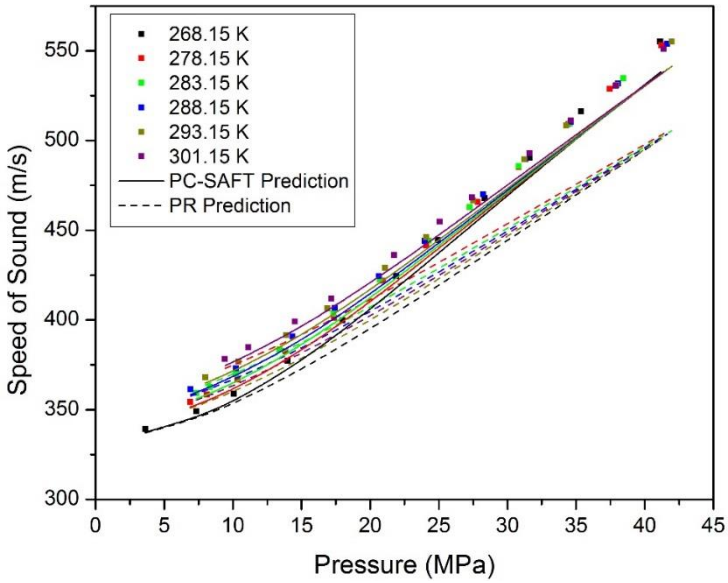

Figure 45. Speed of sound of N_2, experimental data (points) and model predictions (lines)

7.2.5 Speed of Sound of Mixtures

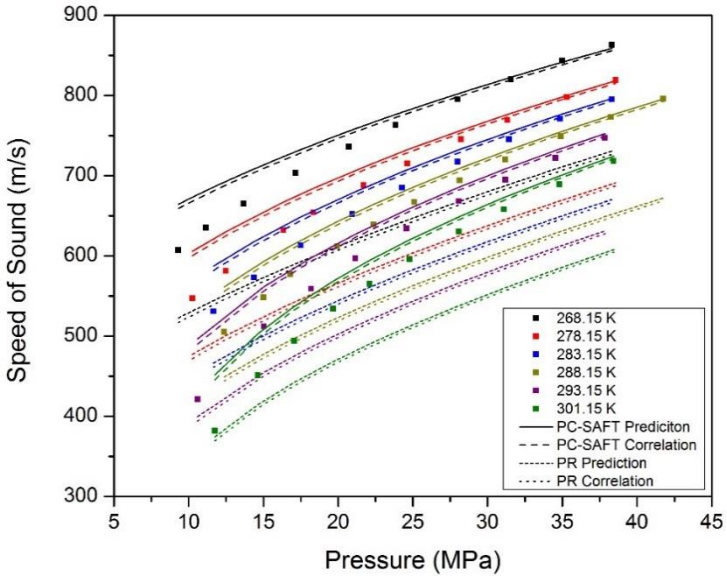

Figure 46. Speed of sound of CO_2-Ar, experimental data (points) and model predictions (lines)

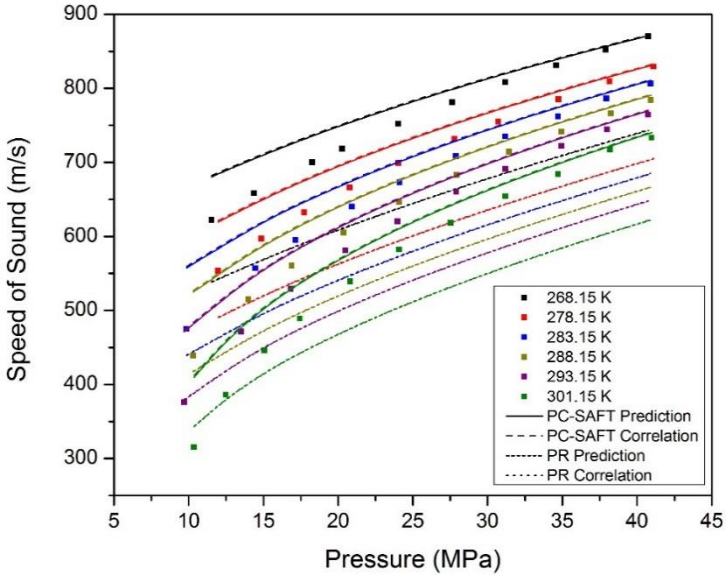

Figure 47. Speed of sound of CO_2-CO, experimental data (points) and model predictions (lines)

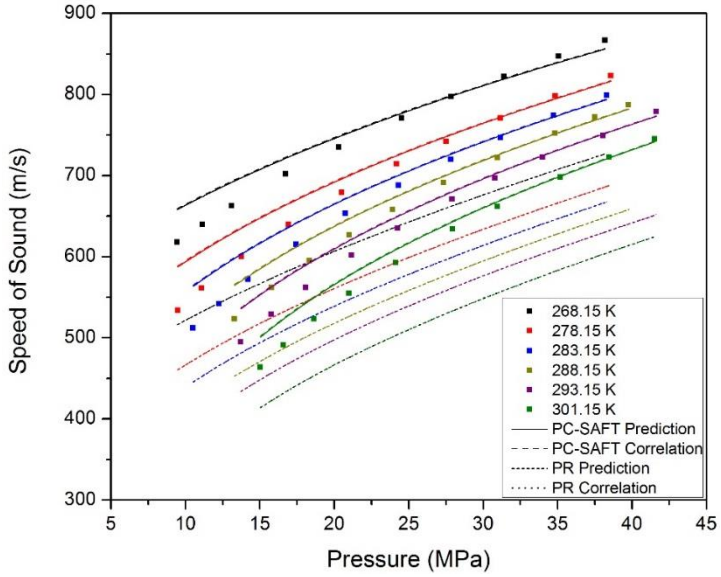

Figure 48. Speed of sound of CO_2-N_2, experimental data (points) and model predictions (lines)

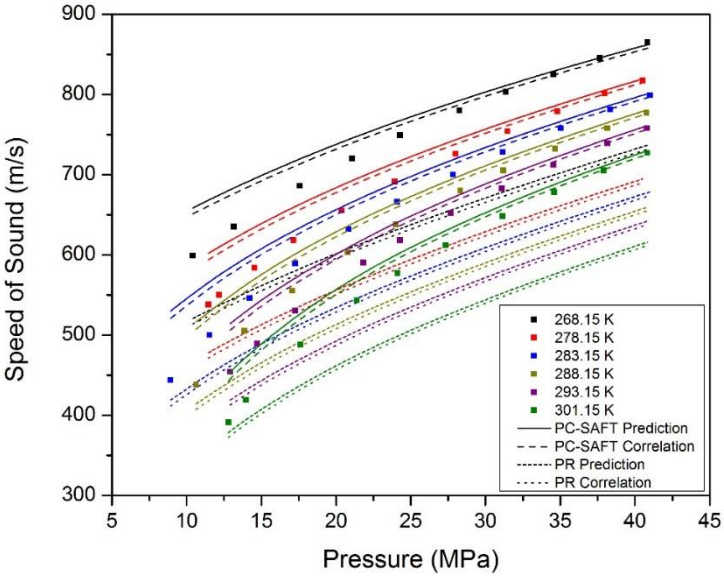

Figure 49. Speed of sound of the CO_2 –O_2 mixture, experimental data (points) and model predictions (lines)

7.2.6 Isothermal Compressibility of Mixtures

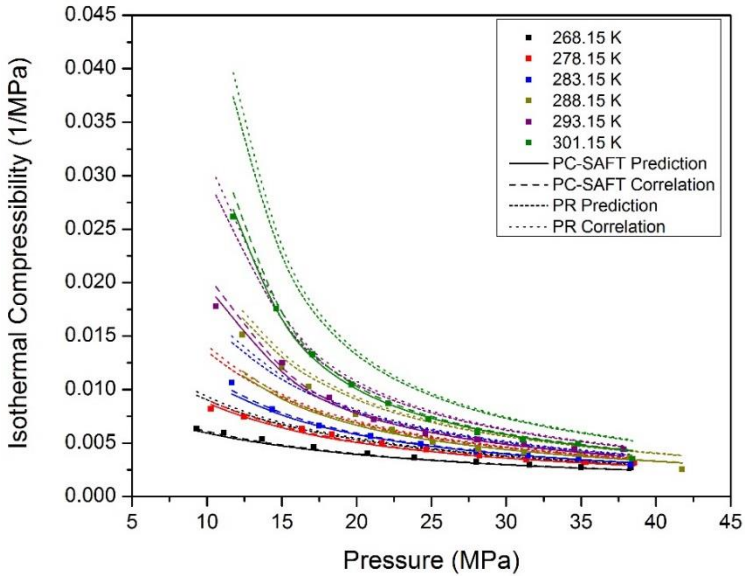

Figure 50. Isothermal compressibility of CO_2-Ar, experimental data (points) and model predictions (lines)

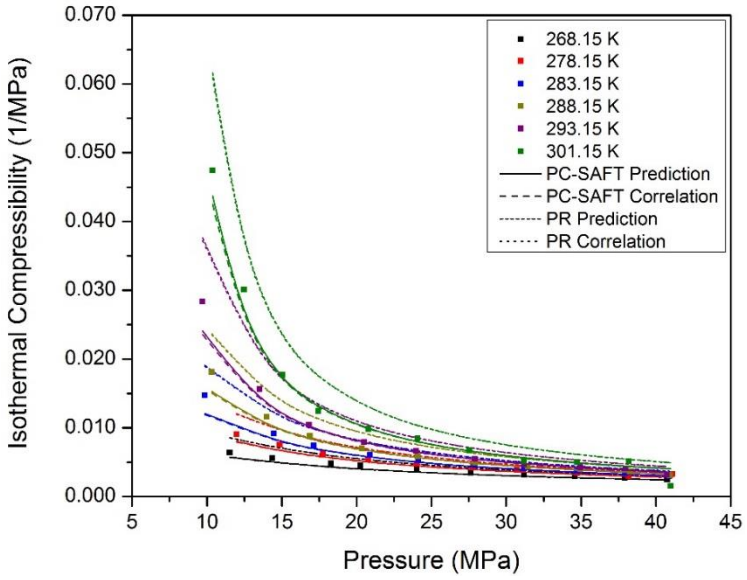

Figure 51. Isothermal compressibility of CO_2-CO, experimental data (points) and model predictions (lines)

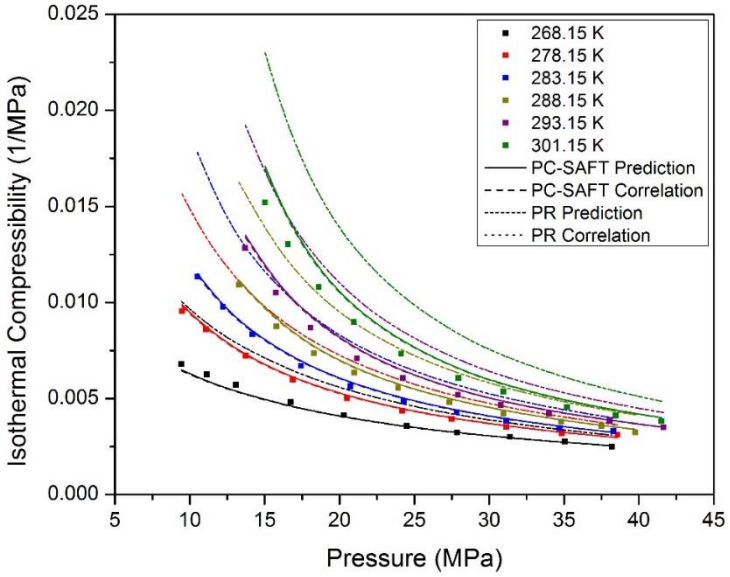

Figure 52. Isothermal compressibility of CO_2-N_2, experimental data (points) and model predictions (lines)

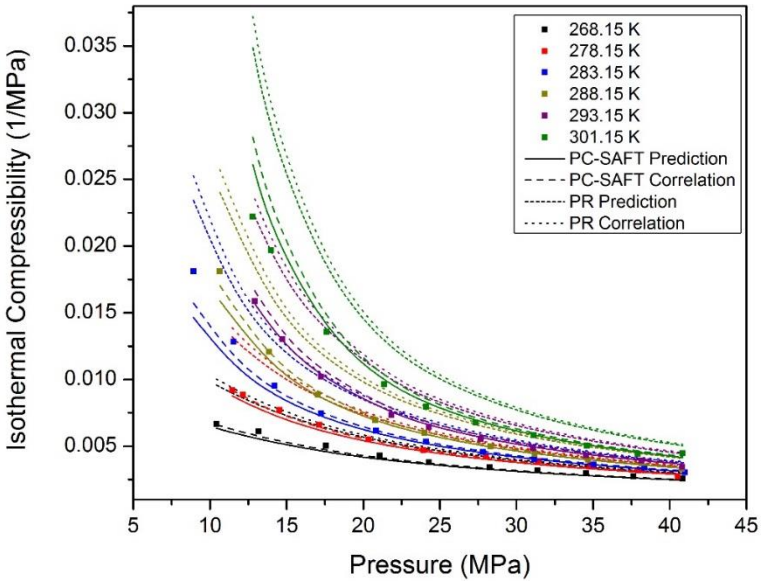

Figure 53. Isothermal compressibility of the CO_2 –O_2 mixture, experimental data (points) and model predictions (lines)

7.2.7 Liquid Water-Hydrate-Vapor Equilibrium

7.2.7.1 Pure Guest Hydrates

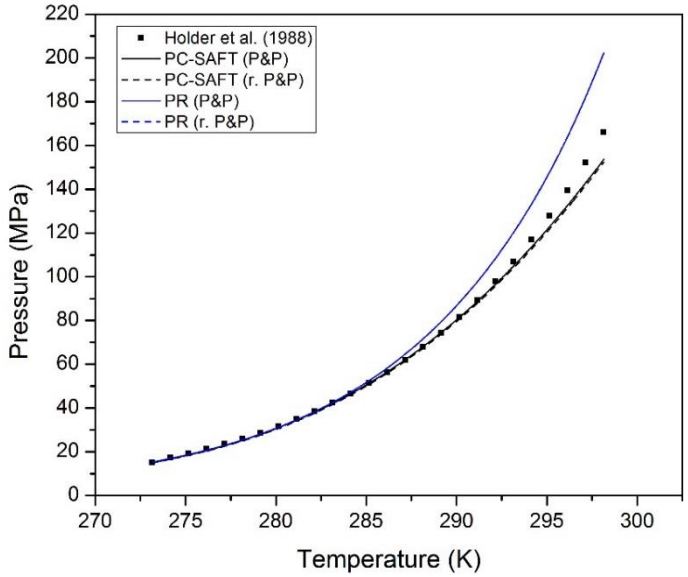

Figure 54. L_wHV phase equilibrium of N_2, experimental data (points) and model predictions (lines)

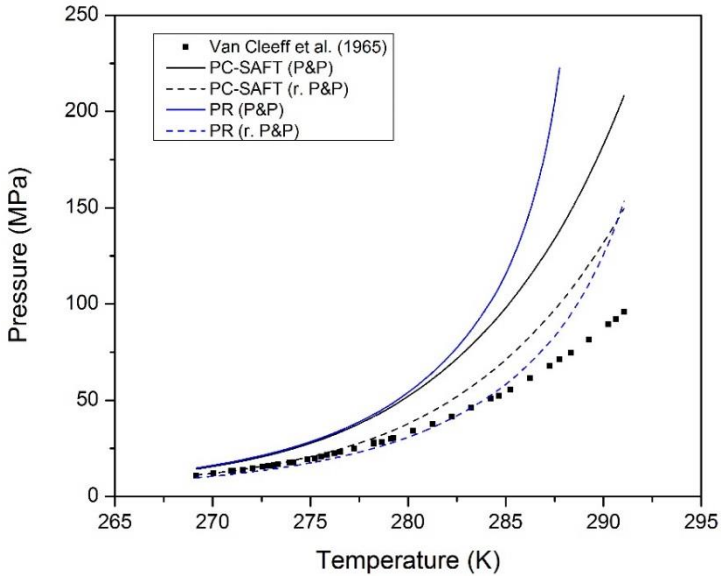

Figure 55. L_wHV phase equilibrium of O_2, experimental data (points) and model predictions (lines)

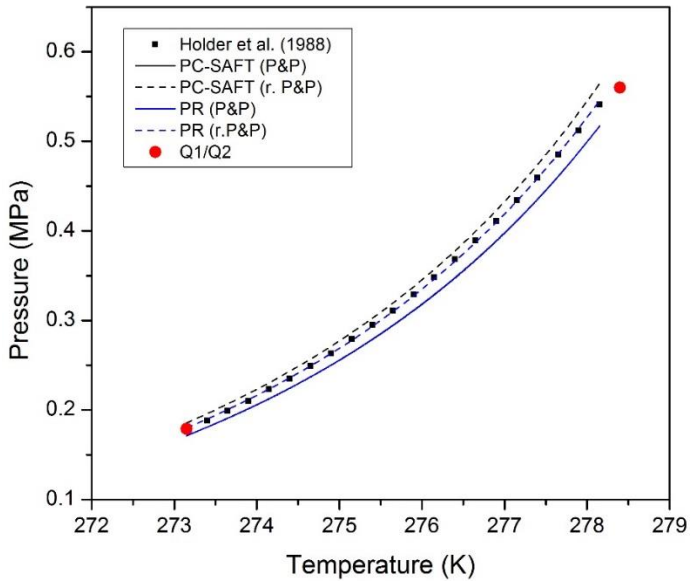

Figure 56. L_wHV phase equilibrium of C_3H_8, experimental data (points) and model predictions (lines)

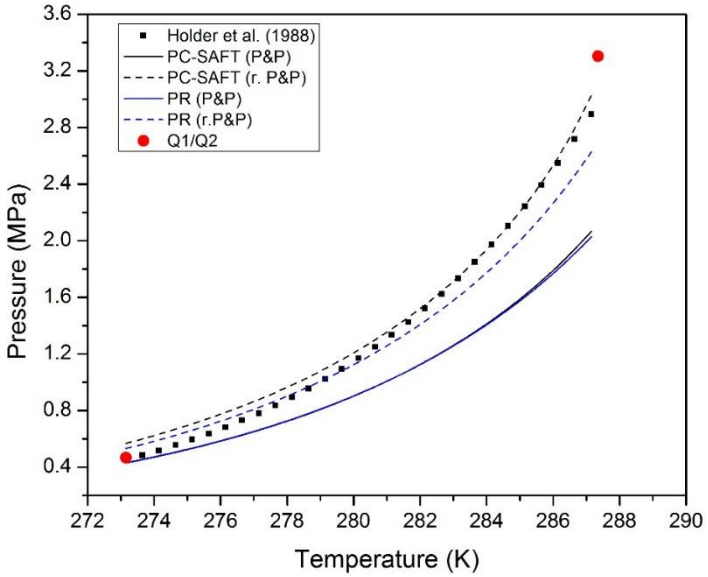

Figure 57. *L_wHV* phase equilibrium of C_2H_6, experimental data (points) and model predictions (lines)

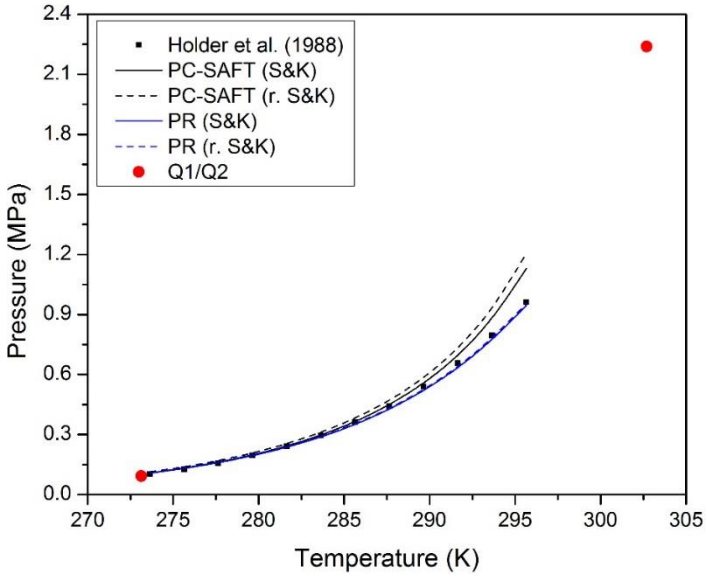

Figure 58. *L_wHV* phase equilibrium of H_2S, experimental data (points) and model predictions (lines)

7.2.7.2 Binary Mixtures of Hydrate Formers

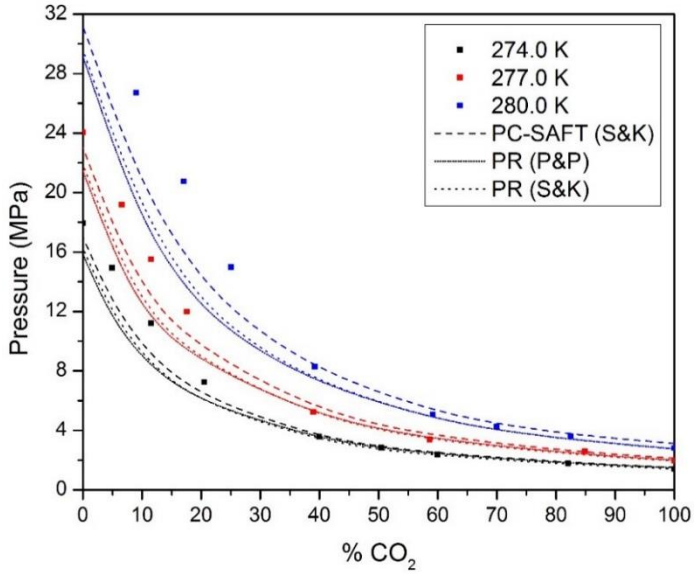

Figure 59. Prediction of *L_wHV* equilibrium for a binary mixture of CO_2-N_2 over a range of compositions, experimental data (points) and model predictions (lines)

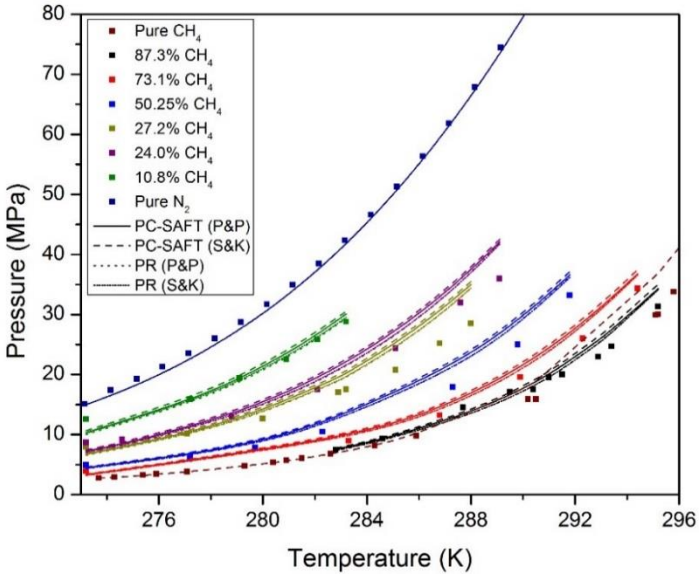

Figure 60. Prediction of L_wHV equilibrium for a binary mixture of CH_4-N_2 over a range of temperatures, experimental data (points) and model predictions (lines)

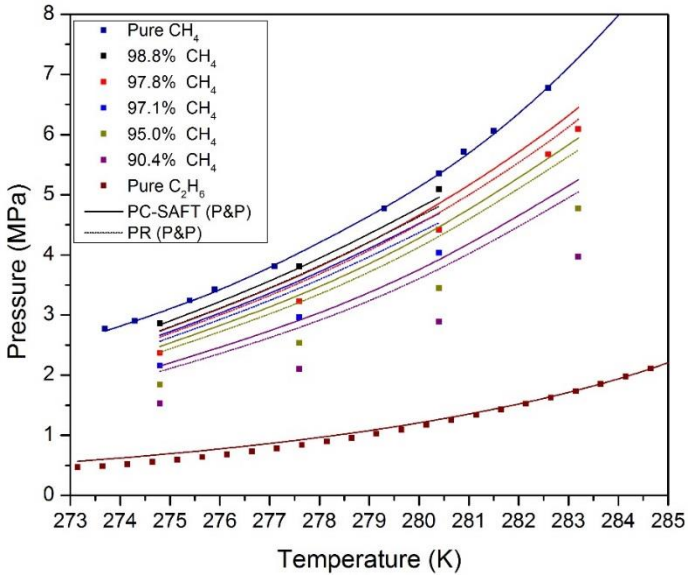

Figure 61. Prediction of L_wHV equilibrium for a binary mixture of CH_4-C_2H_6 over a range of temperatures, experimental data (points) and model predictions (lines)

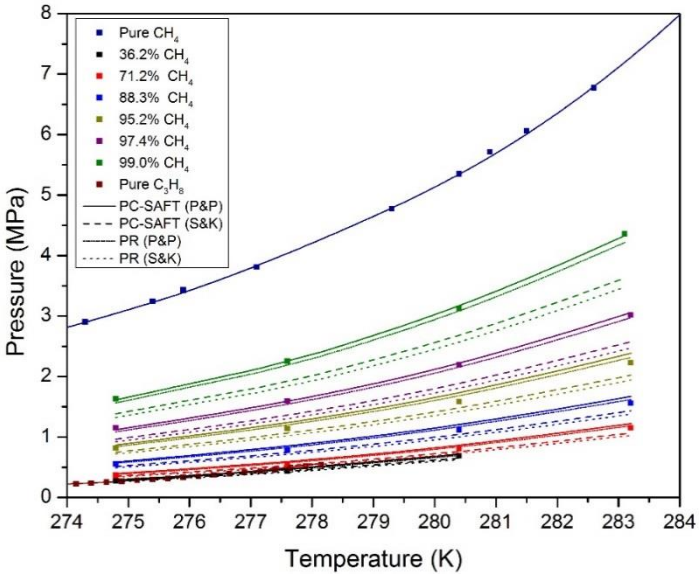

Figure 62. Prediction of L_wHV equilibrium for a binary mixture of CH_4-C_3H_8 over a range of temperatures, experimental data (points) and model predictions (lines)

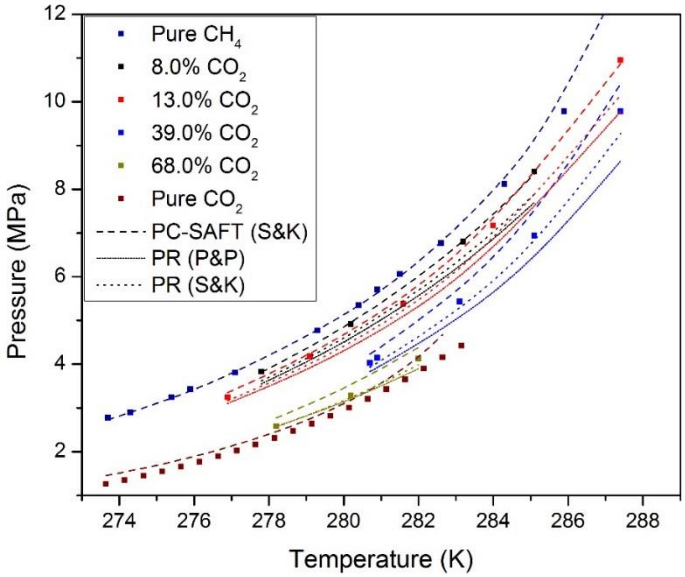

Figure 63. Prediction of L_wHV equilibrium for a binary mixture of CH_4-CO_2 over a range of temperatures, experimental data (points) and model predictions (lines)

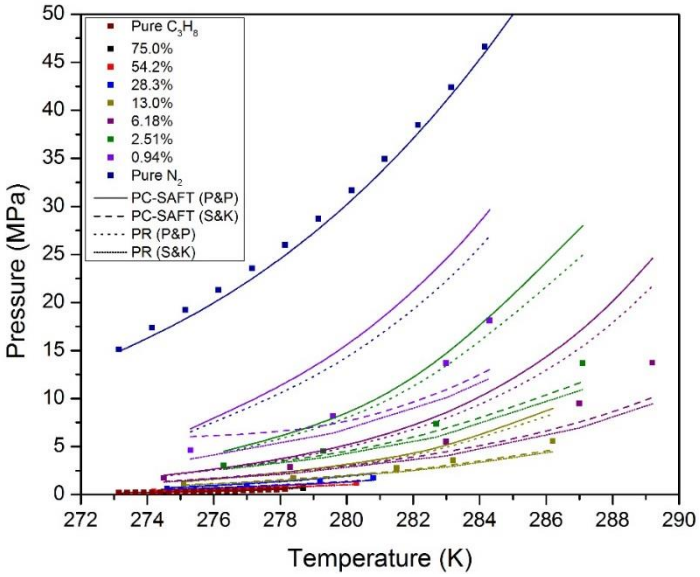

Figure 64. Prediction of L_wHV equilibrium for a binary mixture of C_3H_8-N_2 over a range of temperatures, experimental data (points) and model predictions (lines)

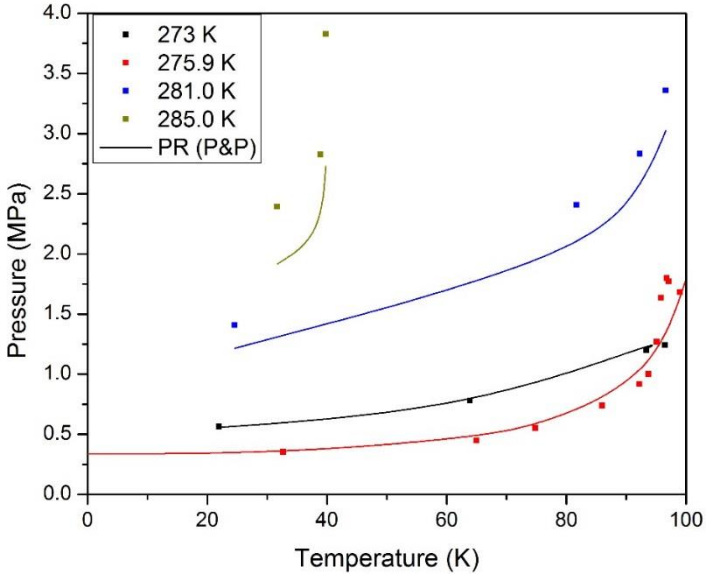

Figure 65. Prediction of L_wHV equilibrium for a binary mixture of CO_2-C_2H_6 over a range of compositions, experimental data (points) and model predictions (lines)

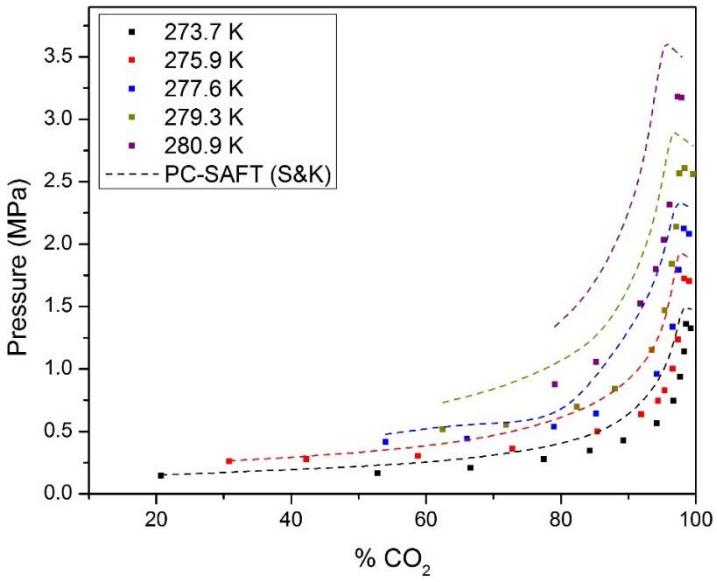

Figure 66. Prediction of *LwHV* equilibrium for a binary mixture of CO_2-*i*C_4H_{10} over a range of compositions, experimental data (points) and model predictions (lines)

7.2.7.3 Ternary Mixtures of Hydrate Formers

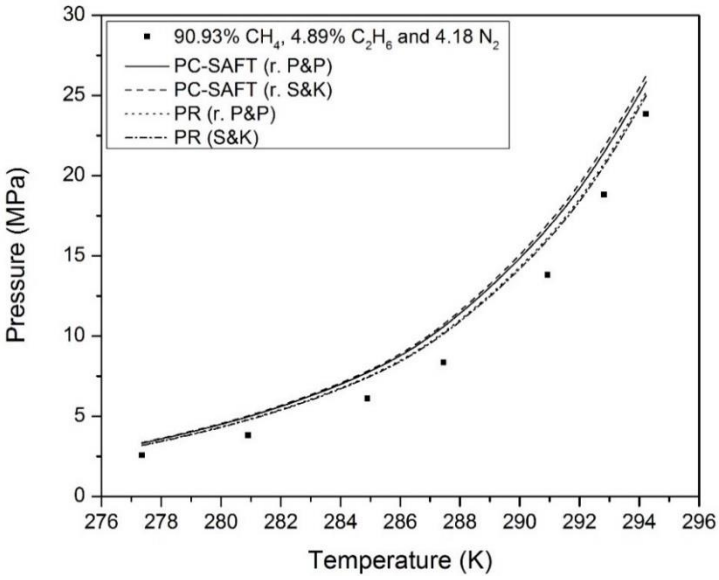

Figure 67. Prediction of *LwHV* equilibrium for the ternary mixture of CH_4-C_2H_6-N_2, experimental data (points) and model predictions (lines)

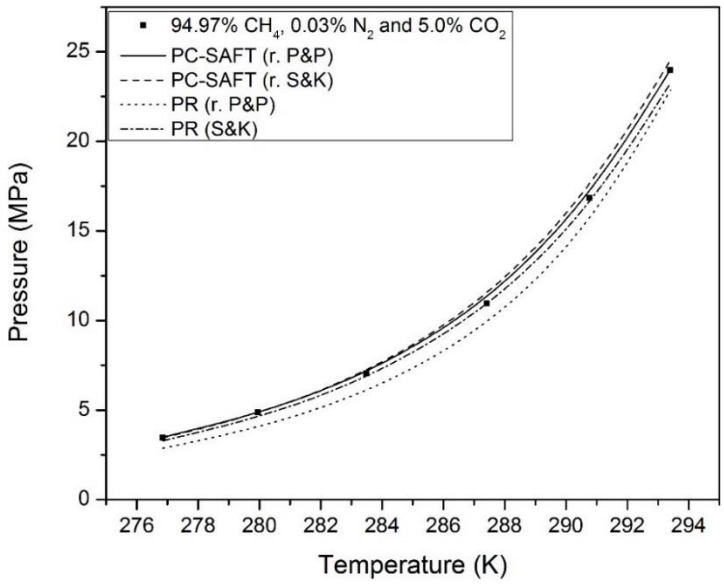

Figure 68. Prediction of L_wHV equilibrium for the ternary mixture of CH_4-CO_2-N_2, experimental data (points) and model predictions (lines)

7.2.7.4 Quaternary Mixtures of Hydrate Formers

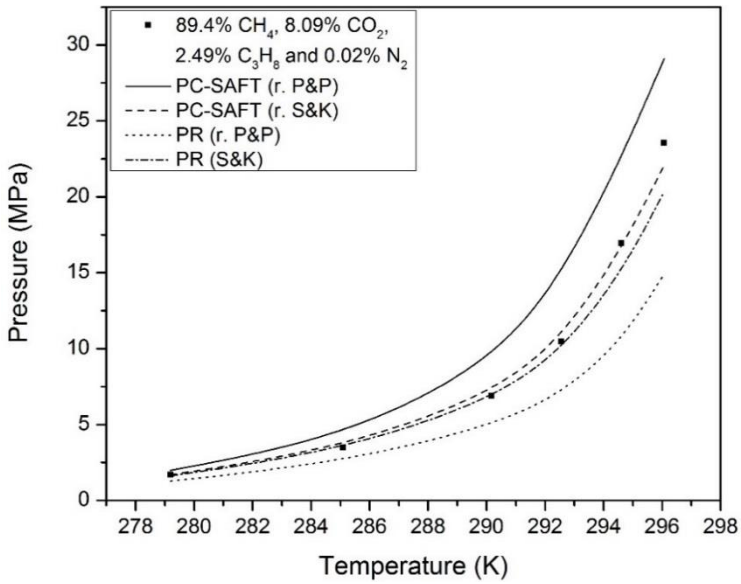

Figure 69. Prediction of L_wHV equilibrium for the quaternary mixture of CH_4-C_3H_8-CO_2-N_2, experimental data (points) and model predictions (lines)

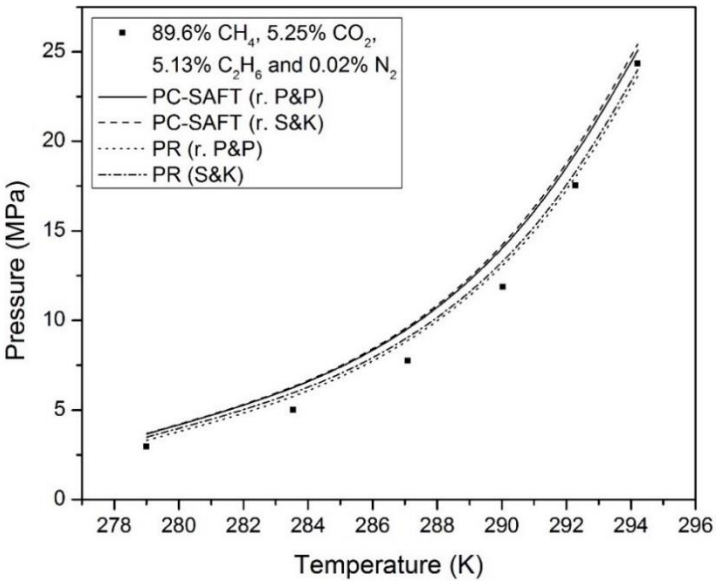

Figure 70. Prediction of L_wHV equilibrium for the quaternary mixture of CH_4-CO_2-C_2H_6-N_2, experimental data (points) and model predictions (lines)

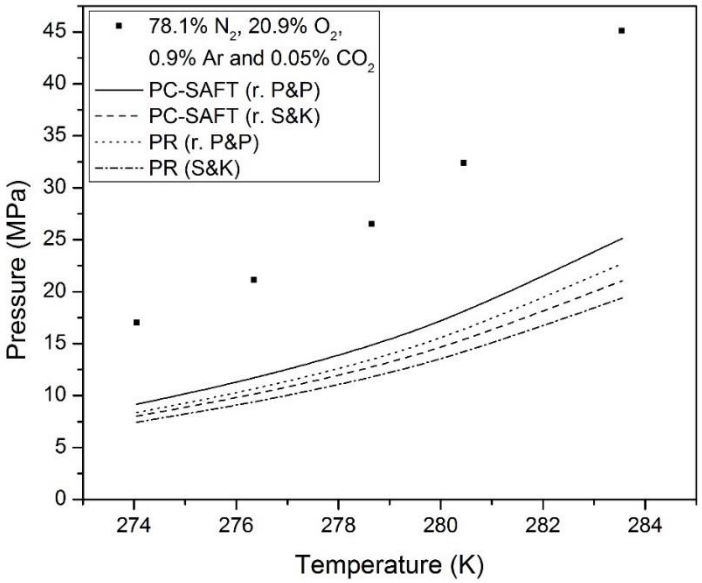

Figure 71. Prediction of L_wHV equilibrium for the quaternary mixture of CO_2-O_2-Ar-N_2, experimental data (points) and model predictions (lines)